Master thesis

Estimation of convection ahead of a solid/liquid interface during solidification of layered peritectic solidification morphologies

Author:

Tanja Pfeifer

Examiner:

Univ. -Prof. Dipl.-Phys. Dr.rer.nat. Andreas Ludwig

Leoben, Juni 18

Eidesstattliche Erklärung

Ich erkläre an Eides statt, dass ich diese Arbeit selbstständig verfasst, andere als die angegebenen Quellen und Hilfsmittel nicht benützt und mich auch sonst keiner unerlaubten Hilfsmittel bedient habe.

Leoben, 06.06.2018 _____

Tanja Pfeifer, B.Sc

Affidavit

I declare in lieu of oath, that I wrote this thesis and performed the associated research myself, using only literature cited in this volume.

Leoben, 06.06.2018

Tanja Pfeifer, B.Sc

Danksagung

An dieser Stelle möchte ich mich bei allen bedanken, die mich während der Anfertigung dieser Masterarbeit unterstützt und motiviert haben.

Mein besonderer Dank gebührt Herrn Prof. Andreas Ludwig, Leiter des Lehrstuhls für Modellierung und Simulation metallurgischer Prozesse an der Montanuniversität Leoben, für die Betreuung und Korrektur meiner Masterarbeit.

Des Weiteren möchte ich mich bei Herrn Dr. Johann Mogeritsch bedanken, der mir als Betreuer über die gesamte Dauer meiner Diplomarbeit immer mit konstruktiver Kritik sowie vor allem viel Geduld zur Seite stand.

Ich möchte auch bei meinen Arbeitskollegen für die gute und freundschaftliche Zusammenarbeit in den letzten Jahren danken.

Mein Dank gilt auch der FFG für die Finanzierung der Diplomarbeit.

Abstract

The present study will emphasize on the investigations of the effect of convection on the formation of peritectic layered structures near the constitutional undercooling by using the binary organic peritectic model system TRIS–NPG. Under conditions where both phases solidify in a planar manner it is possible that for peritectic concentrations the metastable phase nucleates before the initial phase reaches steady state. This enables a competitive growth between the primary and the peritectic phase which leads to peritectic layered structures. Investigation on metal alloys exhibited various layered microstructures in form of bands, island bands, and peritectic coupled growth similar to eutectic structures.

Since such structures are highly influenced by convection in-situ investigations were done to make visible the flow pattern and to observe the corresponding dynamic of the solid/liquid interface. The experimental procedure was carried out by directional solidification in a Bridgman-furnace and the material was enriched with tracers to visualize the convection.

The investigations on the organic model system TRIS–NPG indicated different forms of flow pattern. The fact that the particles show that convection influence the formation of layered structures was a major finding in this project. Another important observation was the influence of liquid channels and micro-plumes within the mushy zone on the evolution of bands in lateral direction.

Kurzfassung

In der vorliegenden Arbeit wird der Einfluss der Konvektion auf die Bildung peritektischer Schichtstrukturen in der Nähe der konstitutionellen Unterkühlung mittels des binären organischen peritektischen Modellsystems TRIS-NPG untersucht. Unter Bedingungen, bei denen beide Phasen planar erstarren, ist es möglich, dass für peritektische Konzentrationen die metastabile Phase nukleiert, bevor die primäre Phase den stationären Zustand erreicht. Dies ermöglicht ein kompetitives Wachstum zwischen der primären und der peritektischen Phase, welche zu peritektischen geschichteten Strukturen führt. Untersuchungen an Metalllegierungen zeigten verschiedene geschichtete peritektische Mikrostrukturen in Form von Bändern, Inselbändern und peritektisch gekoppeltem Wachstum, ähnlich wie bei eutektischen Strukturen.

Da solche Strukturen stark durch Konvektion beeinflusst werden, wurden in-situ Untersuchungen durchgeführt, um das Strömungsmuster sichtbar zu machen und die entsprechende Dynamik der fest/flüssig-Grenzfläche zu beobachten. Die experimentelle Durchführung erfolgte durch gerichtete Erstarrung in einem Bridgman-Ofen und das Material wurde mit Tracern angereichert um die Konvektion sichtbar zu machen.

Die Untersuchungen am organischen Modelsystem TRIS - NPG zeigten unterschiedliche Strömungsmuster. Dabei wurde nicht nur der Einfluss der Konvektion vor der Erstarrungsfront erkannt, sondern auch der Einfluss von flüssigen Kanälen in der breiigen Zone auf die Bildung von Bandstrukturen.

Contents

1. Introduction

The study of microstructures has become an indispensable field of research in materials science. The microstructure determines the material behavior, its mechanical and physical properties and thus enables a better knowledge for the entire material process chain. After years of intensive research on the growth laws under a wide range of terms, attention is being paid now to convection within the melt.

Since convection ahead of the solid/liquid (s/l) interface during solidification cannot be studied on polished metal samples, it must be observed in "real time". Therefore, the following two methods are widely used: In-situ observation of metals/alloys (i) by X-ray method [1, 2] and (ii) by optical investigation with transparent organic model systems. Such methods require substances which have a high temperature plastic phase or rather a non-faceted (nf) phase, called plastic crystals. The plastic crystals solidify in a metal-like planar, cellular or dendritic manner. So, they show the same solidification morphologies, lattice structures and some other similar properties as metals. These facts make the use of these materials quite attractive for the study of solidification [3-6]. Near or below the limit of constitutional undercooling of both solid phases, isothermal peritectic coupled growth (PCG), cellular peritectic coupled growth, discrete bands, island bands, and oscillatory tree-like structures were found [7-16].

The understanding of such solidification morphologies in peritectic systems is still not completed. X-Ray investigations of directionally solidified peritectic alloys such as Zn-Ag [18], Sn-Cd, [11, 16, 19, 20], Ni-Al, [21] and Nd-Fe-B, [22] have revealed numerous complex microstructures. Studies on the microstructure of the binary organic peritectic system "TRIS" (TRIS(hydroxyl-methyl)amino-methane and "NPG" (Neopentylglycol) have been carried out at the Montanuniversität (MUL). Here, focus was laid especially on layered microstructures [17]. It is now assumed that the evolving structures interact with the liquid flow (thermo-solutal convection) in front of the s/l interface.

The present work deals with in-situ observation of the transparent organic peritectic system TRIS-NPG via directional solidification within a Bridgman furnace. Here, focus was laid on thermo-solutal convection in front of the s/l interface of peritectic layered structures. The flow is visualized adding tracers into the material and the observed dynamics of the interface during the formation of layered structures were studied.

2. State of the Art

In the following chapter, theoretical basics of solidification will be presented as far as necessary for the understanding of this work. Solidification of pure metals or alloys provides the starting point for the formation of the inner material structure which determines the mechanical and physical properties. Therefore, it is of great interest, to understand the development of the microstructure.

For this purpose, the peritectic system and the morphology of the solidification interface is first described. Here, the microstructure formation above and below the critical velocity is discussed. Such organic model systems are quite attractive to study the evolution of the microstructure by using the Bridgman method. They offer the advantage to be transparent and solidify like metals at a temperature range where a simple transmission microscope can be used. After this, details of the binary peritectic model system TRIS–NPG are given. Finally, theoretical models and publications relating to convection during solidification are presented.

2.1 Peritectic Systems

The concept of solidification describes the change from liquid to solid. In this study, special attention is paid to layered structures, which occur in a peritectic systems, like in Fig. 1.
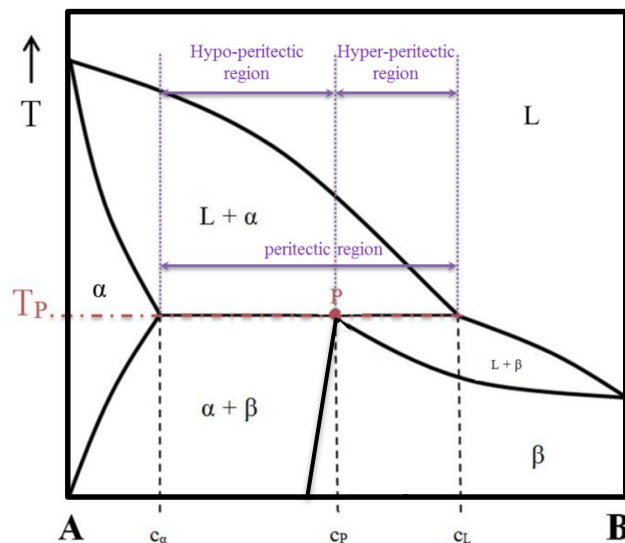

Fig. 1: Peritectic system. Point P marks the point of peritectic reaction. The red dotted line indicates the peritectic Temperature T_P.

The peritectic reaction is characterized that the initial primary phase [α] and a liquid phase [L] form a second solid (peritectic) phase [β] at the peritectic temperature (T_P) according to:

$$L + \alpha \rightarrow \beta \qquad (1)$$

Therefore, an alloy with a peritectic concentration c_P (Point P, Fig. 1) first crystallizes below the liquidus line. The fluid and α-phase will convert completely into the β-phase at the peritectic temperature, T_P [6].

The region $c_\alpha \leq c_0 \leq c_P$ is called the hypo-peritectic region. An alloy, which has a concentration c_0 within the hypo-peritectic region starts to solidify with the primary [α] phase and transforms partly to the peritectic [β] phase when passing T_p. Whereas, for concentrations $c_p < c_0 < c_l$, the α-phase transforms completely into the peritectic β-phase, which is the hyper-peritectic region.

It is important to note, that the liquid/solid transition L→β is much faster than the solid/solid transformation from α→β. This is because the diffusion in liquid is much faster than the diffusion in solid. As a consequence, peritectic reactions are mostly far away from a thermodynamic equilibrium [23].

2.2 Morphology of the Solidification Front

The form of solidification microstructure is governed mainly by the cooling condition and the alloy composition. For pure elements and under directional solidification conditions, the solidification front is planar, but for alloys there are essentially two basic growth morphologies, dendritic/cellular and eutectic. Peritectic alloys grow in a dendritic manner, whereby, under special conditions it is possible that they solidify like eutectics, which is part of this thesis, called peritectic layered structures. The morphology becomes unstable if perturbations are amplified during the solidification. For alloys, the solute components will pile-up ahead of the interface due to the different solubility of the elements [24].

The segregation behavior of an element is characterized by the distribution coefficient k:

$$k = \frac{c_s}{c_l} \qquad (2)$$

It describes the ratio of the solidus concentration c_s of the element in the alloy and to the corresponding liquidus level c_l at a temperature T, see Fig. 2.
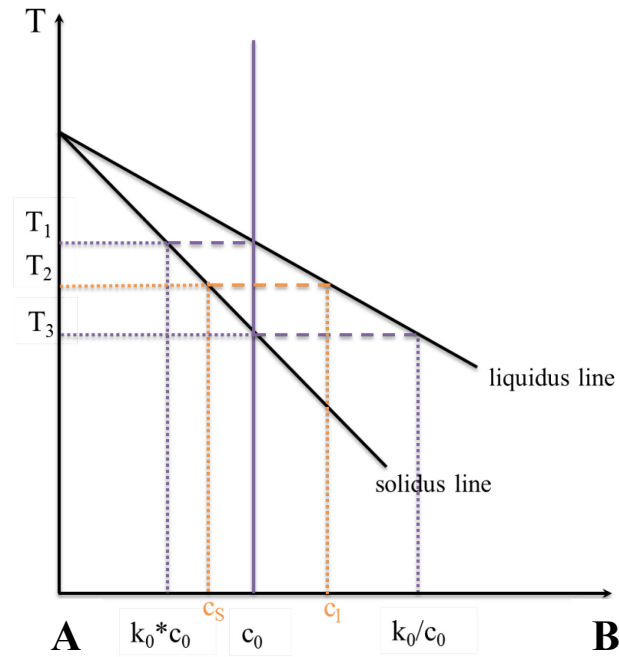
Fig. 2: Connection between phase diagram and distribution coefficient.

Within the solid phase the less soluble component is collected in front of the interface and diffuses back into the melt. This leads to a pile-up of the less soluble components within the liquid and to an increase in the concentration of the rejected components in front of the solidification front in form of a boundary layer, see Fig. 3.
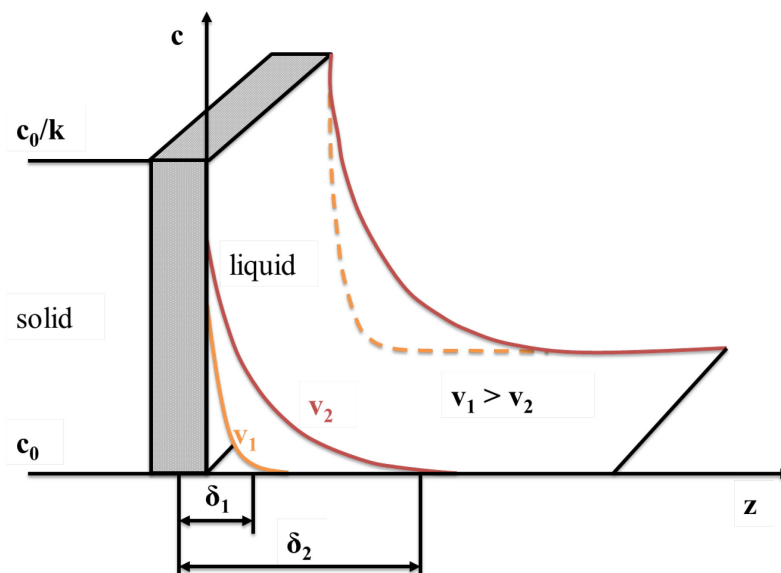

Fig. 3: Sketch of two different boundary layers δ_1 and δ_2 for a planar interface. The layer thickness increases with decreasing growth velocity v [24].

At the solidification front the concentration increases up to c_0/k and the concentration within the melt decreases to c_0 as:

$$c_l = \Delta c_0 \cdot e^{\left(-\frac{v}{D_L}\right) z} \tag{3}$$

Where, v is the solidification rate and D_L is the diffusion coefficient and z the growth direction of the interface.

The boundary layer thickness δ is defined as:

$$\delta = \frac{2 \cdot D_L}{v} \tag{4}$$

and depends on (i) the diffusion coefficient D_L in the liquid and (ii) the solidification velocity v. The development of the pile-up requires a certain distance of solidification until the s/l interface can grow under steady-state condition, called initial transient-state. In case of cellular or dendritic growth, where $v > v_{\alpha,\beta}$, steady-state is reached faster than in case of a planar solidification front [24].

Fig. 4 shows the morphological instability of an alloy in detail. In the liquid a temperature gradient G_T, imposed by the heat flux, exists ahead of the s/l interface. The corresponding liquidus and solidus temperatures, T_L and T_S, are given by the individual phase diagram. Due to the formation of the boundary layer the concentration changes from c_0 to c_0/k and the liquidus temperature decreases. Hence, in front of the solidification interface, the actual temperature might fall locally below the liquidus temperature.

The concentration impoundment (c_l–c_0) ahead of the solidification front reduces the liquidus temperature T_l. The constructed concentration profile leads to the gradient of the liquidus temperature. If the profile of the temperature T_q in front of the interface (temperature gradient in the melt) is now lower than the equilibrium temperature T_l, the melt is constitutional undercooled (shown as shaded area within Fig. 4), which leads to the instability of the phase boundary [25]. This zone is defined as the volume element of the melt in which the melt is in a metastable state. Small perturbations of the s/l interface increase and lead to cellular and dendritic growth.
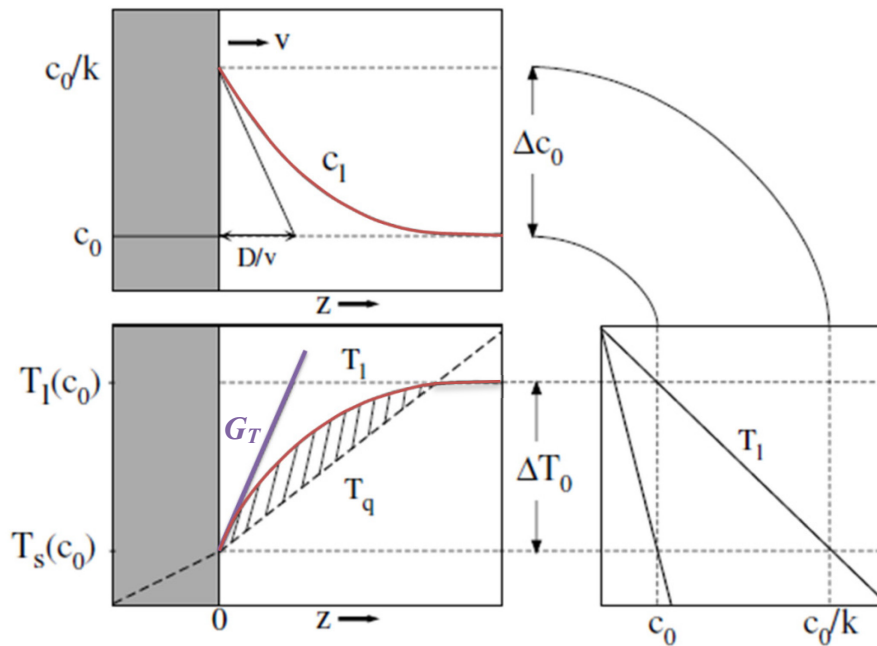
Fig. 4: Concept of constitutional undercooling. The zone of constitutional undercooling is marked as shaded area, it occurs if $T_1 > T_q$ [24].

The "Tiller criterion" represents the boundary condition for the appearance of this constitutional undercooling [26]. The limit of constitutional undercooling is given by the following equation:

$$v = \frac{G_T \cdot D_L}{\Delta T_0} \tag{5}$$

Where, v is the velocity, G_T is the temperature gradient and ΔT_0 is the temperature difference between solidus and liquidus line.

For $v > v_c$ constitutional undercooling ahead of the s/l interface exist and the planar solidification front will become unstable. So the initial planar s/l interface breaks and cells or dendrites will start to grow.

At the limit of constitutional undercooling or rather $v \leq v_c$ a stable planar front grows at the corresponding solidus temperature T_S [24]. For controlled directional solidification like it is used in the Bridgeman method the temperature gradient G_T is determined by the furnace.

Therefore, the occurring solidification morphology can be controlled only by adjusting the pulling velocity v_{Pull}, which is connected to the growth rate.

A peculiarity of the peritectic system is that the values for each phase, ΔT_α and ΔT_β, can be largely different, see Fig. 5. Hence, for a certain solidification velocity v it is possible that one phase grows above the critical velocity whereas the other is below the limit ($v_c^\alpha < v < v_c^\beta$ for $\Delta T_\alpha > \Delta T_\beta$) [17]. It is possible that the α-phase grows above the limit of constitutional undercooling whereas the β-phase grows planar (if $\Delta T_\alpha > \Delta T_\beta$). The interface becomes planar for both phases as soon as the solidification velocity is below the critical velocities ($v < v_c^\alpha$ and v_c^β).
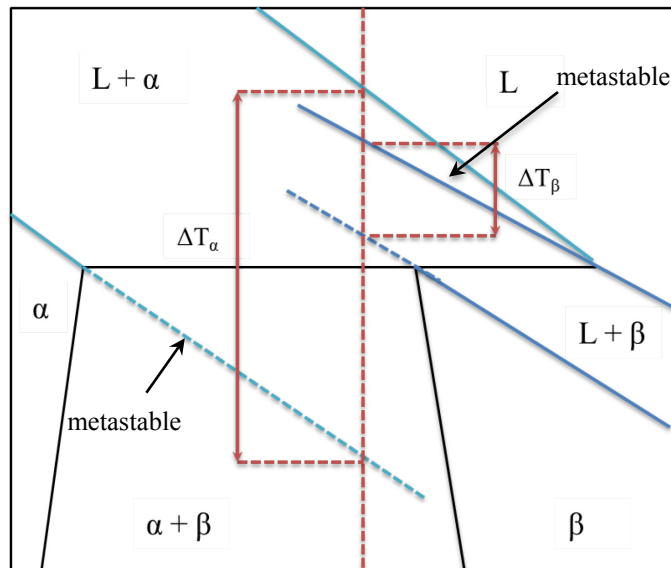
Fig. 5:   Temperature difference between liquidus and solidus line of the primary α-phase and the β-phase for a concentration c_0.

Cellular and dendritic growth

Cellular and dendritic morphologies occur above the critical velocity of constitutional undercooling. The planar interface becomes unstable and transforms into cells or dendrites to reduce the zone of constitutional undercooling. Whereby, cells and dendrites are growing undercooled with regard to the liquidus temperature T_L.
Cellular growth occurs for conditions between planar and dendritic solidification. They exist at low solidification velocities near the limit of constitutional undercooling and also for higher velocities close to the absolute limit of stability [27].

The total undercooling for a cellular interface is approximately equal to G_T/v and the growth temperature can thus be written as [28]:

$$T_c = T_{liq}(c_0) - \frac{G_T \cdot D_L}{v} \tag{6}$$

where, $T_{liq}(c_0)$ is the liquidus temperature of the growing phase at composition c_0.

Close to the limit of constitutional undercooling, the composition fluctuations ahead of the cellular interface can be neglected since they are small compared to the solute pile-up. The composition field ahead of the cellular solid/liquid interface can then be calculated according to:

$$c(z) = c_0 + \frac{G_T \cdot D_L}{m \cdot v} \cdot e^{\left(-\frac{V \cdot z}{D}\right)} \tag{7}$$

where, m is the liquidus slope of the growing phase [24].

Planar interface and layered structures

For $v \leq v_c$ a planar solidification front is expected. Trivedi published a theoretical model to explain the planar growth under the assumption of (i) a planar interface for both phases and (ii) the absence of convection in the liquid.

It predicts cyclic nucleation and overgrowth under diffusive growth conditions in the hypo-peritectic region where both, the α-phase and the β-phase grow planar. Such bands were found in experiments where convection is reduced by using thin samples [11, 29], which is explained in detail in chapter 2.4.

Trivedi's model which leads to the formation of alternating bands is described in Fig. 6. The liquidus temperature for a concentration c_0 is given at point a. The concentration in the liquid at the s/l interface follows the liquidus line (1) and increases to reach point (b). The solid concentration follows the solidus line (2) and tries to reach a steady-state growth at point c. Since the transformation from α to β requires minimum undercooling, the liquidus concentration can reach point d, where nucleation of the β-phase is possible. Thus, the β-phase can occur before the α-phase reaches steady-state. Now, if the β-phase becomes the preferred phase, the liquid composition follows the β-liquidus line (3) from point e and further tries to reach point f.

Since the β-phase rejects less solute, the concentration decrease and the temperature increase. It tends to reach steady-state growth condition which is given by the solidus temperature of the metastable β-solidus line, point g, which is above the peritectic temperature. Now, if this liquidus temperature reaches point f, nucleation of the α-phase is possible and the α-phase will become the new preferred phase before the β-phase reaches steady-state growth condition, point i. Once the α-phase forms again, the cycle is repeated and starts again, which leads to the layered microstructures [11].
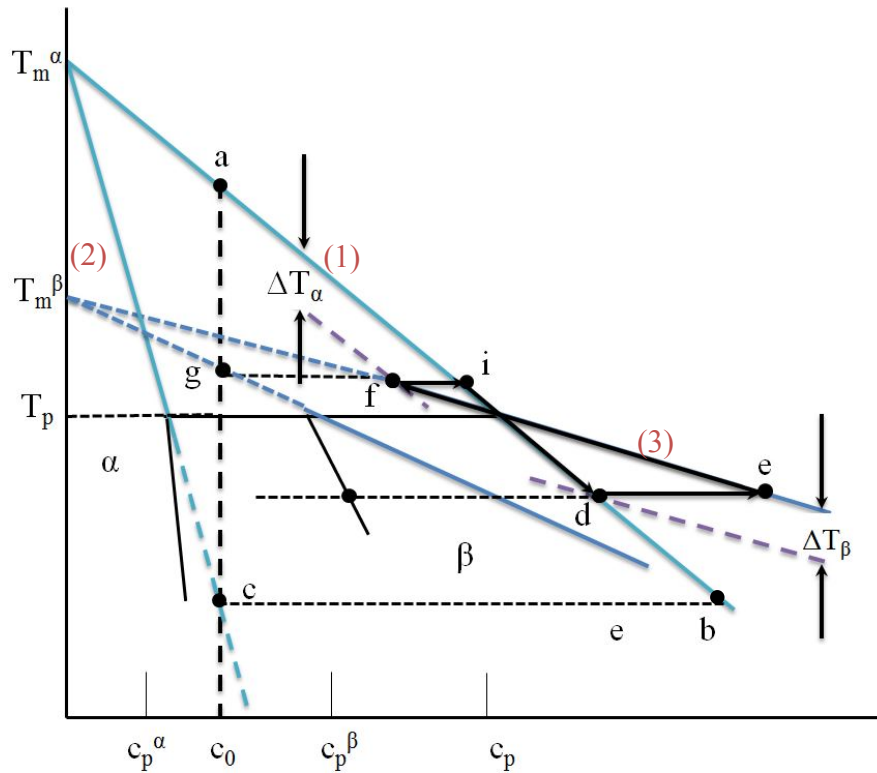
Fig. 6: Schematic illustration of the banding mechanism [taken from Trivedi, 11].

Trivedi's model has to be expanded regarding the influence of existing convection on earth in combination with the simultaneous growth of both phases. A competitive growth occurs as soon as the new phase nucleates at the s/l interface. Fig. 7 shows a sketch of simultaneous growth. Both phases grow against the temperature gradient but additionally, the new phase tries to grow in lateral direction on the interface (a). If the β-phase becomes unstable it comes to the evolution of cells (b). The α-phase can grow in the direction of the thermal gradient, between these β-cells (c). An new sequence of α and β is therfore initiated which leads to island bands or peritectic coupled growth [30].
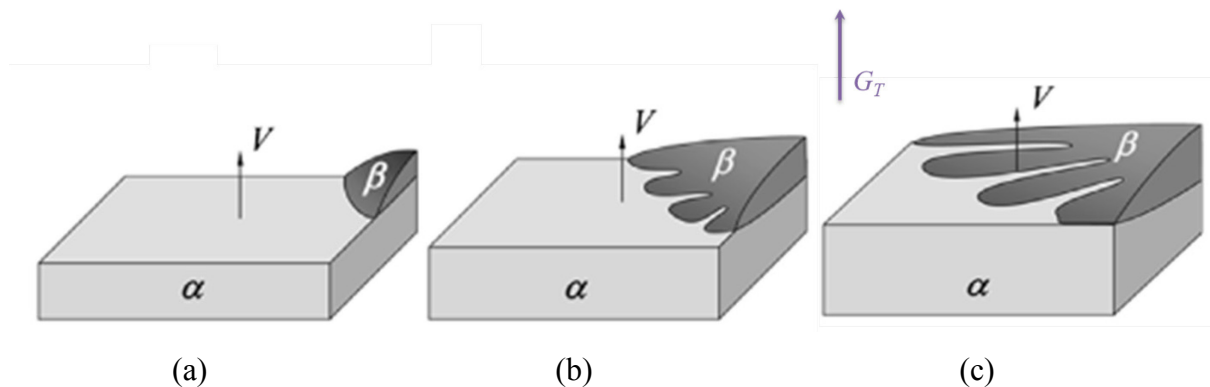
Fig. 7: Sketch of the simultaneous growth of α- and β-phase [30].

Such alternating eutectic-like, two-phase microstructures have been already observed for alloys like Ni–Al [21] and Fe–Ni [31, 32]. Fig. 8 shows a sketch of the possible forms of layered structures: (a) bands, (b) island bands (partial bands) and (c) peritectic coupled growth (PCG) [10, 33, 34]. Whereby isothermal peritectic coupled growth differs from the well-known eutectic growth. Here, in contrast to eutectic growth, the pile-up is not reduced.
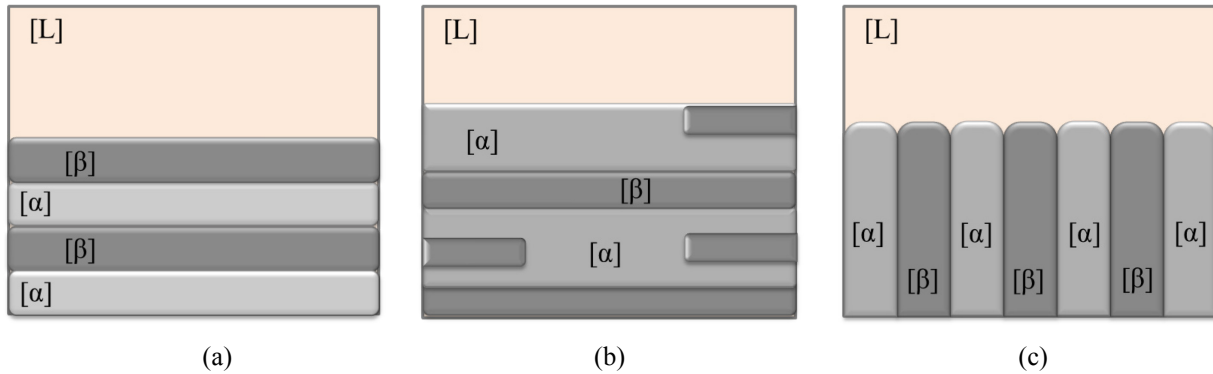

Fig. 8:   Patterns of layered structures in peritectic systems: (a) banded structure, (b) island bands and (c) coupled growth.

2.3 The Peritectic System TRIS–NPG

The knowledge about dynamics during solidification processes of metals is based on the in-situ investigations on transparent, organic, metal-like solidifying substances, so-called plastic crystals. These substances crystallize with high-temperature, non-faceted (nf) phase interfaces which leads to the formation of planar, cellular, dendritic or eutectic solidification morphologies [3–6].

Various transparent organic compounds have been investigated to find model substances that allow a real-time observation of metal-like solidification processes. Several substances have been found which are suitable for the investigation of binary eutectic and peritectic growth. However, just a few substances have been found that show nf/nf reaction with suitable temperature-range for direct observation within a Bridgman furnace.

Based on previous investigations at MUL, the binary organic model system TRIS (Tris-(hydroxyl-methyl)-amino-methane) and NPG (Neopentylglycol), published by Barrio et al.

and Sturz et al. [35, 36], is used in this study. From now on, these substances are designated by the short title TRIS–NPG.

NPG as well as TRIS show nf/nf crystalline phases at high temperatures and a peritectic reaction within a suitable concentration and temperature range. These facts make these components comparable to peritectic metal systems like Fe–C, Fe–Ni, Cu–Sn, and Cu–Zn. A main advantage is that these organic substances enable in-situ observations because the materials are transparent. However, due to this, it is difficult to distinguish between the two phases from one another [35, 36]. The procedure for distinguishing the various phases will be described later. Table 1 shows the chemical and physical properties of the compounds TRIS and NPG [35, 37, 38].

Table 1: Chemical and physical properties of the organic compounds TRIS and NPG.
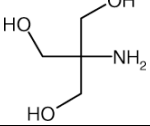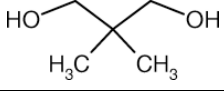
	TRIS	NPG
Formula [37]	$H_2NC(CH_2OH)_3$	$(CH_3)_2C(CH_2OH)_2$
Formula, summed up [37]	$C_4H_{11}NO_3$	$C_5H_{12}O_2$
CAS-Nr. [37]	77-86-1	126-30-7
Structure [37]		
Sigma Aldrich Prod. Nr. [37]	T1503	53.825-6
Purity as delivered [37]	99.9+ %	99 %
Density at room temperature [37]	1.353 g/cm^3	0.980 g/cm^3
Molar mass [38]	121.14 g/mol	104.15 g/mol
T_m (as delivered) [37]	445 - 446 K	398 - 403 K
Low temperature phase [38]	Orthorhombic [O]	Monoclinic [M]
Lattice constants [38]	$a = 8.853$ Å $b = 7.804$ Å $c = 8.800$ Å	$a = 6.019$ Å $b = 10.881$ Å $c = 10.132$ Å $\beta = 100.160$ Å
T_{SST} (s.-s. transition) [38]	406.8 ± 1.0 K	314.6 ± 1.0 K
ΔH_{SST} [38]	34.0 ± 1.7 kJ/mol	12.8 ± 0.6 kJ/mol
ΔS_{SST} [38]	83.7 J/mol·K	40.6 J/mol·K
ΔV_{SST} [38]	5.07 cm^3/mol	4.86 cm^3/mol
ΔH_{SST} [38]	3.7 ± 0.2 kJ/mol	4.4 ± 0.2 kJ/mol
High temp phase [38]	bcc [C$_l$]	fcc [C$_F$]
Lattice constant [38]	6.8888 Å (at 408 K)	8.854 Å (at 353 K)
T_m (purified) [38]	442.7 ± 1.0 K	401.3 ± 1.0 K
ΔH_m [38]	3.7 ± 0.2 kJ/mol	4.4 ± 0.2 kJ/mol
ΔS_m [35]	7.12 J/mol·K	10.8 J/mol·K
ΔV_m [35]	6.63 cm^3/mol	4.86 cm^3/mol
T_b (as delivered) [37]	492 - 493 K (at 13 hPa)	481 - 482 K
ΔS_f [38]	$1.06 \cdot 10^5$ J/K·m	

Fig. 9 shows the peritectic region for the phase diagram TRIS–NPG. The peritectic plateau ranges from $x_\alpha = 0.47$ to $x_L = 0.54$ mol fraction NPG and the peritectic reaction is at a concentration of $x_P = 0.52$ mol fraction NPG [35, 36].
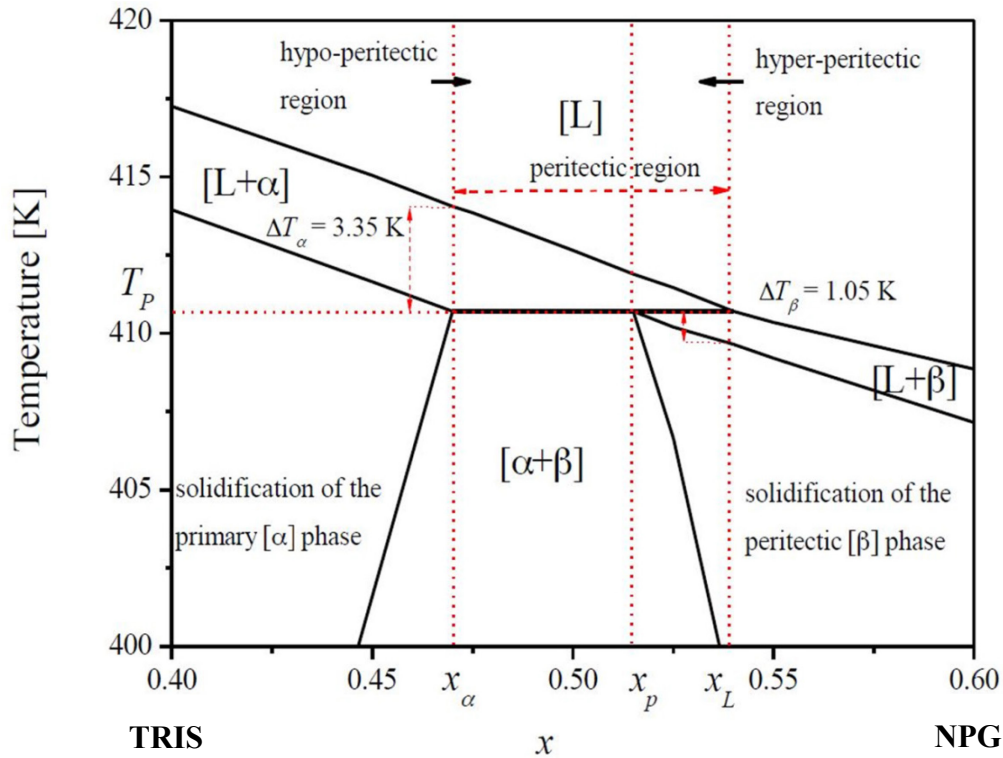
Fig. 9: Detail of the peritectic system TRIS–NPG.

The different morphologies of the system TRIS–NPG, which are obtained up to now, are shown in the microstructure map, see Fig. 10. They have been calculated and detected by in-situ investigations according to [Hunziker et al. 39]. It shows a wide range of well-known structures like cells and dendrites as well as layered structures in form of bands, oscillation coupled growth and peritectic coupled growth (PCG) [17]. The microstructure map was calculated by measuring the diffusion coefficient and the difference between the solidus and liquidus temperature. Layered structures like bands are found for concentrations between $x = 0.475$ and $x = 0.505$ mol fraction NPG and a G_T/v_p ratio from $1.7 \cdot 10^{10}$ to $2.5 \cdot 10^{10}$ Ks/m² [17].
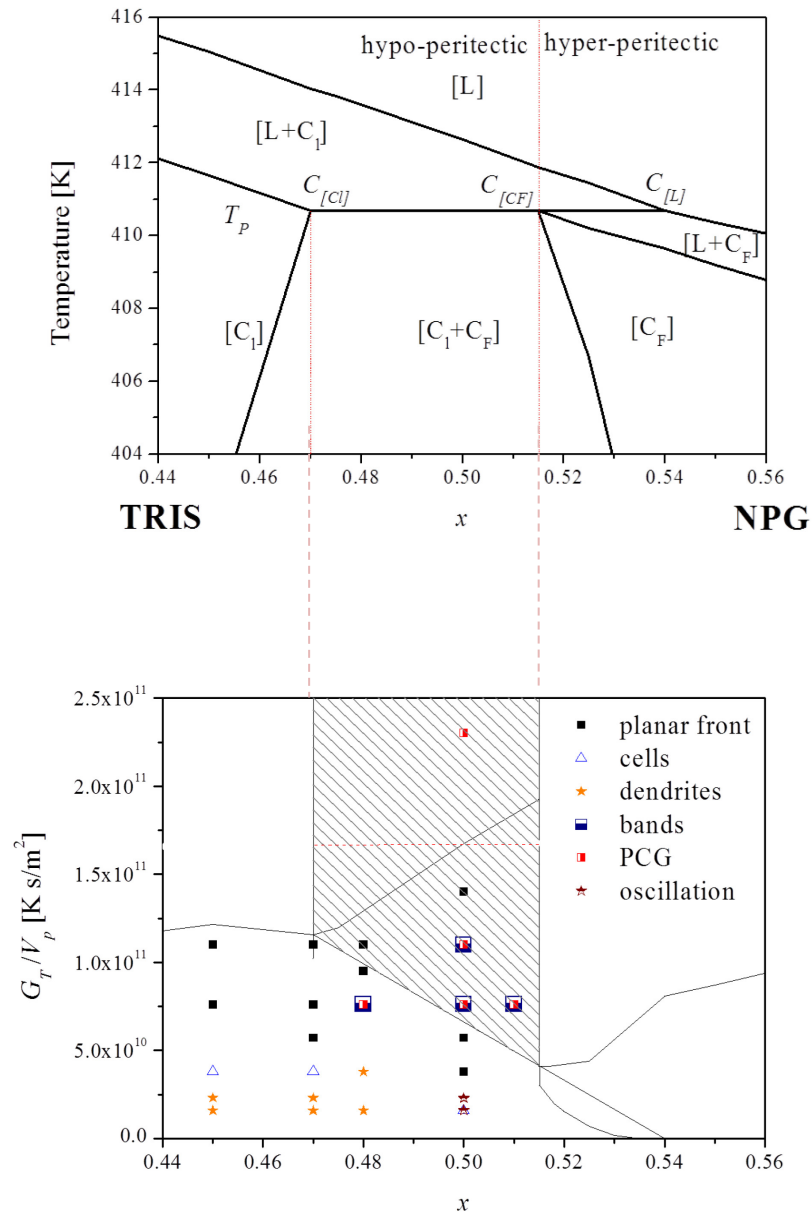
Fig. 10: Phase diagram and G_T/v_P-c diagram (microstructure map) of the system TRIS–NPG. It shows the areas of different morphologies, which are observed up to now at MUL [17].

Optical distinction by colorization

Preliminary tests in the past were made to enable a distinction between the two transparent phases α and β, the binary system was colored with Sudan-red colour.

As a result, there were lighter and darker areas within the mushy zone, see Fig. 11. Comparing the liquid area – which has a dark-red coloration – with the solid area (light-red coloration), it can be concluded, that the dark areas within the mushy zone must also consist of liquid material.

This liquid material is defined as liquid channels (elongated area) and liquid pockets (enclosed liquid which can reach the interface or stay enclosed within the mushy zone). Fig. 11 shows the arrangement. It is assumed, that the liquid material within these liquid material is enriched with NPG.
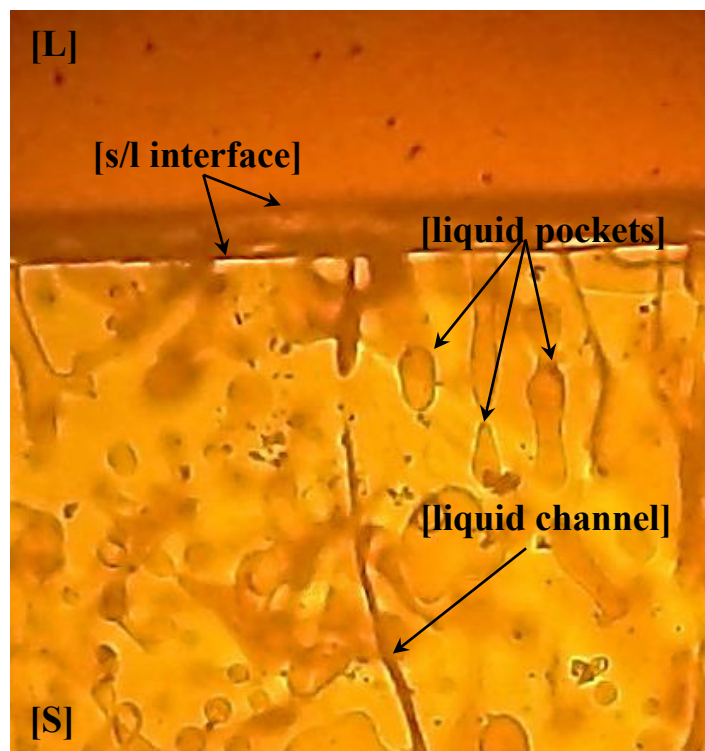
Fig. 11: Picture of an experiment with Sudan-red colour. The darker areas correspond to NPG.

Above the critical velocity in the model system TRIS–NPG

Cellular and dendritic morphologies were observed at low solidification velocities near the limit of constitutional undercooling. Whereby, cellular growth occurs in the transition region between planar and dendritic solidification.

Fig. 12 shows an example of this transition, found in the peritectic system TRIS–NPG. The pulling velocity was kept constant during the entire experiment. After a certain period of time the initial planar front becomes instable and shallow cells start to grow (a). These cells are getting larger (b) and finally transform into dendrites (c) [6].

(a)   (b)   (c)
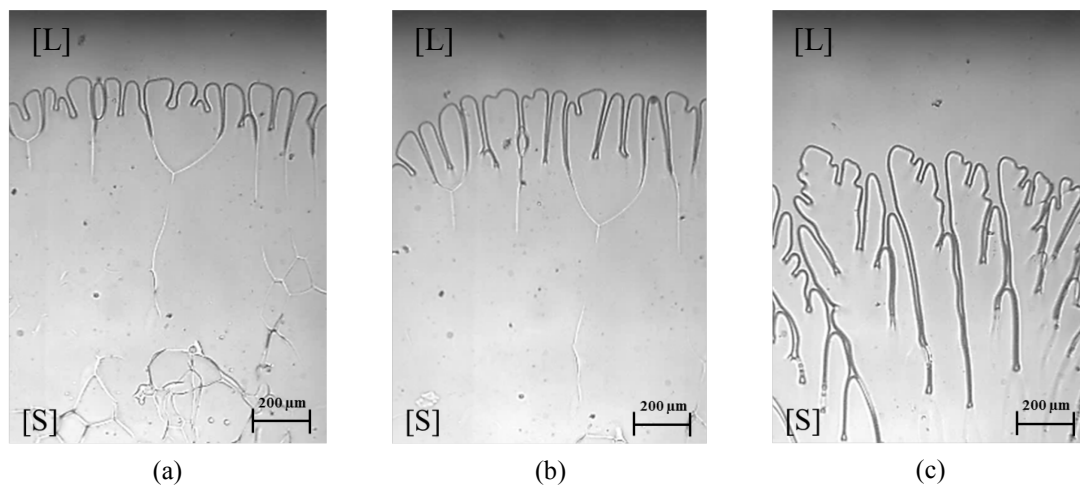
Fig. 12: Transition from cellular growth to dendrites: a) shallow cells, b) deep cells c) dendrites [6]

<u>Below the critical velocity in the system TRIS–NPG</u>

At a solidification rate close to or below the critical velocity, a planar solidification front with simultaneous growth of α and β in form of PCG was observed. Fig. 13 shows an example of this morphology. The left side of the picture shows a curved s/l interface, which is a result of convection within the sample [40].
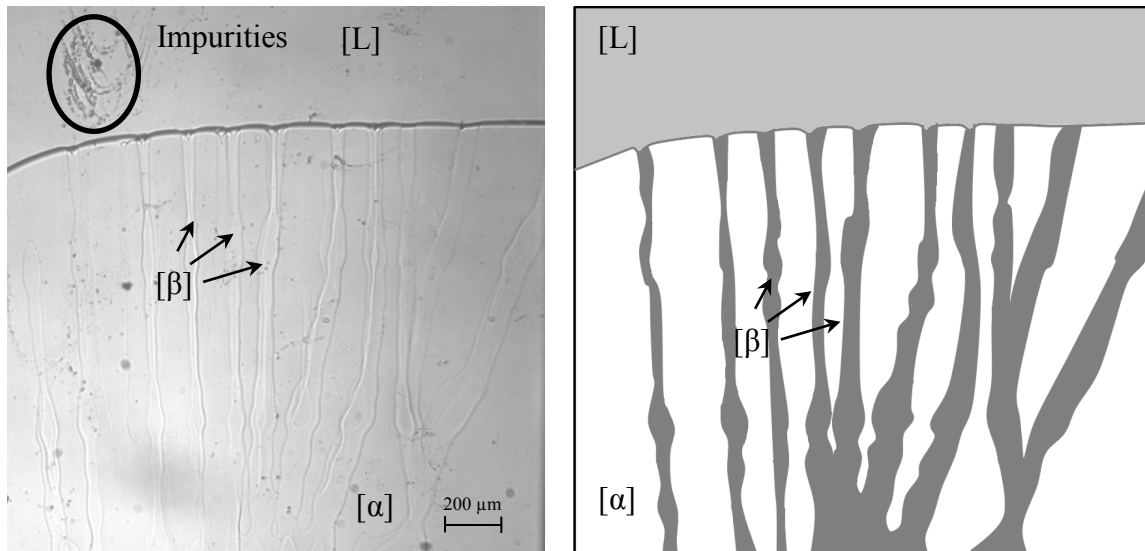

Fig. 13: Example for peritectic coupled growth in the system TRIS–NPG.

Also the transition from island bands to PCG was found in the past for vertical as well as for horizontal solidification experiments. Fig. 14 shows the transition of island bands, which grow first lateral and then transform into coupled growth [17]. Due to the concentration profile in lateral growth direction the interface is again slightly curved. For a better understanding, the pictures are also presented with a sketch. Here, the grey area represents the growth of the β-bands and the white area is the primary α-phase.
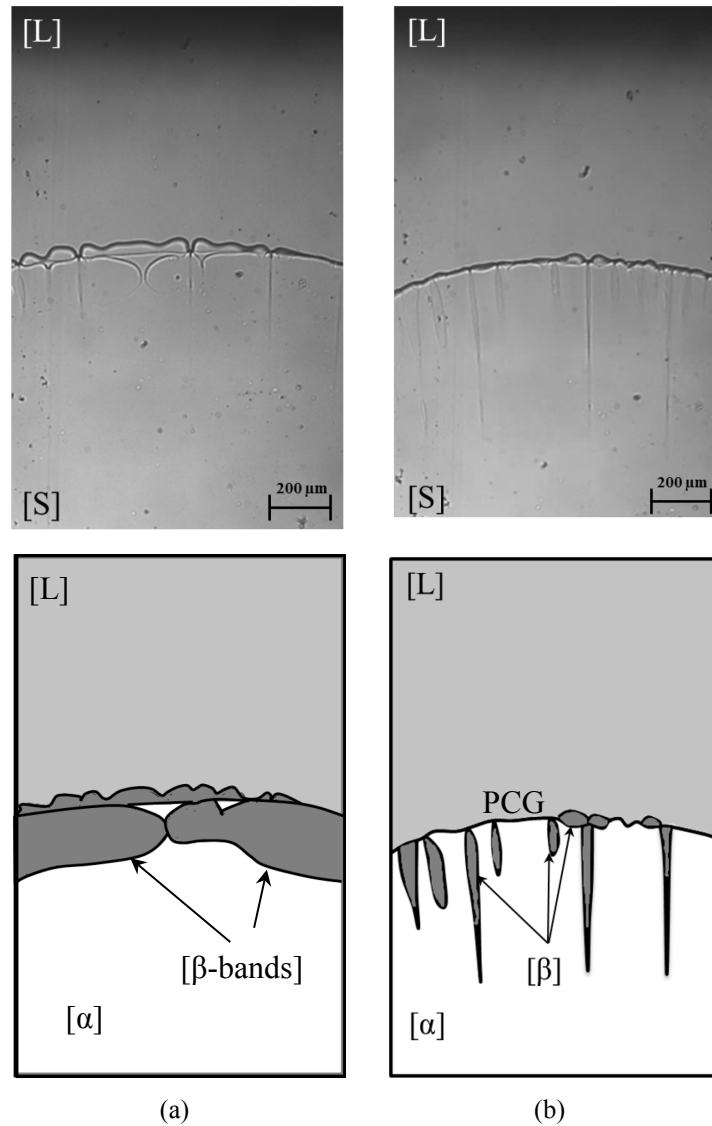
Fig. 14: Transition from parallel bands to coupled growth in a vertical solidification experiment: (a) growth of a band (b) transition to coupled growth begins to build.

PCG can be achieved for two conditions: (i) competition between lateral growth and nucleation through island bands, like it is shown in Fig. 14. This transition is also achieved within horizontal solidification experiments, see Fig. 15. The transition from banded structure to isothermal PCG is initiated by a growth of the peritectic β-phase onto a planar α/l interface, Fig. 15a. The α-phase grows planar e.g. stable until the β-phase forms a new band and nucleate on several positions at the interface, Fig. 15b. This leads to island bands, see Fig. 15c [41]. Finally, the competition between lateral and forward growth of the two phases leads to an isothermal PCG, see Fig. 15d.
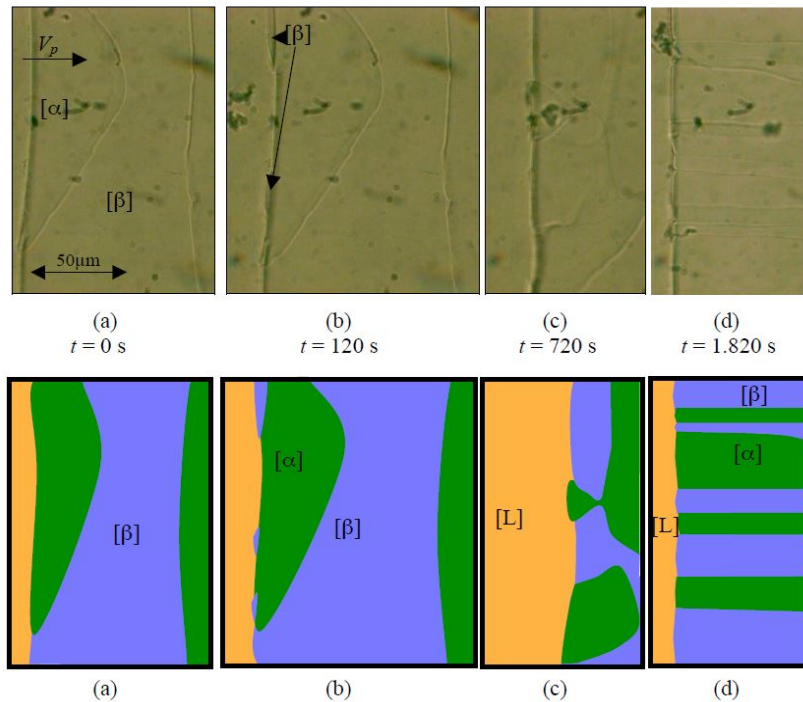
Fig. 15: Transition from island bands to PCG in a horizontal solidification experiment in the system TRIS–NPG [41].

(ii) PCG can also be achieved by reducing the growth rate. For this, the critical velocity will be reduced to a value below. Fig. 16a and b show the transition from α-dendrites to β-cells, both phases grow at a different depth within the sample. This means, that the peritectic β-phase grows 0.8 ± 0.3 K behind the primary α phase. Reducing the growth velocity the two arrays form two different interfaces, α/l interface in the back section and β/l interface in the front section (Fig. 16c). When the interfaces are getting closer to a planar form they start to interact with each other. The α-phase starts to form islands at the β/l interface. Finally there is a transition into α-lamellae, which grow simultaneous with β-lamellae, see Fig. 16d [41].
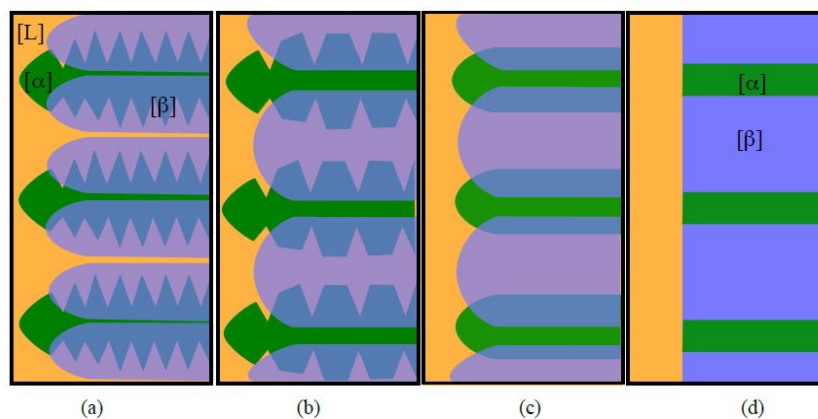
Fig. 16: Development of isothermal PCG by reducing the growth velocity [41].

21

2.4 Convection

Natural convection describes flow in a liquid that occur within a gravitational field, which is the case here on earth. They are produced by density changes of the material due to an applied thermal gradient (thermal buoyancy convection) or a concentration gradient (thermos-solutal buoyancy convection) in the melt and driven by gravity. This section deals with the thermo-solutal convection and its influence on solidification morphology. It is also presented how the fluid flow can be made visible for further investigations.

Fluid flow during solidification

In addition to diffusion, convection is a process that determines heat and mass transfer within the liquid phase. Essentially, convection can be divided into (i) free convection, such as gravity-dependent buoyancy and gravity-independent convection e.g. marangoni convection, and (ii) forced convection. Usually, a combination of more than one of these types can occur within the melt.

Due to the fact that solidification processes always occur in a gravitational field, the thermal and solutal gradients generate natural convection. In recent years, research has focused on the relationship between convection and solidification morphologies [42–45].

For direct solidification processes with the Bridgman method, the effect of gravitational force and rejected elements ahead of the solidification front influences the occurrence of the existing fluid flow. During solidification, the lighter components of the alloy might pile-up in front of the s/l interface (see chapter 2.2). Due to this phenomenon, an upward movement is induced. In the case that the heavier element is rejected, the gravity counteracts the diffusion direction.

Thermo-solutal convection can be greatly reduced by using small containers. Trivedi and Park published a description of this effect for layered structure formation. Investigations with metal bars of different diameters solidified with the Bridgman method were carried out [47, 48]. It was found that the formation of banded structure mainly depends on the composition, the ratio of G_T/v as well as on the sample size. Here, the formation of two-phase patterns for the peritectic alloy system Sn-Cd was investigated. They show complex microstructures in both diffusive and convective regimes.

(i) For peritectic systems with two-phase microstructures, fluid flow creates a new class of microstructures that are not predicted in the diffuse growth regime. For hypo-peritectic alloys, diffusive growth allows the evolution of discrete bands of the two phases, while fluid flow causes only a transition from the primary α-phase to the peritectic β-phase. In contrast, diffusive growth in hyper-peritectic alloys predicts only a transition from the primary to the peritectic phase, whereas the presence of fluid flow results in a continuous oscillatory structure of the primary phase embedded in a peritectic phase matrix. Systematic experiments in samples of different diameter showed that diffusive growth, for example in the Sn-Cd system, can be obtained in samples with diameters of less than 1.0 mm [47–48].

(ii) To reduce the effect of convection concerning the microstructure, samples with small diameter were used for hyper-peritectic alloys. Discrete bands of alternating phases perpendicular to the direction of growth were found. It is shown that banded structures are formed only in a small range of alloy compositions. From this banding composition window, the banding cycle, explained in chapter 2.2, was published. The undercooling, which is required for β-phase nucleation, was determined to be 1.0 K, and for the α-phase nucleation it was determined to be 0.2 K. This was the first quantitative experimental study to determine the undercooling of nucleation in directional solidification experiments [47–48].

(iii) It has been shown that the development of these microstructures is determined by the competition of the nucleated β-phase and the primary α-phase, which leads to the formation of layered microstructures. The growth competition depends on the diameter of the sample, the growth rate and the composition [47–48].

(iv) These experimental studies have provided an understanding of the different microstructures that can form in a diffusive regime when only a single nucleus of the new phase forms at the wall/solid/liquid interface which then spreads laterally, see Fig. 18 [47–48].

The experimental results from Trivedi for very thin samples are shown in Fig. 17. They were gained under diffusive regimes. Microstructure (f) is a novel microstructure, which requires the presence of oscillatory convection in the melt for formation. For this study, only (a)–(d) are of interest. Diffusive growth was observed in very thin samples with a diameter smaller than 10 mm diameter. The flow intensity was found to increase with increasing sample

diameter in thick samples with a diameter of larger than 10 mm. Thus, the influence of convection can be related to the sample diameter [47–48].
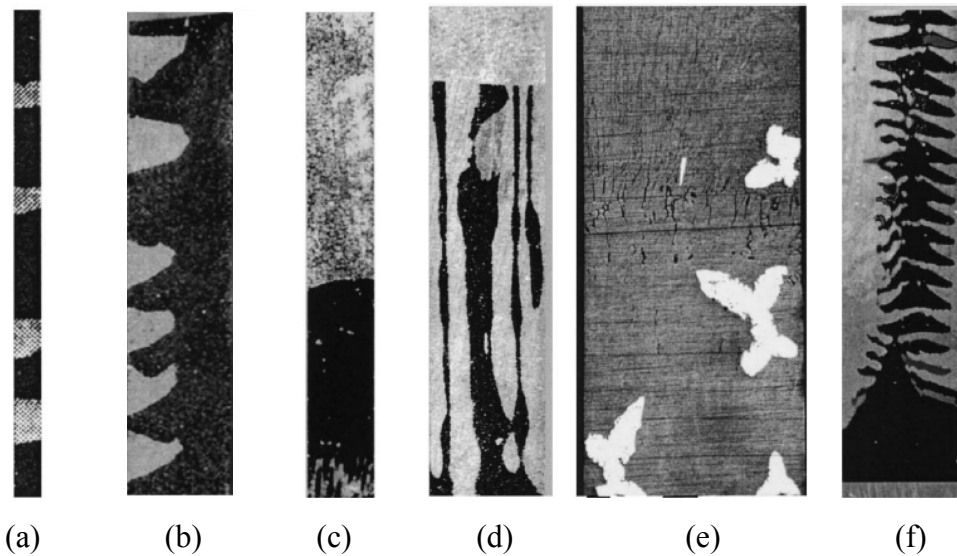

<div align="center">(a)   (b)   (c)   (d)   (e)   (f)</div>

Fig. 17: Published flow controlled microstructures in peritectic alloys [taken from Trivedi, 47]: (a) discrete bands (b) partial bands or rather islands (c) transition from primary to peritectic phase (d) simultaneous growth (planar interface) (e) dispersed phases due to nucleation in front of the s/l interface (f) tree-like, oscillating structures with the β-phase embedded in the primary phase [47].

This limitation is based on small diameter samples which are required to obtain diffusive growth condition. In samples which are larger, more nuclei can grow at the same time. For this purpose, the distance between two nuclei can be controlled by nucleation rate which thus defines the microstructure [47].
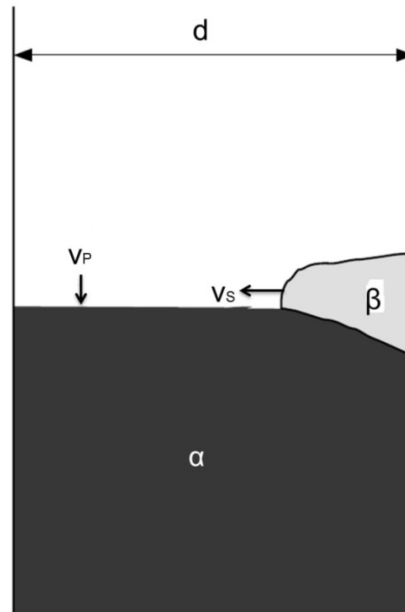
Fig. 18: The formation of the β-nucleus at the wall/solid/liquid junction, and growth of the β-phase. The α-phase also grows upwards as the β-phase spreads laterally.

According to the publication of [47], in this study, very small glass tubes were used to suppress convection and to obtain layered structures.

Simulation of solutal capillary convection and channel segregation

The area in which both phases, liquid and solid, coexist during solidification is called mushy zone [24]. The microstructure that forms within the mushy zone is characterized by a solid dendritic structure with discontinuous liquid droplets/pockets and/or continuous channels. These liquid pockets and channels influence the mechanical properties. A solid material with liquid channels and/or droplets may lead to reduced strength. At the end of solidification, when the last liquid consists of elongated liquid channels, the mushy zone can no longer be compensated by feeding. Therefore it is stated that such liquid channels and droplets are critical at the end of solidification [49].

However, at the end of solidification, when the last liquid is present in form of very thin liquid channels, an opening of the mushy zone can generally no longer be compensated by feeding with liquid. It can be concluded that the morphology of the liquid channel is critical in the last stage of solidification, especially in thin areas at the roots of liquid channels and at the grain boundaries (GBs) [49].

A picture of flow pattern for a dendritic morphology is shown in Fig. 19. It shows a very strong fluid flow out of the mushy zone into the liquid [49].
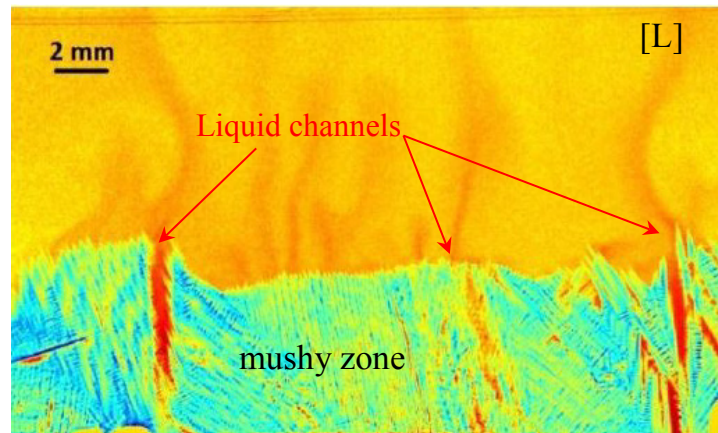

Fig. 19: Example of a simulation of dendritic structures including liquid channels from a solidification experiment. There is a strong flow out of these channels [49].

The segregation of solutes, results in grain boundaries (GBs). These boundaries depend on the arrangement of solidifying grains, referred to as divergent or convergent growth. Also the misorientation angles have an influence, see Fig. 20. For small angular misalignments, the grain boundary segregation and the energy of misorientation are connected. To compress the influence of segregation, also phase field simulations were used [49, 50, 51]

It was found that divergent growth results in a higher separation of solutes at inter-dendritic channels than convergent growth. This is due the lateral diffusion within the liquid ahead of the dendritic solidification interface.

Convergent dendrites which grow towards each other, show a strong interaction of solutes and a higher amount of solutes in front of the tips, which leads to diffusion in lateral direction. In contrast, divergent primary dendritic structures grow in the opposite direction. This creates a solute mass sink to diffuse into the space between the dendrites. Either convergent as well as divergent bi-crystal growth cases are also inflected by the misorientation angle [52].

The field in front of divergent/convergent dendrites depends also on divergent cases of orientation-dependent prime distance and side branch growth.
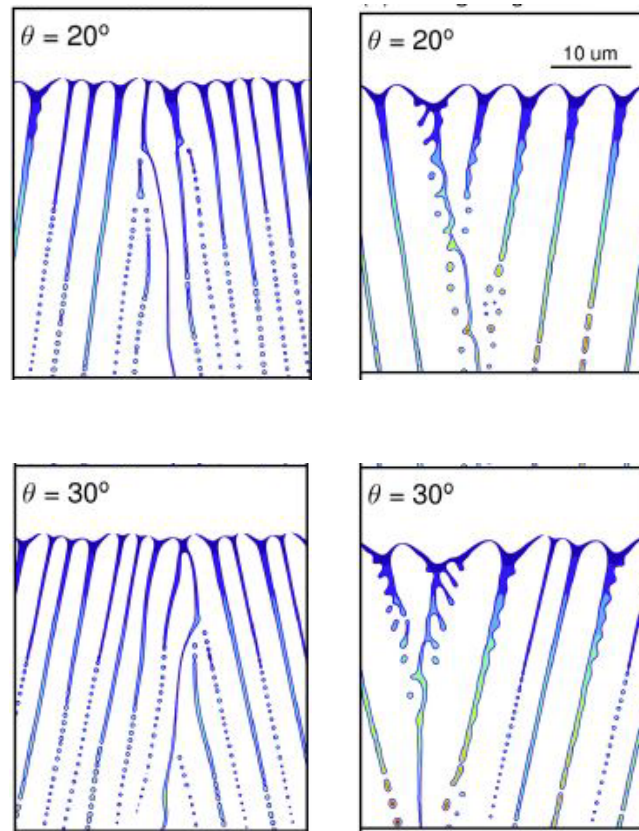
Fig. 20: Solutal distribution within liquid channels in two-crystal columnar growth of a simulated Al-2.0 wt.% Cu alloy for two misorientation angles for convergent and divergent growth [52].

It has to be mentioned that realistic simulations concerning segregation are still difficult. In fact, for such simulations a sufficient description of the microstructure parameters such as the kinetic coefficients, anisotropy parameters and interface width are required. In fact, such information's are hard to obtain.

As a rule, simulations in simple cubic or cylindrical domains are carried out. These simulations are usually limited to thermo-solutal convection which is unstable. Furthermore microstructure characteristics are mostly neglected. Due to the spatial resolution of a defect which is in the order of the primary dendrite arm spacing, the simulation in 3D is a very demanding and time consuming process [52].

In this study, the influence of convection during the first stage of solidification, more particularly, its influence on the s/l interface shape and solute distribution in the liquid phase will be investigated without simulation.

Visualisation of the convection

In order to make statements about flow pattern ahead of the transparent s/l interface, in this study, convection has to be made optical visible. This is done by using tracers.

The selection of such particles according to the used organic material depends on a lot of factors which influence the interaction between liquid and particles. They should be designed in a way so that they can follow the convection without affecting it. The movement of the tracers can be followed either with a suitable software, called Flow manager, which can represent the flow with vectors, or manually, by following each particle individually. The range of products which are available for this study is presented later on.

The main factors, which should be taken into account by choosing the right particles are:

- the size and size-distribution of the particle,
- the density ratio between particle and fluid and also
- no chemical reactions between the tracers and the organic substances [53].

Velocity of a particle within a fluid

For the determination of the sinking velocity of a particle within a liquid, the following equations are given. A sufficiently small and spherical particle with a diameter d_P, which is located in a viscous fluid with the dynamic viscosity μ falls due to the gravity g with the speed

$$U_g = d_P^2 \cdot \frac{\rho_P - \rho_L}{18\mu} \cdot g \qquad (8)$$

to the ground.

The formula can be used to estimate the particle velocity but only under the condition of very small Reynolds numbers ($Re \ll 1$), which is the case here in this study [54].

$$c_d = \frac{24}{Re} \qquad (9)$$

where C_d is the drag coefficient and Re is the Reynolds number.

3. Experimental Set-up

This chapter covers the experimental implementation. First, the functionality of directional solidification using the Bridgman technique is explained. Further on, the density determination for the liquid components is discussed, and finally, the sample preparation is described.

3.1 Directional Solidification

In this study, directional solidification is carried out by using a Bridgman furnace. Fig. 21 shows a sketch of the Bridgeman furnace. Here, a long rectangular sample is moved vertically with constant pulling velocity through the furnace. The cooling and the heating plates are separated by an adiabatic gap. Rectangular glass samples filled with alloy, described in chapter 3.3, are moved through the temperature gradient within the adiabatic zone. The temperature in the hot and cold zone is selected in such a way that the s/l interface is within the observation zone. To avoid a loss of heat to the surrounding, the whole furnace is isolated by ceramic shelters. The sample is illuminated through glass windows in the ceramic plates at the adiabatic zone to observe the morphology of the s/l interface with a ZEISS microscope. The movement of the glass sample through the furnace is PC-controlled. Pictures were recorded simultaneously with the involved temperatures every 30 seconds. The objective of the front is connected to a CCD camera and a storage system [55].
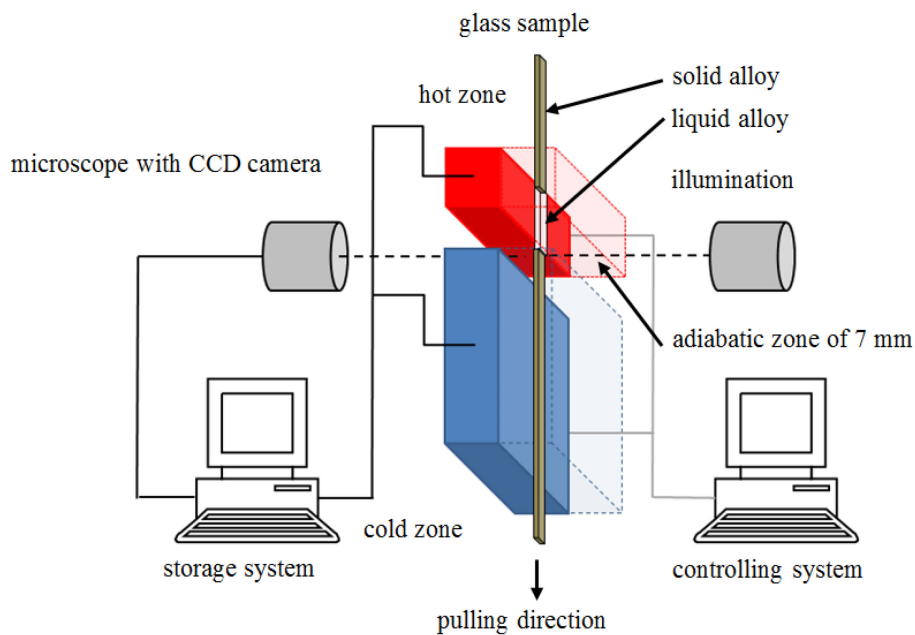
Fig. 21: Sketch of the Bridgman furnace [55] (left side) and open Bridgeman furnace (right side).

Fig. 22 shows the complete set up for the investigations. The unit of the furnace with the ceramic shelter including the hot and cold plates and also the sample corresponds to the violet area in this picture. The thermos-control unit (green area) serves for the temperature control of the hot and cold plate within the furnace.
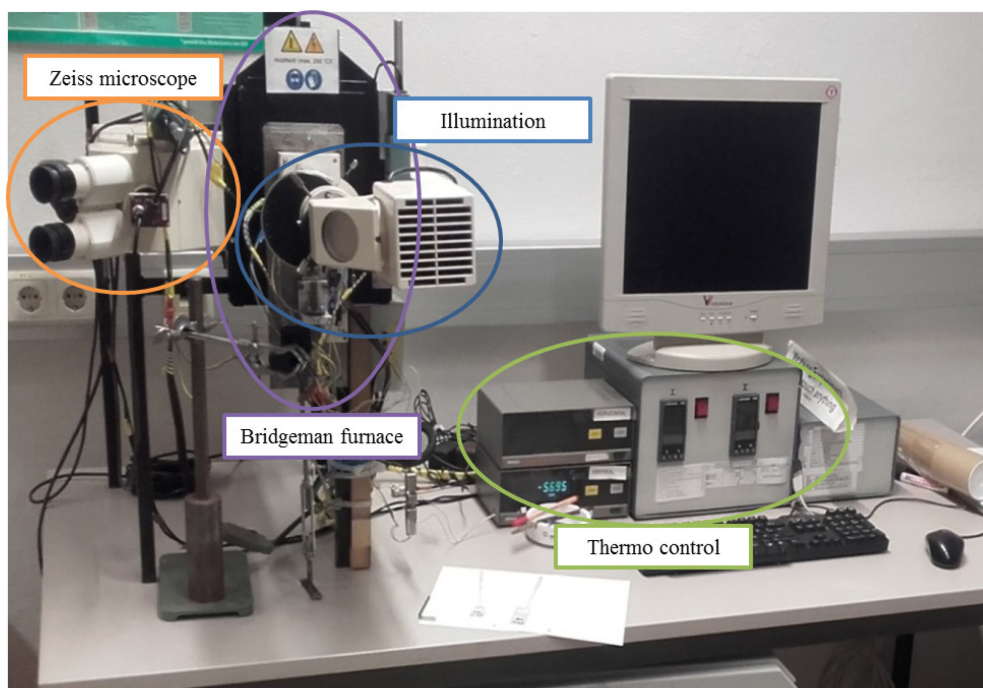
Fig. 22: Entire testing unit consisting of the Bridgman furnace.

The temperature gradient within the adiabatic area was controlled by the selected temperature in the hot and cold zone of the furnace. An average temperature gradient of G_T =5.6 K/mm was determined by moved samples equipped with a thermo-sensor, shown in Fig. 23.
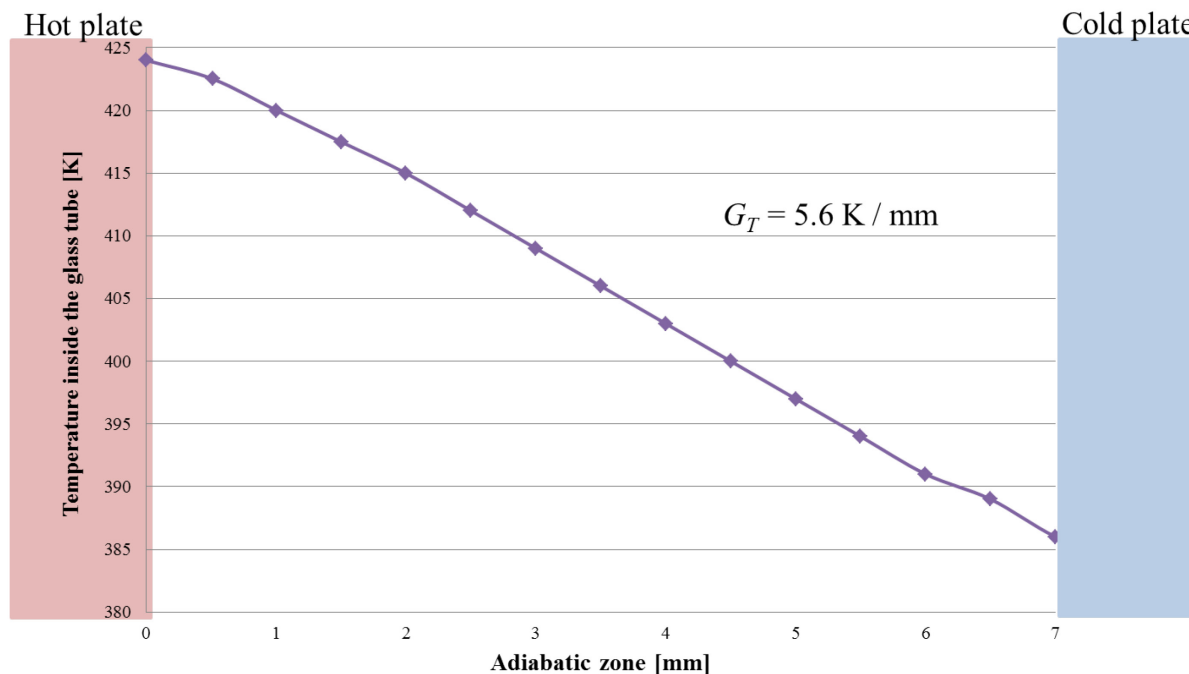
Fig. 23: Measured temperature gradient G_T within a sample.

Seeding particles

A requirement for the tracers is an equal density as the liquid organic material. Since the density of the organic substances depends on the temperature it is hardly possible to exactly match the specification. Up to now, no associated tests were carried out in the liquid state of the system TRIS–NPG, therefore, it was necessary to determine the density within this work.

The density is a function of temperature and with increasing temperature the density of liquids decreases. Hence, for the investigations with tracers it is necessary to know the value for 433 K ± 5K. Since NPG has the tendency to sublimate (even at room temperature), the determination needs to take place in a closed vessel to avoid a loss of mass. For this the method of volume measurement was selected.

The density of the solid organic substances can be calculated according to following equation:

$$\rho_{ges} = \frac{m_1 + m_2}{\left(\frac{m_1}{\rho_1} + \frac{m_2}{\rho_2}\right)} \tag{10}$$

Where, ρ_{ges} is the density of the mixture, m_1 is the molar mass of component 1, m_2 is the molar mass of component 2, ρ_1 is the density of component 1 and ρ_2 the density of component 2.

Table 2 shows the published properties of the substances and the calculated density of an alloy with $x = 0.5$ mol fraction NPG by using equation 10.

Table 2: Properties and calculation of the mixture-density for $x = 0.5$ mol fraction NPG [5].

		TRIS	$x = 0.5$	NPG
density (293,15 K)	[g/cm³]	1.350	1.15	0.980
density (401,15 K)	[g/cm³]	-	1.036	1.06
molar mass	[g/mol]	121.14		104.15

For these investigations an alloy of $x = 0.50$ mol fraction NPG was prepared and then the material was put into a volumetric flask. The filled flask was placed on a heating plate to melt the mixture. During the melting process, solid alloy was added to reach the volume mark of the flask exactly. Afterwards, the mass of the filled flask was determined.

Fig. 24 shows the equipment as well as the implementation of the test. For this experiment an electronic analytical balance "Kern 440-35N", a volumetric flask with a volume of 50 ml and a heating plate were used. . Finally the density was calculated according to:

$$\rho_{m,l} = \frac{V_{alloy}}{m_{flask\,filled} - m_{flask\,empty}} \tag{11}$$

<div align="center">(a)   (b)</div>
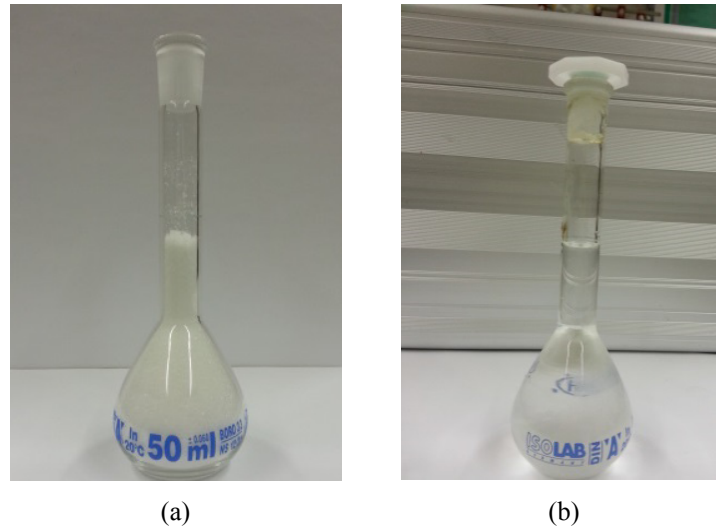
Fig. 24: Determination of the density using a volumetric flask: a) flask filled with powder material b) obtained volume of the mixture at $T = 433$ K.

Table 3 shows the results of the tests obtained out of 3 experiments. For an estimation of the particle density the accuracy of this value is sufficient. The mass resulted from the initial weight of the alloy. By filling the flask with the alloy, a defined volume was obtained.

Table 3: Determination of the density

	Flask empty [g]	**Flask filled** [g]	**Mass m** [g]	**Density $\rho_{m,l}$** [g/cm³]
	38.330	90.130	51.800	1.036
	38.400	90.260	51.860	1.037
	38.340	90.020	51.680	1.034
average	38.357	90.137	51.780	1.036

Within this project only commercial available tracers are economically justifiable. The company "Dantec Dynamics" offers a variety of tracers, see Table 4.

Table 4: Product range of seeding particles [56].

	PSP Polyamide seeding particles	HGS Hollow glass spheres	S-HGS Silver-coated hollow glass spheres	FPP Fluorescent polymer particles
Mean particle size (µm)	5, 20, 50	10	10	10, 30
Size distribution	1 - 10 µm 5 - 35 µm 30 - 70 µm	2 - 20 µm	2 - 20 µm	1 - 20 µm 20 - 50 µm
Particle shape	non-spherical but round	spherical	spherical	spherical
Density (g/cm3)	1.03	1.1	1.4	1.19
Melting point (°C)	175	740	740	125
Refractive index	1.5	1.52	–	1.479
Material	Polyamide 12	Borosilicate glass	Borosilicate glass	Poly (Methyl methacrylate) (Labeled with Rhodium B)

According to the selected experimental investigations in a temperature range of 433 ± 15 K the tracers has to be thermal stable. The organic alloy shows a density of $\rho_L = 1.036$ g/cm^3 at this temperature, therefore, polyamide seeding particles (PSP) and hollow glass spheres (HGS) are at the same range of density and are tested.

Fig. 25 shows a REM picture of the shape of the PSP and HGS particles. The polyamide seeding particles are globular and microporous. The hollow glass spheres are made of borosilicate glass. The particles have a spherical shape and a smooth surface [56].

(a)   (b)
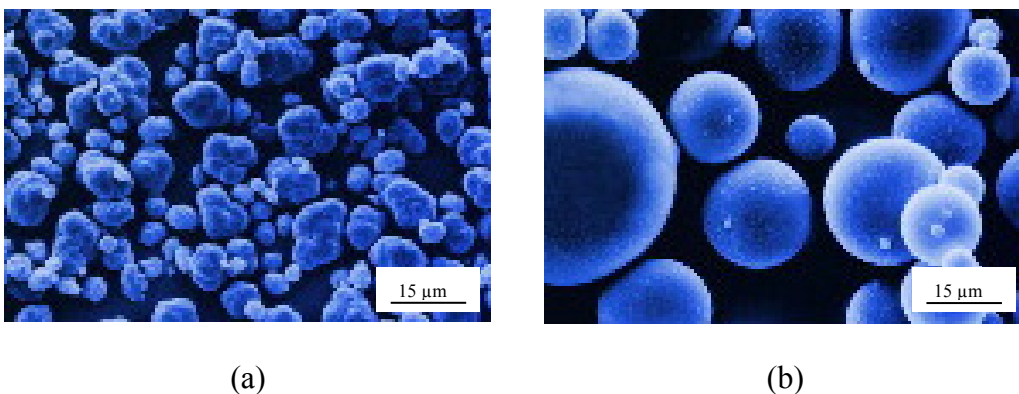
Fig. 25: REM-Picture of the shape of (a) Polyamide seeding particles and (b) Hollowglass spheres [56].

3.2 Particle Analysis

To test the behaviour of the tracers within the liquid, preliminary experiments were carried out with both. The results are shown in the following.

<u>Investigation with PSP Particles</u>

The seedings were delivered with a particle size of 45 µm and a size distribution between 30–70 µm. The melting point of the particles is 448 K. The highest temperature in the experiment is on the hot plate with approx. 426.2 K. Normally, the material should resist the thermal load. The sample was moved through the furnace with a pulling velocity of $v = 0.174$ µm/s.

Fig. 26 shows the results. The PSP particles were easily recognizable because of the large size, which facilitated the evaluation. In general, only a few particles were visible within the observation window. It can be seen that there exist some kind of conglomeration of particles, see particles 1, 2, 3 and 4. Some particles seem to be deformed which may be an indication of thermal load, see particle 5. The particles show not really a downwards movement within the sample since the densities of the fluid and the PSP particles are nearly the same.

| (a) | (b) | (c) |
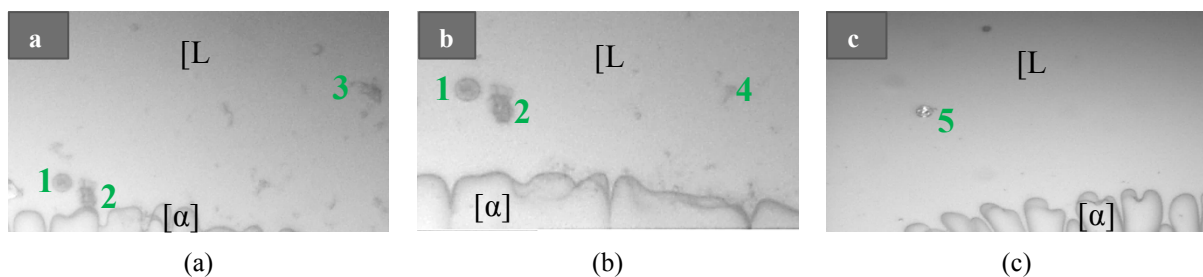
Fig. 26: Preliminary experiment to investigate the behaviour of the PSP particles within the melt: (a) and (b) the particles 1,2,3 and 4 seems to be clustered with other particles (c) the shape and colour of particle 5 differs from the otherwise round shape of the particles.

Investigation with HGS Particles

Fig. 27 shows the test with the hollow glass spheres. The particles are produced with a diameter of an average distribution size of 2–20 µm. Since the density of the tracers is a bit higher than the density of the liquid, a downwards movement was observed. The melting point is with $T = 1013$ K high enough to be unaffected by the thermal load. Also no conglomerates were found within the sample. Due to the fact that for both experiments 0.01 g Particles were added, here, more particles are within the sample due to the smaller size of these particles. As a result, flow patterns can be better represented. On the other hand the evaluation requires more precision.
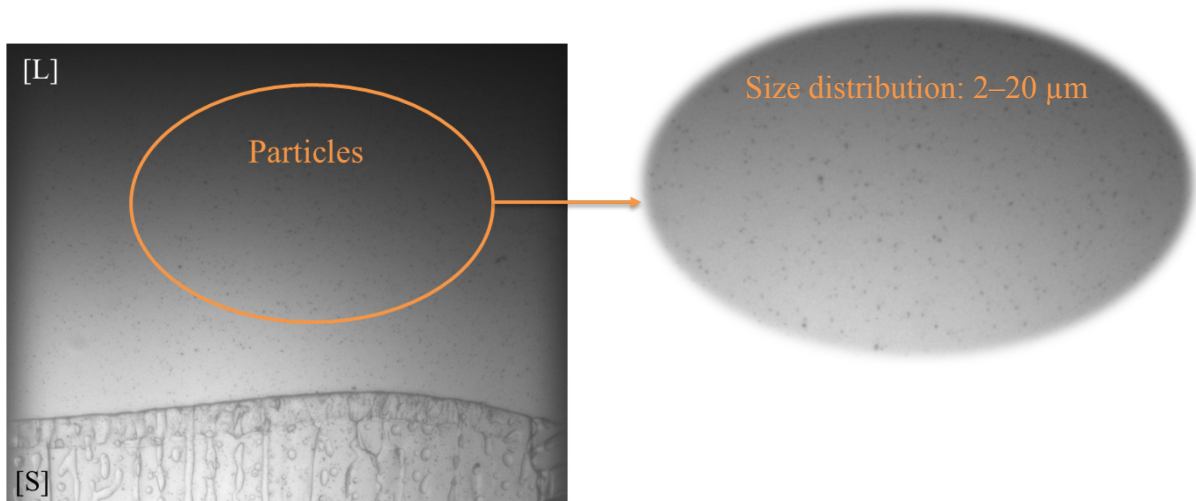
Fig. 27: Preliminary experiment to investigate the behaviour of the HGS particles.

Comparing the physical properties of both tracers, the HGS particles are finely distributed and not sensitive to thermal load. Therefore, the HGS tracers are selected. Due to the differences in density and the observed downward movement, an additional experiment with a sample in rest was carried out in order to determine the rate of descent without any other motion.

3.3 Evaluation Method

Original, the seeding particles from Dantec dynamics are designed for **P**article **I**mage **V**elocimetry (PIV). The software deals with the creation of vector maps [56]. Pictures are taken within a short time interval of less than 0.1s and the motion of the particles is calculated by comparison two subsequent pictures, called double image. First the evaluation of the particle motion via PIV software was tried. It became obvious, that the software did not recognize the particles correctly. This is probably because:

(i) the software is mainly designed for fluorescent tracers which are made luminous by laser. In the experimental setup a laser is not scheduled. This would be beyond the scope of this study. So the particles where just illuminated by normal light.

(ii) Impurities in the sample cannot be prevented because of the small size of the glass tube. There may be some dirt in the inside of the sample which can look like a seeding particle. Usually they did not reveal the same density like the fluid or the particle so the movement differs from the movement of the particles. Unfortunately, the program was unable to distinguish between impurities and particles which cause very diffuse results with too many vectors, see Fig. 28.

(iii) the program deals with the output of vectors. It calculates $\varDelta t$ between a picture and the subsequent picture. There are several different settings like the "auto correlation" or "particle tracking". The interval between each picture of our experiments is 30 seconds. The evidence suggests that this is likely a too big time window. After 30 seconds, the program can no longer assign the vector to the correct particle. Ideal would be a time interval of 1 second. The relevant experimental observation time was approx. 10 hours, which would require a storage of 360.000 pictures equal to 1.7 terabyte memory.
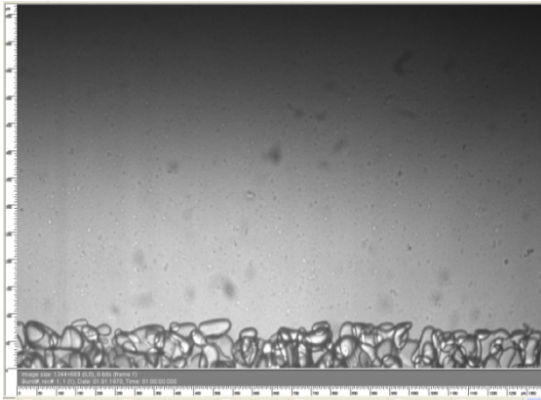
Original Image in "Flow Manager":

To output a vector with the PIV-Software it is necessary to make a "double image", which means that 2 subsequent pictures were connected.
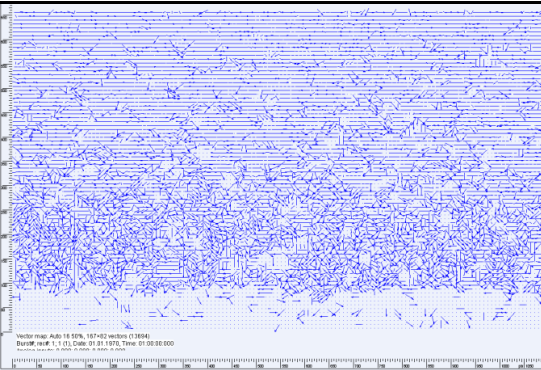
Evaluation with "Flow Manager":

The program creates so called Vector maps. The first picture shows the input "Autocorrelation". The picture below shows the "particle tracking". It can be seen that the vectors were distributed very confused and incoherently in both cases. This is probably because there is too much impurities and too much particles are present.
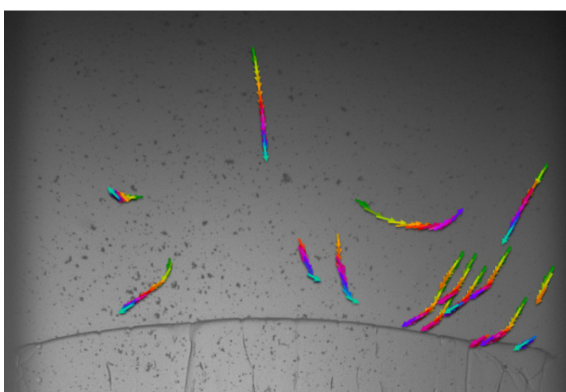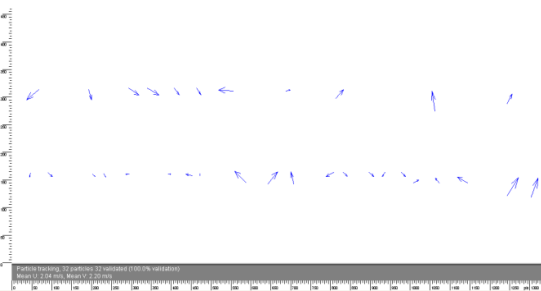
Optical evaluation:

Selected particles which had approx. the same size were followed by naked eye for every single picture. Afterwards the individual "vectors" were overlaid to a complete picture so that the whole movement can be observed. The disadvantage here is the inaccuracy because of optical investigation which is complex.

Fig. 28: Methods for particle investigation.

Hence, the evaluation of the flow, finally, had to be made by optical investigation. Due to this, the procedure is explained in Fig. 29.

A certain particle was recognized at some position 1, see Fig. 29a. In the following picture – after 30 seconds – the same particle moved to position 2, see Fig. 29b. To visualize this movement, the distance between the two positions was marked with an arrow between position 1 and 2, Fig. 29c. For every specific time step, the arrows where marked with a certain color, so it is ensured that each particle can be assigned to a given time. Since the particles move in an ensemble, each particle could be safely assigned to the next image. With this kind of "vector-map", see Fig. 29d, conclusions about convection within the sample can be drawn.
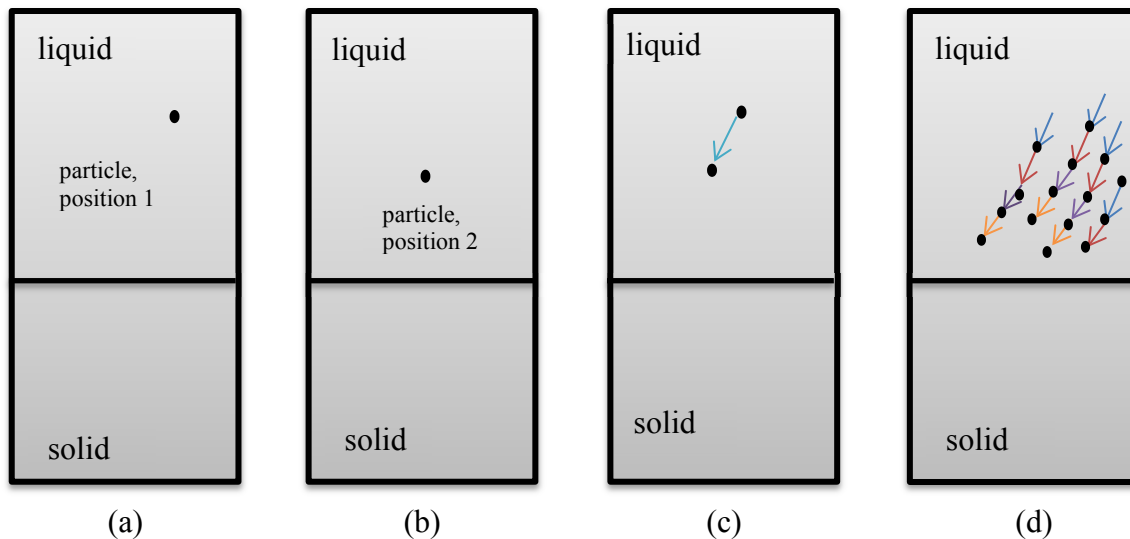
Fig. 29: Sketch of the procedure for optical investigation of the flow with seeding particles.

3.4 Sample Preparation

The organic peritectic region of the model system TRIS–NPG, varying from $x = 0.47$ to $x = 0.54$ mol fraction [35], was examined. For this, the pure materials were obtained as a powder, NPG with a purity of 99% and TRIS with 99.9^+ %. Both substances are highly hydroscopic [57].

The alloys were prepared within a glove box under argon atmosphere to avoid any reaction with oxygen and humidity. The powder was filled within a small glass sample and heated up until the material reached the liquid state. Due to the different melting points, NPG melted

first and then TRIS went into solution. To avoid sublimation of NPG the glass sample was closed during the whole process of melting. Afterwards the sample was cooled down to room temperature without any additional cooling methods. Finally, the alloy was grounded to powder and mixed with 0.1 g ± 0.01 g HGS particles and stored for further use in a new glass container. The preparation of the organic compounds was published in details in [17].

For the solidification experiments glass samples in form of rectangle quartz tubes with the inner dimensions 100 μm depth, 2000 μm width and approx. 15 cm length were prepared. These quartz tubes are called 2D. The method of preparation is shown in Fig. 30.
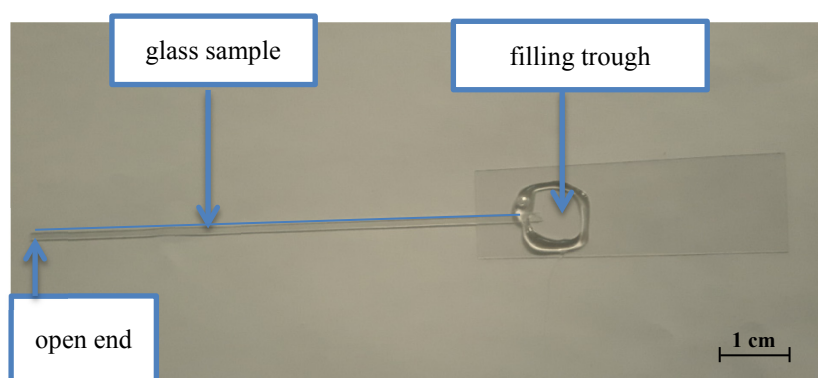
Fig. 30: Glass sample with filling trough, ready for filling.

For filling, the samples were placed on a hot plate in such a way that the area with the filling trough was heated on the plate and the open end of the sample was approximately 1 cm outside of the hot plate. To bring the alloy in the samples the prepared organic compound was put into the filling trough.

As soon as the compounds melted the sample was filled automatically by capillary force. This force sucks the liquid organic compound into the glass sample till the end of the hot plate was reached. When the glass sample was filled, it was slowly drawn from the heating plate and the material was quickly solidified. The glass plate with the filling through was broke off and both ends of the tube were sealed with a hardening glue to avoid any evaporation while heating in the furnace.

Finally, the end of the glass sample was glued again on to a new glass plate, which enables the fixing of the glass sample within the pulling system in the Bridgman furnace.

Fig. 31 shows an example of a filled sample adjusted within the (open) Bridgeman furnace. The brass-like area includes the hot plate and the cold plate. The gap between those two plates is the adiabatic zone. The sample is fixed within a small slot and is connected to the engine, which can pull the sample both upwards or downwards with a constant velocity. The temperature sensors are installed on the hot plate as well as on the cold plate to measure the temperature during the experiment.
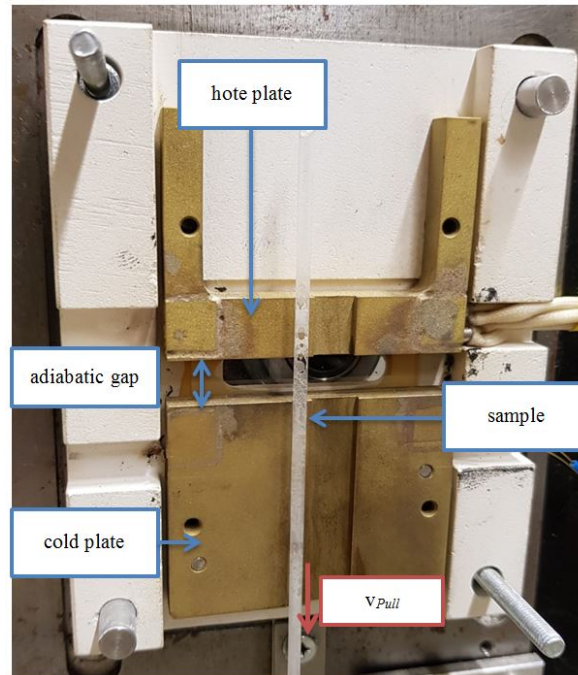
Fig. 31: Bridgeman furnace with the filled sample adjusted within the Bridgman furnace.

3.5 Experimental Procedure

All samples, presented in Table 5, were mixed with 0.01 ± 0.01 g hollow glass spheres with a diameter of 10 µm and a size distribution of 2–20 µm according to Table 4. In order to ensure uniform starting conditions with respect to the concentration distribution within the samples, all of them were homogenized before the solidification procedure. This was achieved by quickly moving the sample through the hot and cold zones over the whole sample length.

To achieve an equilibrium state, the sample was heat up to operating temperature and was kept unmoved for one hour. After this, the sample was moved downwards from the melting zone to the cooling zone with constant pulling velocity (v_{Pull}). Due to this movement, the solid/liquid interface showed – depending on the chosen concentration and pulling velocity –

different solidification morphologies. Table 5 shows the process conditions for the solidification experiments.

Table 5: Data with all the values of the testing series.

Concentration	v_{Pull}	G/v	T_{hot}	T_{cold}
[mol]	[μm/s]	[K s/m]	[K]	[K]
0.48	0.122	$4.59 \cdot 10^{10}$	426.1	358.1
	0.140	$4.01 \cdot 10^{10}$		
	0.157	$3.57 \cdot 10^{10}$		
	0.174	$3.21 \cdot 10^{10}$		
	0.192	$2.92 \cdot 10^{10}$		
	0.209	$2.68 \cdot 10^{10}$		
0.50	0.122	$4.59 \cdot 10^{10}$	426.1	358.1
	0.140	$4.01 \cdot 10^{10}$		
	0.157	$3.57 \cdot 10^{10}$		
	0.174	$3.21 \cdot 10^{10}$		
	0.192	$2.92 \cdot 10^{10}$		
	0.209	$2.68 \cdot 10^{10}$		
0.52	0.122	$4.59 \cdot 10^{10}$	426.1	358.1
	0.140	$4.01 \cdot 10^{10}$		
	0.157	$3.57 \cdot 10^{10}$		
	0.174	$3.21 \cdot 10^{10}$		
	0.192	$2.92 \cdot 10^{10}$		
	0.209	$2.68 \cdot 10^{10}$		
0.54	0.122	$4.59 \cdot 10^{10}$	426.1	358.1
	0.140	$4.01 \cdot 10^{10}$		
	0.157	$3.57 \cdot 10^{10}$		
	0.174	$3.21 \cdot 10^{10}$		
	0.192	$2.92 \cdot 10^{10}$		
	0.209	$2.68 \cdot 10^{10}$		

4. Experimental results

This chapter includes the obtained results of the solidification experiments. For the investigation of the convection several particles which was well recognizable was selected and the behaviour of the particles was investigated. After this, the obtained flow patterns are presented. Here, focus was laid on investigations of convection during the formation of layered structures. Finally the flow of these structures was compared with a planar solidification front with only one existing phase. It has to be noted that an in-situ observation of a solidification experiment is very difficult to explain by showing a picture sequence. Here, only the most meaningful images of the experiments are presented to show the evolution of the morphologies.

4.1 Sample in Rest

Since the densities of the HGS particles $(\rho_{seeding} = 1.1$ g/cm^3) and the liquid $(\rho_{melt} = 1.036$ g/cm^3) are slightly different, an analysis of the behavior of the tracers within the liquid organic alloy was performed. For this, a sample with a concentration of $x = 0.54$ mol fraction NPG was kept immobile for several hours within the furnace. Thus, the behavior of the particles within the liquid can be checked.

HGS: $x = 0.54$, $v = 0$ µm/s

According to the experimental procedure the sample remain stationary for 1 h in the temperature gradient to reach a thermal equilibrium state. Afterwards, the sample remains stationary to detect the movement of the particles within the melt ($t = 27030$ s).

During this time, the particles followed the gravitational force and move almost straight downwards towards the boundary surface, where they accumulate and remain unmoved (black pointed layer on the s/l interface), see Fig. 32. According to the density difference between the tracers and the organic component, this movement was expected. The motion of one individual tracer ahead of the s/l interface is evaluated by arrows which represents the change of the position. In contrast to the moved samples, here, each individual particle-movement has a certain color.

In addition, unexpected temporary local upward movements were observed, presented in Fig. 32b, marked with yellow arrows. It can be seen that there are particles which moves upwards from the s/l interface into the molten area. This is due to some liquid channels, which are described later on in detail, in chapters 5.2 and 6.

The upward movement of these particles from the liquid channels (yellow arrows) obviously has an effect to its surrounding. It causes particles which are directly besides these particles to be pulled upwards with this flow (blue arrows).

(a)   (b)
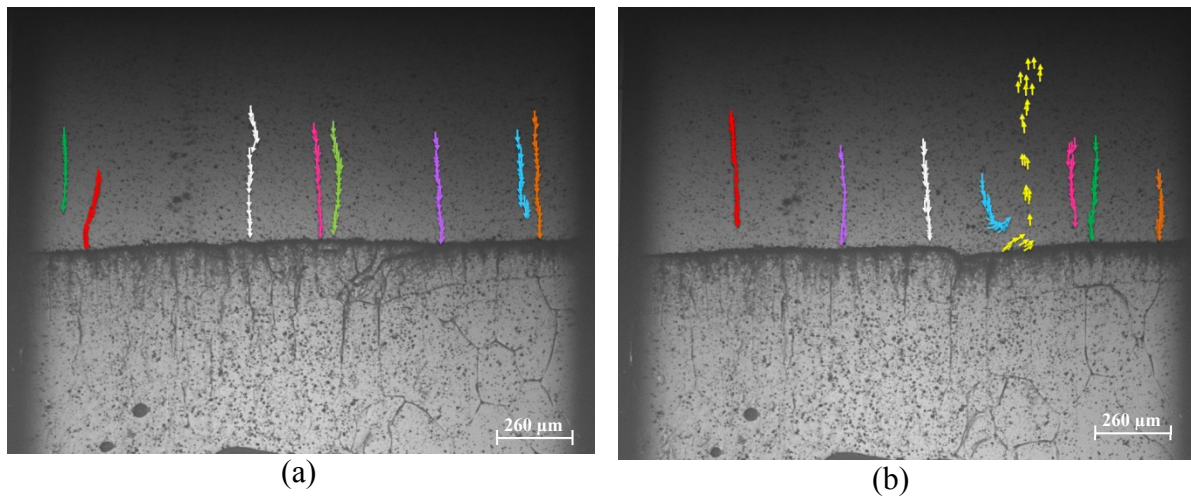
Fig. 32: Illustration of the particle motion in an unmoved sample (v_{Pull} = 0 µm/s). The movement was made visible with coloured arrows. Each different colour represents one individual tracer moving line and each arrow a time step of Δt = 30 s. (a) within a time frame of t = 810 s until t = 1610 s only a downwards movement was observed. (b) at a time frame from t = 1650 s to t = 2460 s also an upwards movement was found (yellow).

4.2 Solidification Experiments

In the following three representative solidification experiments are selected and subsequently evaluated. The first experiment shows the evolution of a planar s/l interface. It serves for comparison with the experiments where layered structures occur. Those structures are presented below. All samples were first moved upwards and downwards over the whole sample length to achieve homogenization. The pulling velocity hereby was $v_{Pull} = 15.64$ μm/s, which is compared to the velocity of the solidification experiments 100 times faster. Due to this movement, which leads to dendritic structures, an inter-dendritic liquid still exists even after homogenization within the sample. This is evident on elongated fluid channels and droplets within the mushy zone. After that the samples were held in "start position", for 1 hour, to receive a planar solid/liquid interface. Finally, the sample was moved with a defined constant pulling velocity for approx. 8 hours through the Bridgman-furnace. The dynamic of the solid/liquid interface morphology was documented with the DIoS system which takes a picture every 30 seconds.

Planar s/l interface: $x = 0.50$, $v = 0.140$ μm/s

During the direct solidification experiment the organic substances showed initially planar solidification morphology. Fig. 33 shows representative snapshots of the experiment for $x = 0.50$ and a pulling velocity of $v = 0.140$ μm/s. The sequence shows a timeframe from $t = 12000$ s until $t = 34650$ s. On both sides of the sample, the interface is slightly curved. With increasing time, this curvature increases from approx. 35° (a) to approx. 43° (d). However, this is a result of the concentration distribution ahead of the solid/liquid interface, described in [17]. Also, an impurity was found at the interface (a–c). However, this does not affect the evolution of the morphology. The detected flow pattern is then given in Fig. 34. Here the flow pattern is marked with red arrows in contrast to the layered structures.
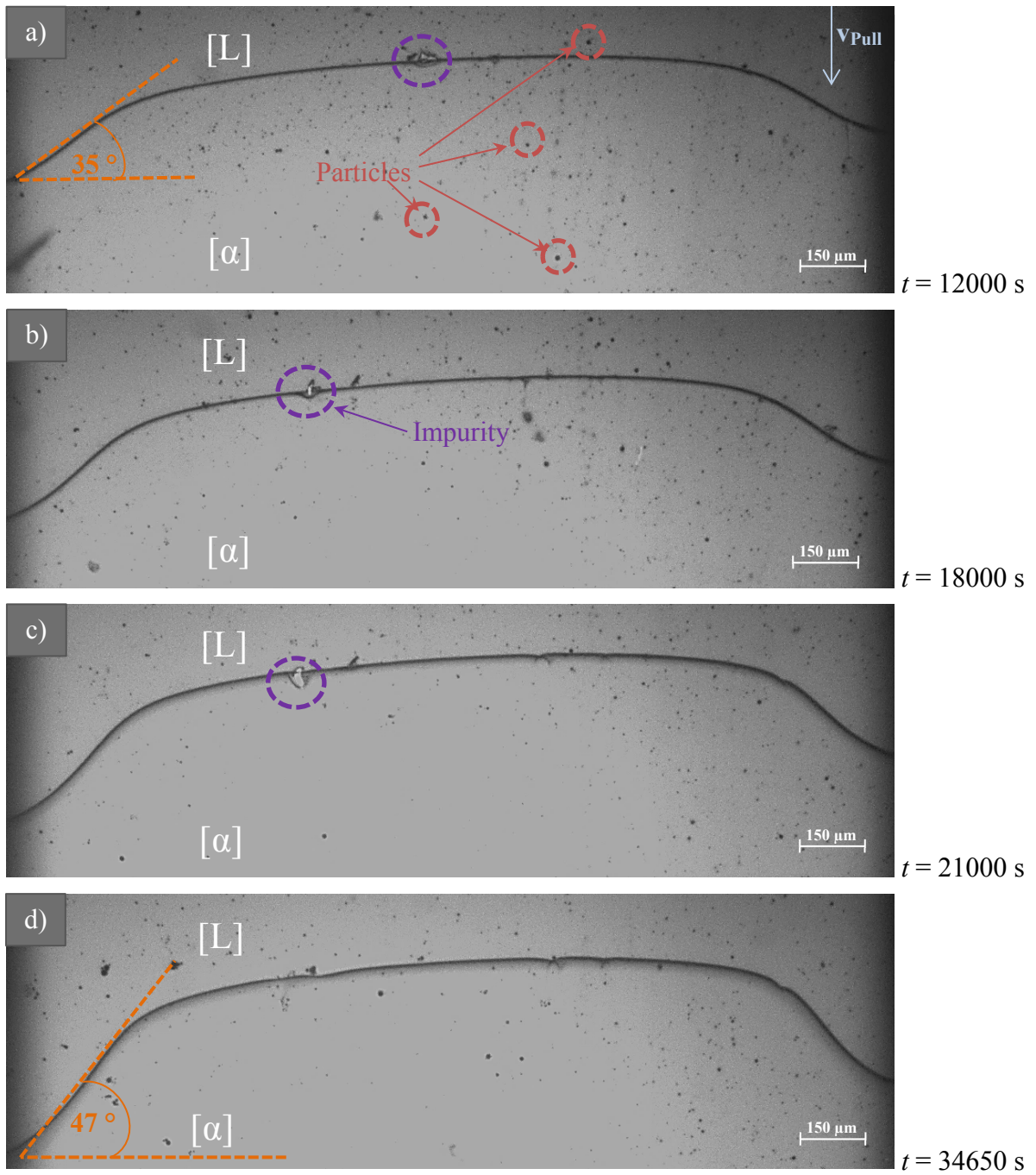
Fig. 33: Evolution of a planar interface with curved sides near the sample wall.
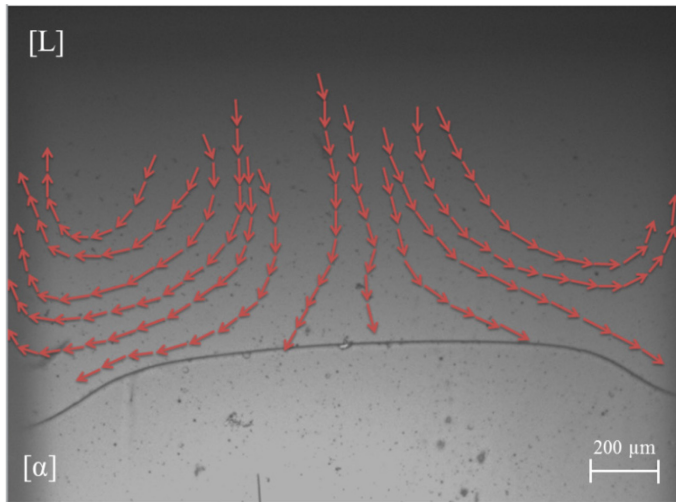
_t = 8550 – 9000 s_

Right after beginning of the experiment a curvature developed on the s/l interface on the left and right side of the sample. The reason is described in chapter 5.3.

The particles moved from the center of the sample to the left and right downwards and just before the interface, they moved upwards with the flow back up along the glass wall (vortex).
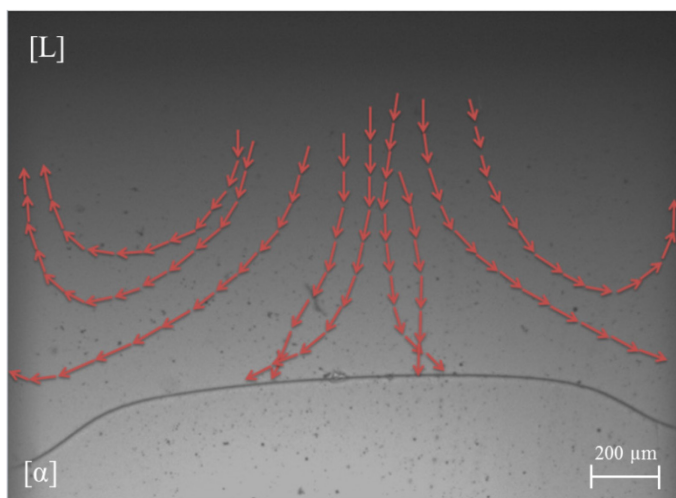
_t = 11550 – 12000 s_

During this time interval, there was no significant change in flow direction. Particles which are situated in the middle of the sample falls straight downwards and particles on the left and right side of the sample moves upwards along the sample wall and ahead of the curvature.
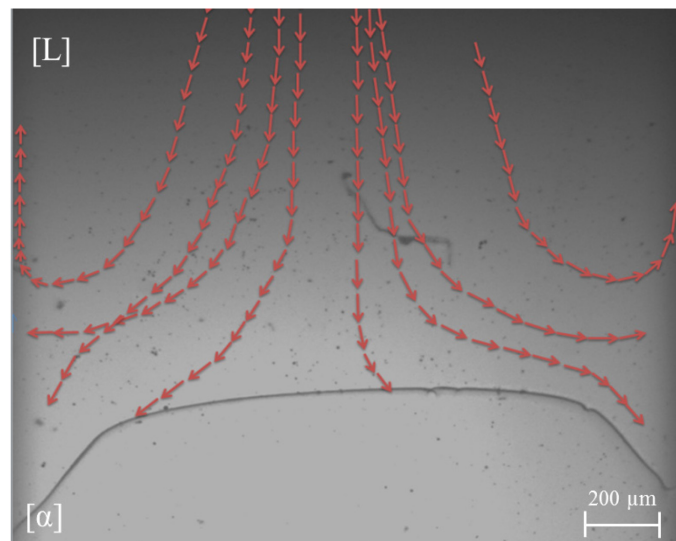
_t = 34050 – 34650 s_

Towards the end of the experiment, the curvature of the s/l interface increased from initially 35° to approx. 47°, see Fig. 33. It was observed that individual particles followed the bending. However, most of the particles followed the undisturbed flow near the center of the sample or rather in front of the s / l interface, respectively

Fig. 34: Evolution of the flow pattern for experiment *x* = 0.50, *v* =0.140 μm/s.

<u>Layered structure: $x = 0.52$, $v = 0.174$ µm/s</u>

Fig. 35 shows the experiment for layered solidification morphology of an alloy with $x = 0.52$ mol fraction NPG and a pulling velocity of $v = 0.174$ µm/s. The formation of layered structures in form of bands and peritectic coupled growth in combination with the visualization of the flow through tracers is shown in Fig. 36. The various phases and bands will be discussed below.
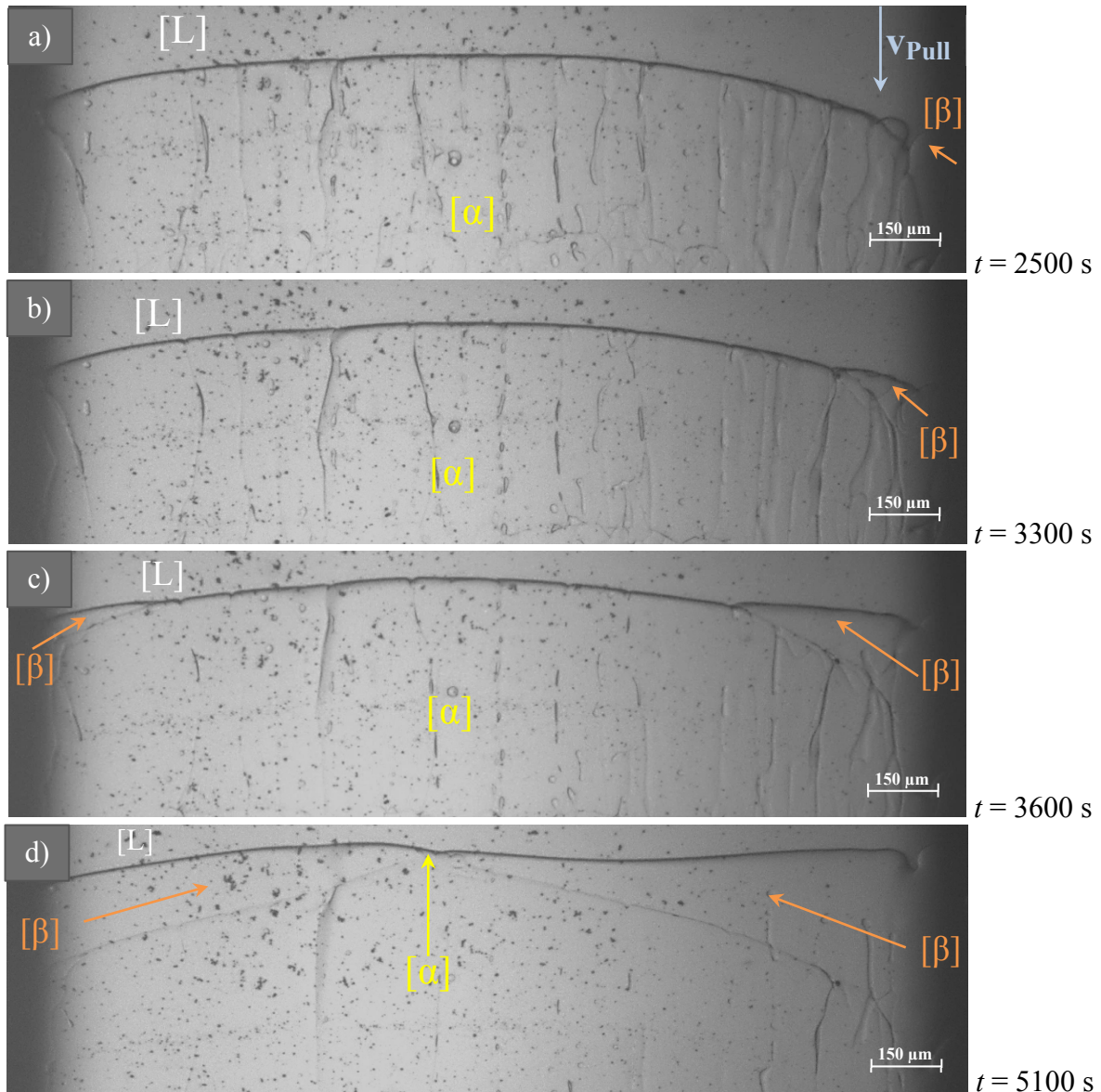
Fig. 35: Layered structures for solidification experiment: $x = 0.52$ mol fraction NPG, $v = 0.174$ µm/s.

The developing microstructure, given in Fig. 35 illustrates the following characteristics: Initially, after $t = 2.500$ s the formation of layered structures begins with the growth of a β-

band on the right side of the sample wall in lateral direction towards the centre of the sample, see picture a–d.

After $t = 3600$ s – which corresponds to picture b – it can be seen, that also from the left side a β-band begins to grow lateral towards the centre of the sample. At picture d, the two bands seems to be grown together. In fact, a small part of α-phase breaks through both island bands. The growth of these two β-bands lasts approx. $t = 2600 \pm 450$ s (variation is due to the reason that it is not visible where or rather when the nucleation of β starts exactly). Measured near the s/l interface, the left β-band has a final length of approx. 870 µm and the right β-band of approx. 1064 µm (lateral direction).

Fig. 36 illustrates the growth of the second phase which leads to two parts of island growth separated by a small part of the α-phase. For clarification the pictures are combined with a sketch.
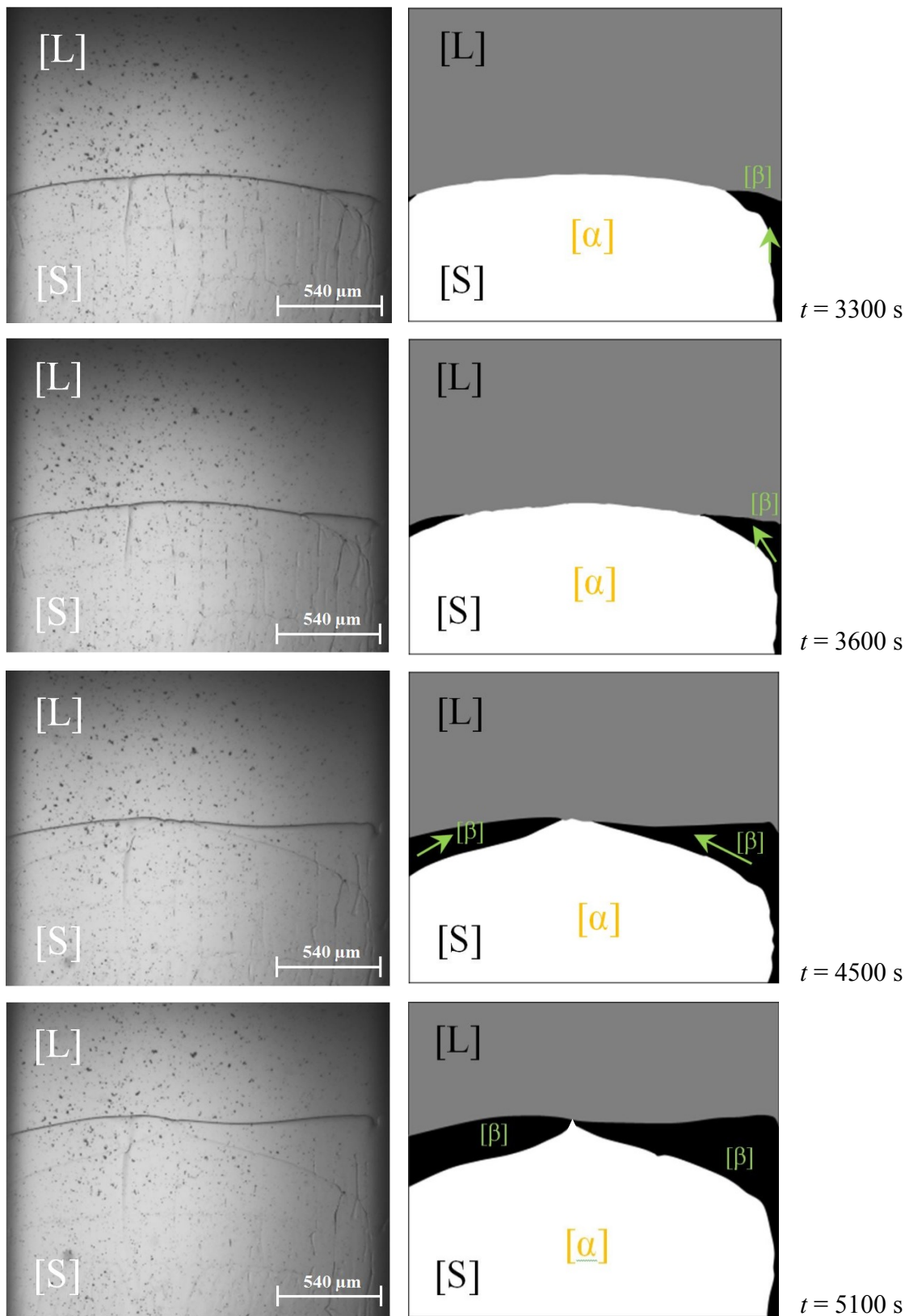
Fig. 36: Presentation of the banding cycle from $t = 3300 – t = 5100$ seconds.

The dynamic of the s/l interface and the competitive growth of both phases, which turn the banded structure finally into peritectic growth, is shown in Fig. 37a–d for a period of $t = 5700$ s $- t = 10500$ s. After the island bands try to reach each the middle of the sample, now, the α-phase is the preferred phase and starts to grow again, white area in the sketch, see Fig. 37a.

It spreads out in both lateral directions which can be recognized in the growing triangle a–d. The lateral length of this triangle at the s/l interface is approx. 568μm (measured on picture c). Simultaneously, there is another α-band forming on the right side of the sample above the β-phase (b–c) which grows also lateral in the middle of the sample. This multiple nucleation on the s/l interface finally leads to peritectic coupled, see Fig. 37d. However, the transition from banding cycle to PCG was observed within a time frame of 5400 ± 90 s.
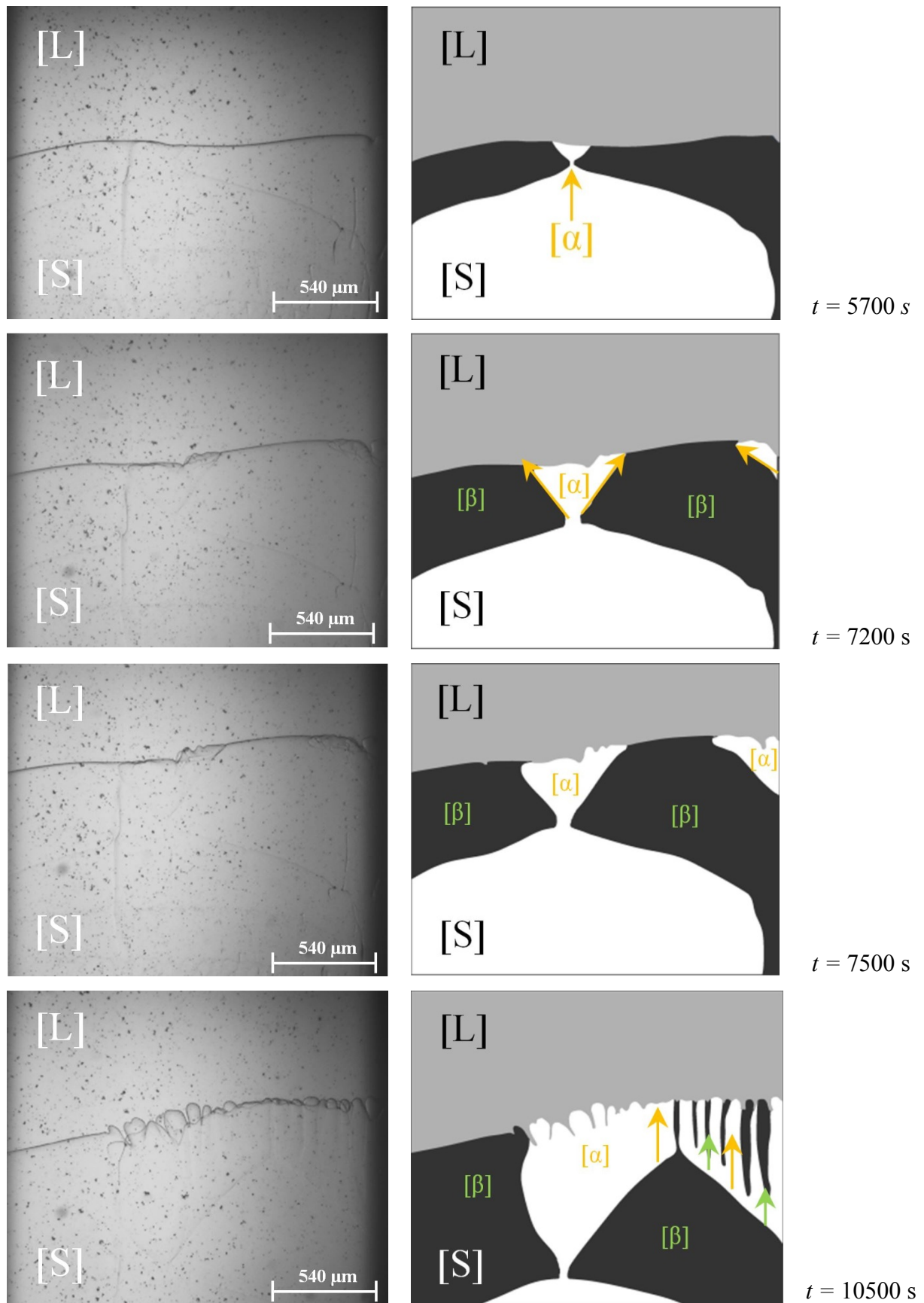
Fig. 37: Transition from banded structure to PCG. After the two island bands where grown to reach the middle of the sample the α-phase starts to grow again (*t* = 5700 s). Also another α-band starts to grow on the right side (*t* = 7200 s). The sequence ends after *t* = 10500 s with the evolution of PCG.

For the evaluation of the convection in front of the s/l interface a data folder was created for each picture according to the explained evaluation method in chapter 4.

Fig. 38 shows the arrangement. A few selected, well recognizable particles were selected, traced and marked with an arrow which has a certain colour, so it is ensured, that even later on each particle can still be followed, Fig. 38a.

That means that each particle can be assigned to a given time. It was attempted to obtain particles from each section of the sample (left side, middle and right side) Fig. 38b. After a period of time, all arrows were overlaid to represent the behaviour of the flow after a specific time Fig. 38c.
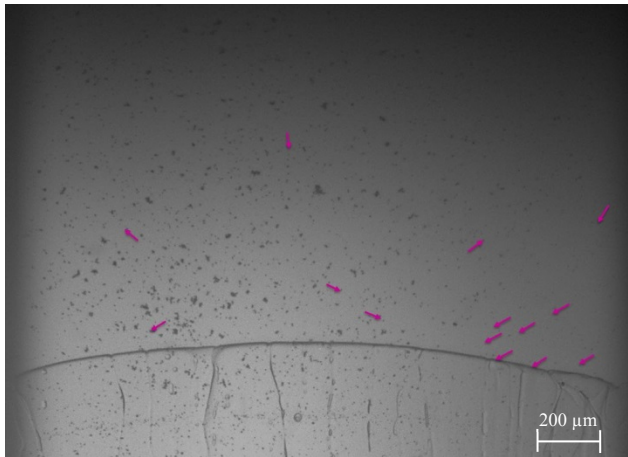
(a) Picture of the map after t = 3120 s. It shows the arrows of each selected particle with the characteristic colour.
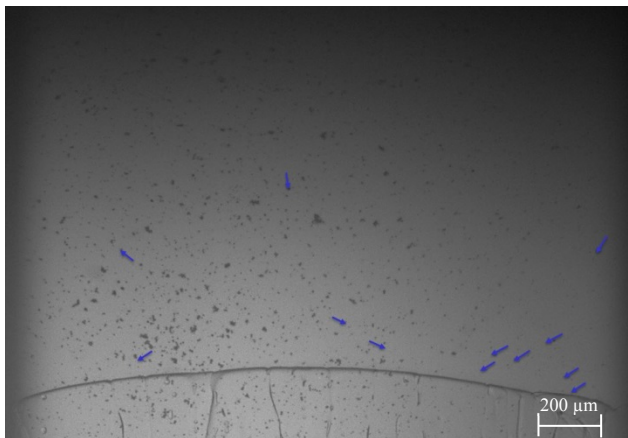
(b) Picture 30 s later. It was tried to follow particles of each area of the sample.
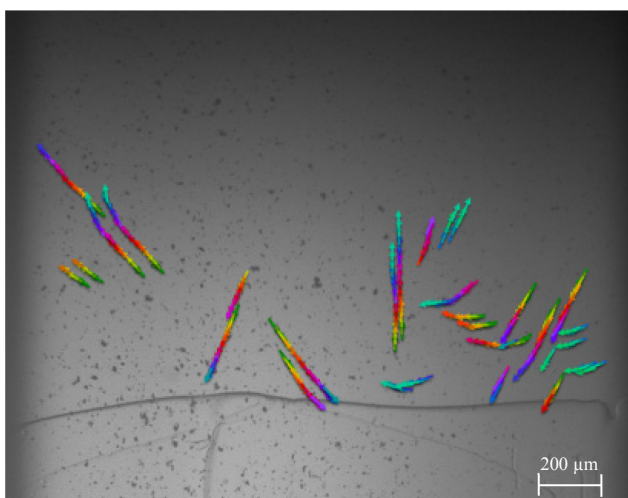
(c) Last picture of the map– overlay of all arrow. It shows the behaviour of the flow after a specific time period.

Fig. 38: Evaluation method for experiment HGS x = 0.52 mol fraction NPG

Fig. 39 shows the whole implementation of the flow analysis of this experiment. The evaluation of the flow starts at t = 0 s. Initial the boundary layer was slightly curved on the right side of the sample. The evaluation ends with the formation of α-phase between the two β-island bands at t = 4620 s.
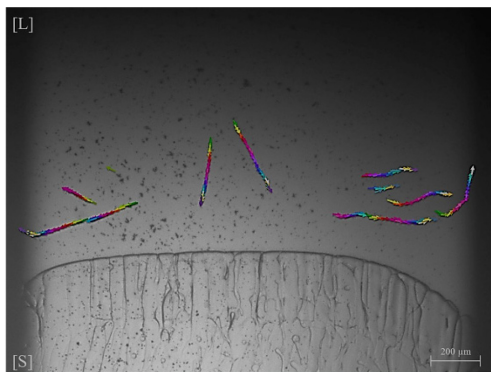
t = 0 – 900 s

Initially, a flow is formed, which bends to the left and right side of the sample sample wall. In the middle of the sample the particles falls fairly straight downwards. The average velocity of the particles was approx. $v_{particle}$ = 0.596 µm/s.
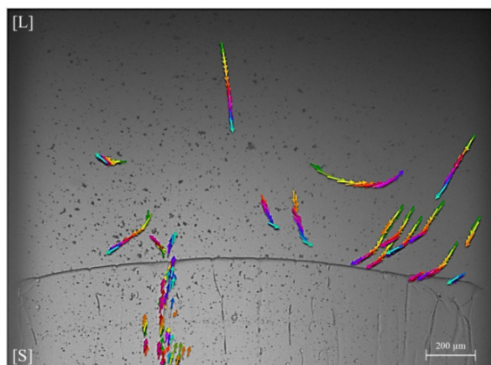
t = 2760 – 3360 s

There were lot of particles on the right side of the sample which are moving inclined with respect to the interface normal. On the left side of the sample only a few particles were recognized. This is probably because there was a strong flow out of a liquid channel which displaces any flow in the surrounding.
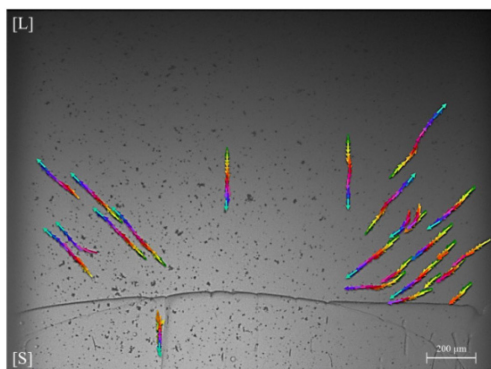
t = 3390 – 3990 s

On the left, the particles from the liquid channel seem to adapt to the flow in the upper surrounding liquid material and are transported upwards. On the right side the movement adapted to the development of the band which can be seen in the increased bending of the arrows.
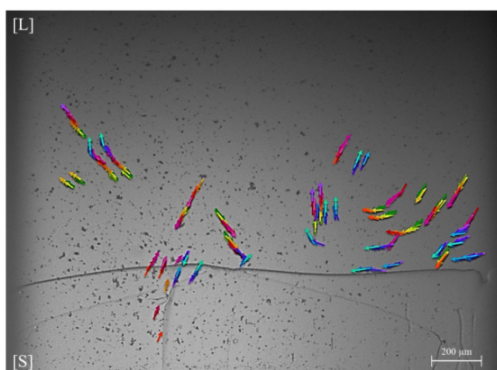
t = 4020 – 4620 s

Again a strong movement from the right side to the left side is shown. All in all is is a very diffusive movement. The liquid channel was still present although the β-band was growing "over" this channel.

Fig. 39: Evaluation of the flow pattern ahead of the s/l interface.

Liquid channels

Since there is repeatedly an upward movement observed within the liquid material, attention was paid more closely to this. Due to the fact that this movement is assumed to come from liquid channels, situated within the mushy zone, which came from interdendritic liquid, one particular particle within the biggest liquid channel was traced. Fig. 40 shows the movement of this particular particle within a time frame of $t = 4020$ s to $t = 4470$ s. It first moves upwards (yellow arrows) and after 4140 seconds it moves downwards within a frame of 30 seconds (red arrow). After these 30 seconds it moves upwards again until it reaches the s/l interface.

This movement was observed with several particles within this range. It looks like as if the particle is transported laterally upwards with the progressing band which grows from the left side to the center of the sample. Finally, after t = 4290 seconds it reached the s/l interface, where it moved upwards into the liquid. At the grain boundaries, however, a correspondingly high number of particles were recognizable.

As already mentioned, in contrast to particles in the liquid region, the particles here had a non-constant velocity which reached from approx. $v = 0.894 - 1.49$ µm/s. Assuming the average velocity of the up going particles with 1.19µm/s this is two times higher compared to the velocity of all other down going particles within the sample.
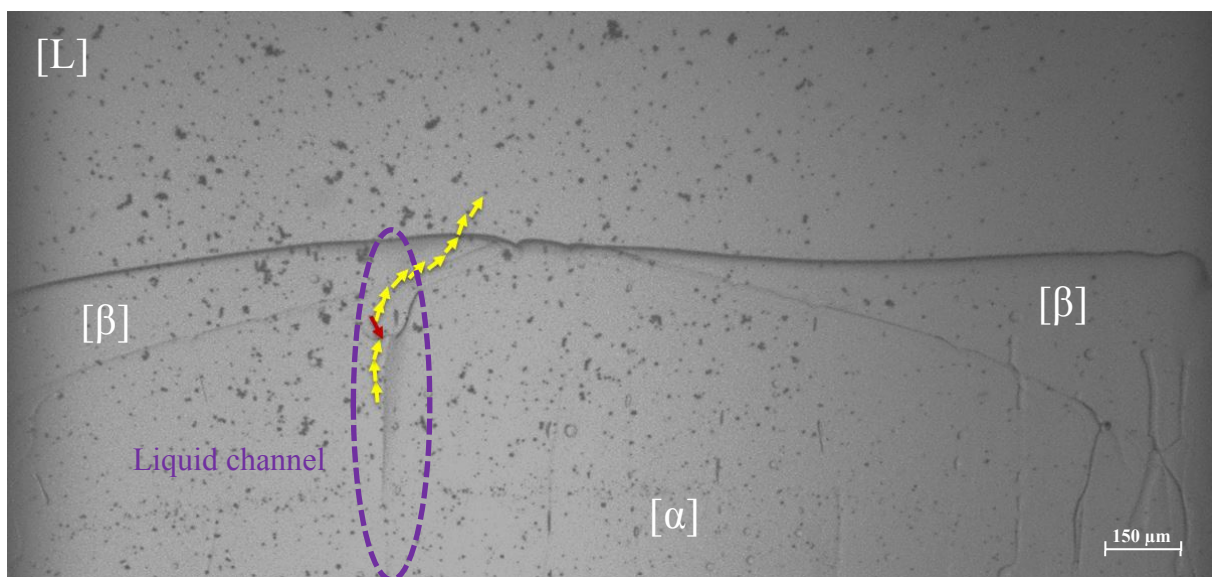
Fig. 40: Path of a Particle within a liquid channel, upwards movement is marked with yellow arrows and downwards movement with red arrows.

In some cases liquid micro-plumes with enclosed particles were observed to merge together and thus form an elongated channel which can reach up to the top of the s/l interface. Here, the particles leak out of the solidified material into the liquid material and move upwards with a higher velocity than all the other particles in the liquid. This phenomenon was observed during the whole experiment. Thus, it can be assumed that all particles, which were recognized to move upwards in the liquid area, probably come out from these channels or from the vortex of the flow.

Carefully observation of the small channel ($x = 0.52$, $v = 0.174$ μm/s) revealed also an oscillatory motion in the lateral direction. It moves alternately right and left back and forth. Fig. 41a shows a picture of the observed oscillating liquid channel within this sample and Fig. **41** b–c show sketches of the channels (for better understanding).

(a) (b) (c)
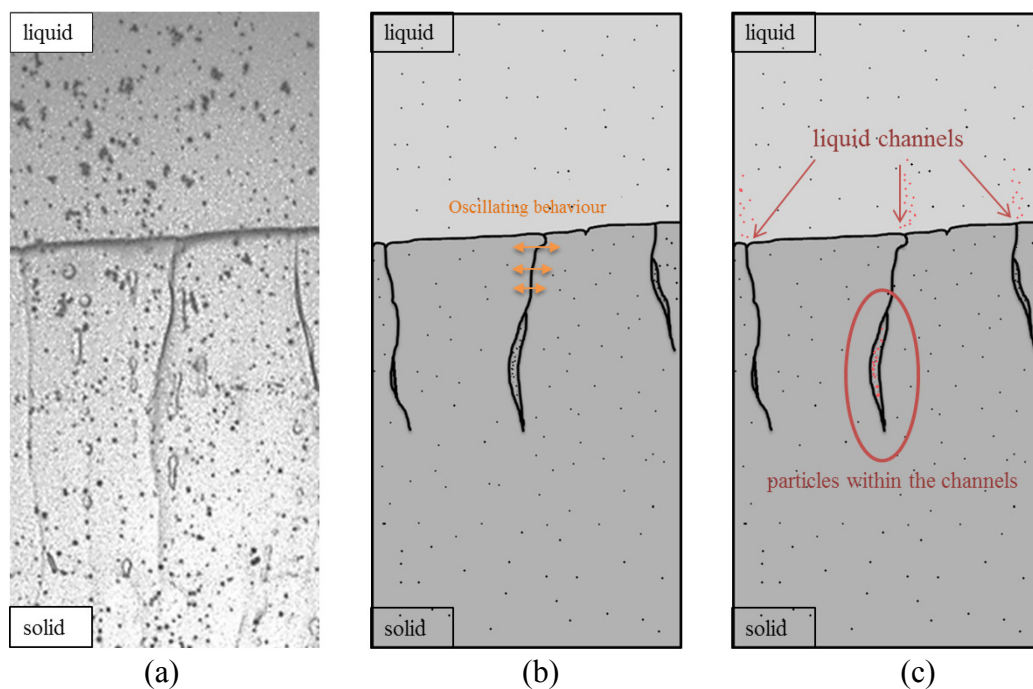
Fig. 41: Liquid channels within the solidified area including enclosed particles: a) real picture of the experiment (b) sketch of the observed channel with oscillating behaviour in lateral direction and (c) sketch of the whole channels including the enclosed particles which are rising upwards out into the liquid (red colour).

Layered structures, $x = 0.52$ mol fraction NPG, $v = 0.157$ µm/s

The second layered structure experiment was found for $x = 0.52$ mol fraction NPG. Pictures of the whole banding cycle from $t = 2250$ s until $t = 7350$ s are shown in Fig. 42. After the sample was homogenized and hold in rest for 1 hour, it was pulled with a velocity of $v = 0.157$ µm/s.

Here, the growth of a β-band was only in one lateral direction, from the left hand side to the right hand side, see Fig. 42a–c. The period in which the band grows was approx. $t = 5100$s. Taking the whole size of the sample for growth, that corresponds to a growth velocity of 0.392 µm/s of the band. After the band reached the middle of the sample there was, again, a transition to peritectic coupled growth Fig. 42d. It has to be mentioned, that the β-band nonetheless still grows in the lateral direction. It looks like the band is growing above the alpha phase. (s/s transformation or growth) which would take a very long transition time. However, since the growth rate is nearly that of the previous experiment, it is believed that the band is growing in a different plane of the sample.The length of the band is 2000 µm since it grows from the left side of the sample right up to the edge of the right side of the sample.
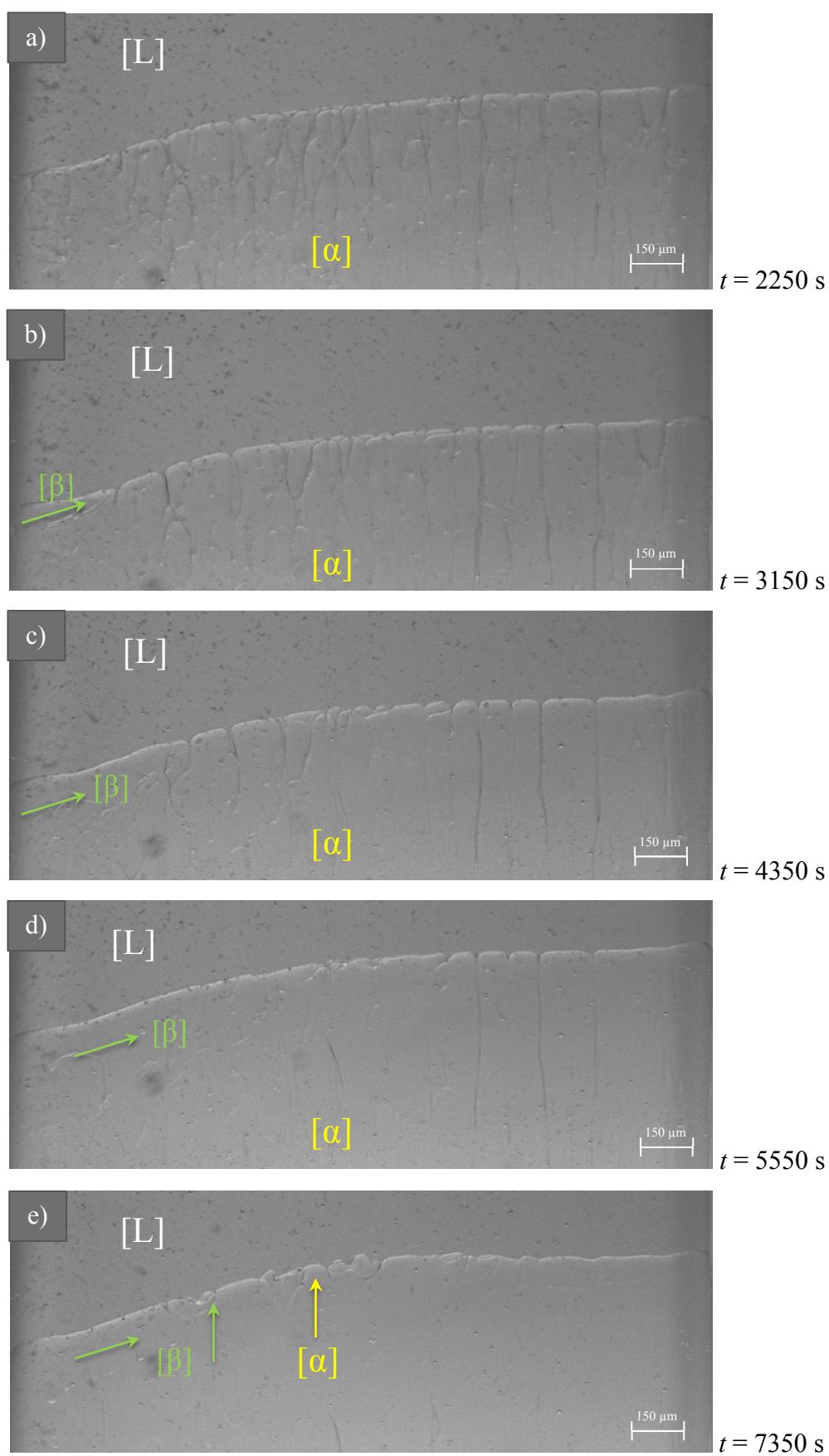
Fig. 42: Evolution of a β-band from left to right (b–e) and transition to coupled growth (c).

Fig. 43 shows details and sketches of the transition from banded structure to peritectic coupled growth. The nucleation of β starts at $t = 2250$ s. The band grows from the left side of the sample in lateral direction into the middle of the sample ($t = 3.350$ s). After $t = 4350$ s, peritectic coupled growth starts. Nevertheless, undisturbed by PCG, the β-band still grows until it reaches the right end of the sample after $t = 7350$ s. Thereafter only PCG was observed.
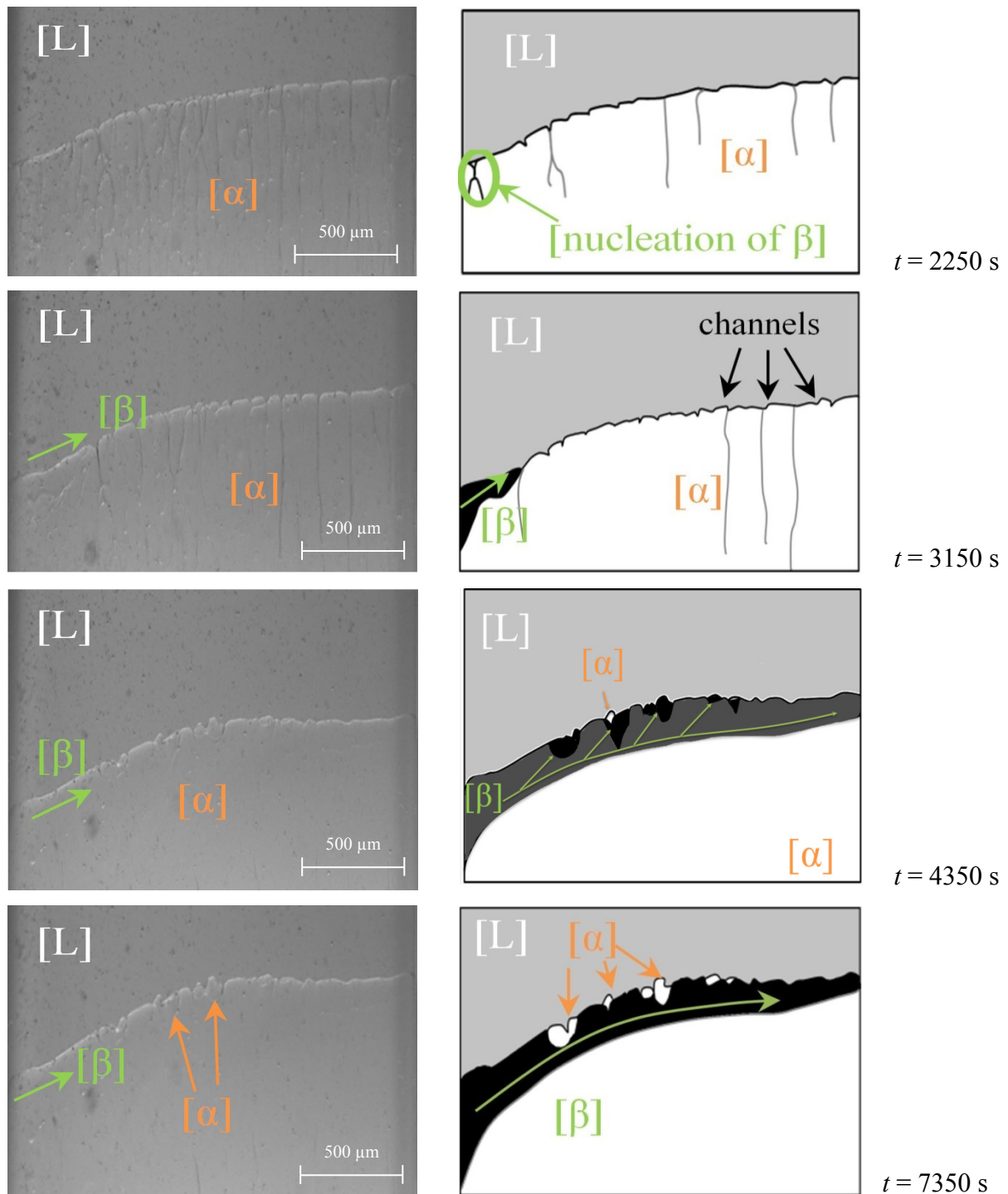
Fig. 43: Nucleation, formation of banded structure and transition to PCG of the β-phase.

The evaluation of convection in this sample showed, that the main flow starts from the right side of the sample to the left side. All in all the particle movement was better to evaluate in this experiment since the particles were well distributed in all areas of the sample. Liquid channels were found with flow out of these micro-plumes but it was not observed as obvious as in experiment with $v = 0.174$ µm/s. Fig. 44 shows pictures of the flow pattern within the liquid phase of this experiment for the timeframe $t = 0$ s until $t = 6930$ s.
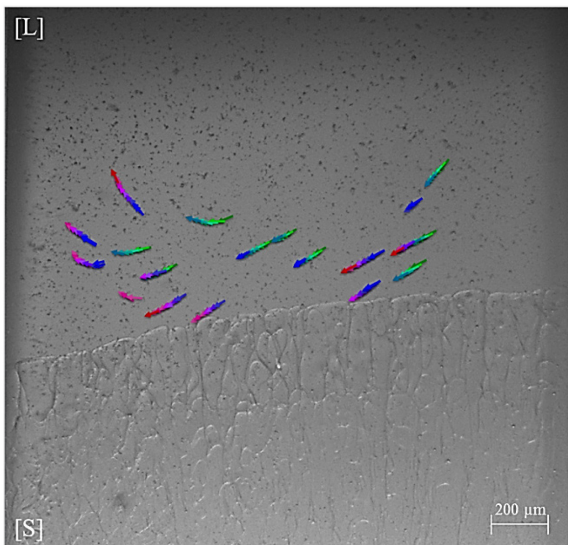
t = 0 – 630 s

The evaluation of the flow pattern starts with the beginning of pulling the sample downwards. After 630 s, the flow pattern shows a movement from the right hand side to the left hand side. The particles were well distributed within the sample and the movement was well visible. The average particle velocity was approx. 0.58 µm/s.
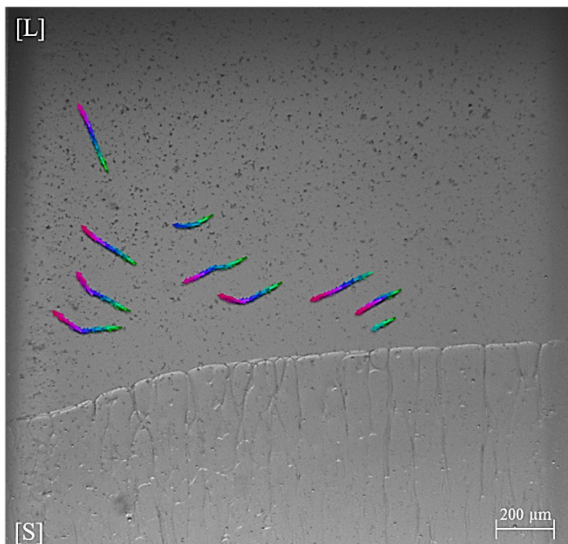
t =1.890 – 2.520 s

Within this time interval, also a movement from right to left was observed. No strongly divergent motions were detected.
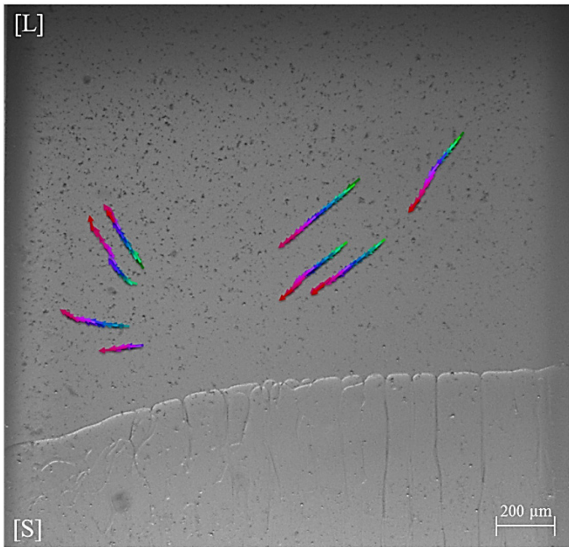
t = 3780 – 4410 s

Although the developing β-band grows from left to right no change in convection direction was observed. Also there was no obvious strong upwards flow from out of liquid channels.
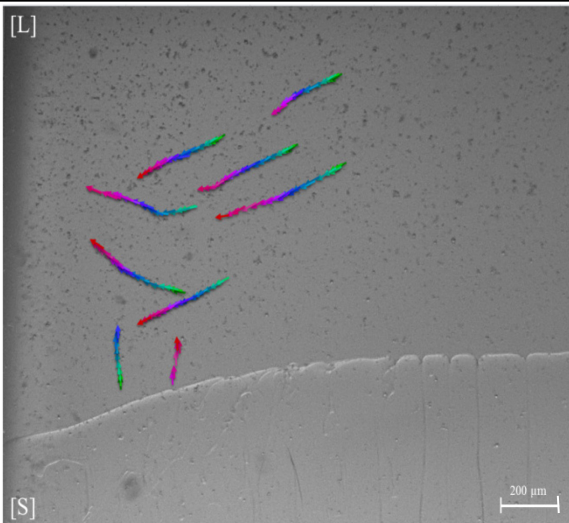
t = 5040 s – 5670 s

There was no significant change in the "main" flow in the middle of the liquid material. Here, particles which move also upwards near the band were observed.
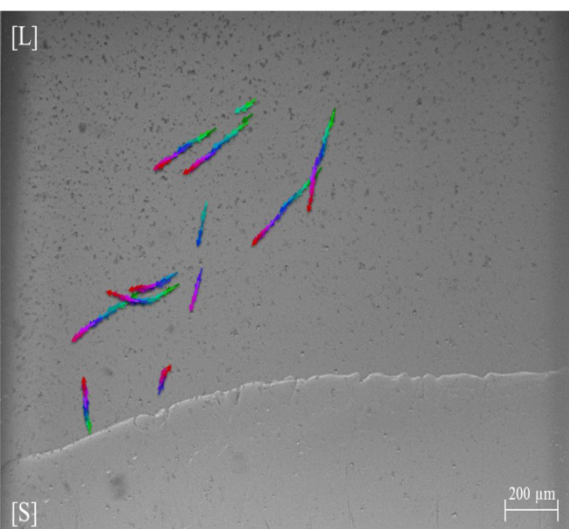
t = 6300 s – 6930 s

The sequence ends at t = 6.930 s. After that there was no important progress for this study. The β-band was grown until the end of the right side of the sample. Additionally PCG was formed. Some liquid channels were found on the left side of the sample, where particles moved upwards. However, the main flow wasn't effected neither by the growth of the band nor the transition of PCG.

Fig. 44: Visualisation of the convection of the period, where banded structure occurs.

5. Discussion

Numerous alloy concentrations covering the whole peritectic range were investigated. For all experiments the temperature gradient was kept constant with $G_T = 5.6$ K/mm and the pulling velocities ranged from $v_p = 0.09$ µm/s to 1.9 µm/s. In this study, layered structures were found for experiments with velocities $v = 0.174$ µm/s and $v = 0.157$ µm/s. Since both phases are transparent, the interpretation of the phases is based by comparing the s/l interface evolution with the published phase diagram [17].

Based on all the experiments within this study, three microstructure maps were created, see Fig. 45. The map was evaluated for (a) $t = 9000$ s, (b) $t = 18000$ s and (c) $t = 27000$ s. They show all observed structures in the area of solidification velocities from $v_p = 0.09$ µm/s to 1.9 µm/s and concentrations from $x = 0.48$ to 0.54 wt. % NPG. That represents almost the entire hypo- and hyper-peritectic area. Here, the microstructure patterns were divided into planar, cells, dendrites, PCG and bands. It can be seen, that with increasing solidification rate a transition from planar to cellular growth to banded structures, as well as PCG and dendritic growth results. Bands were found for concentrations $x = 0.52$ mol fraction NPG and for G_T/v_P values of $3{,}57 \cdot 10^{10}$ and $3{,}21 \cdot 10^{10}$, see Fig. 45a. After that, the bands transform into PCG which can be seen in Fig. 45b.
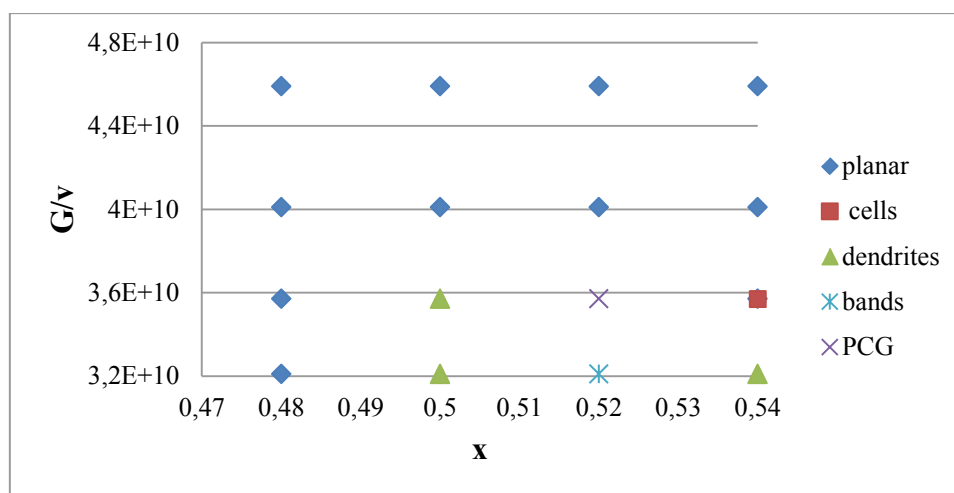
(a)
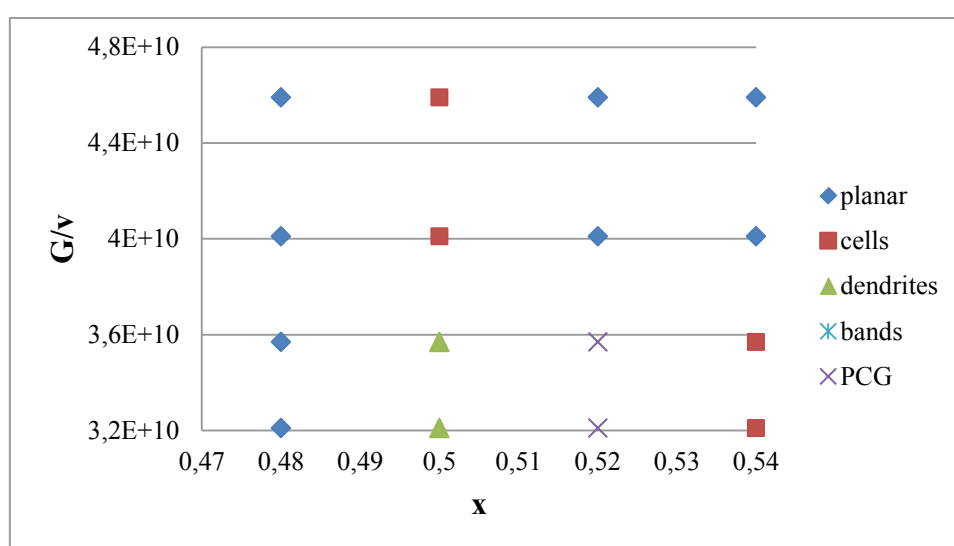
(b)
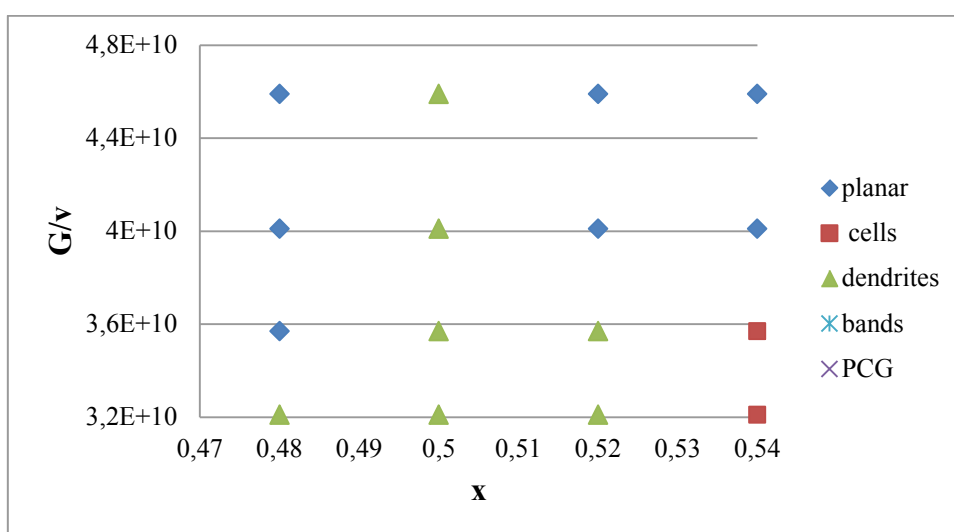
(c)

Fig. 45: Microstructure map after (a) $t = 9000$ s, (b) $t = 18000$ s and (c) $t = 27000$ s.

5.1 Convection for Sample in Rest

<u>HGS x = 54 mol fraction NPG, v = 0 µm/s</u>

Fig. 46 shows two sequences out of the experiment of a sample in rest for (a) t = 3000s and (b) t = 15000 seconds. The concentration redistribution in the mushy zone appears to have no real effect on the flow within the unmoved sample. This can be explained by the fact that the evaluation of the particles showed that they move straight downwards without any change in direction near the interface. Most of the particles remain on the s/l interface except some, which fall into existing liquid channels within the mushy zone, this is visible due to the black lines, see Fig. 46a. These accumulations indicate that for an initial planar front, liquid channels exist which connects even the metastable β-phase with the melt ahead of the s/l interface, see Fig. 46b.

(a)   (b)
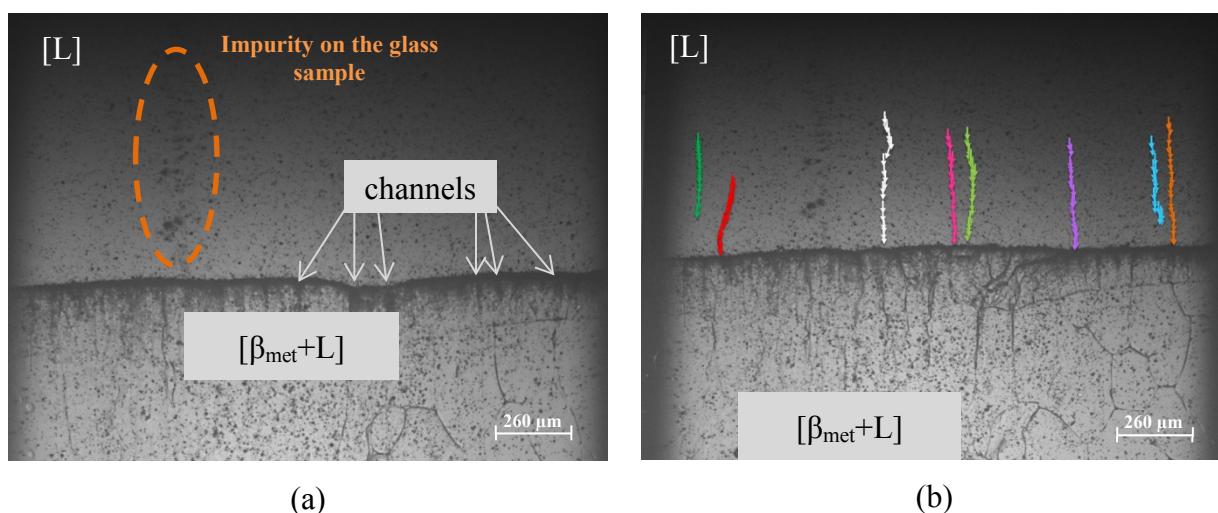
Fig. 46:   Particles within a sample in rest.

Fig. 47 shows the s/l interface according to the phase diagram. The s/l interface corresponds to the phases β_{met} + L. The initial temperature at the interface is T = 410.6 ± 1K, which is the peritectic temperature.
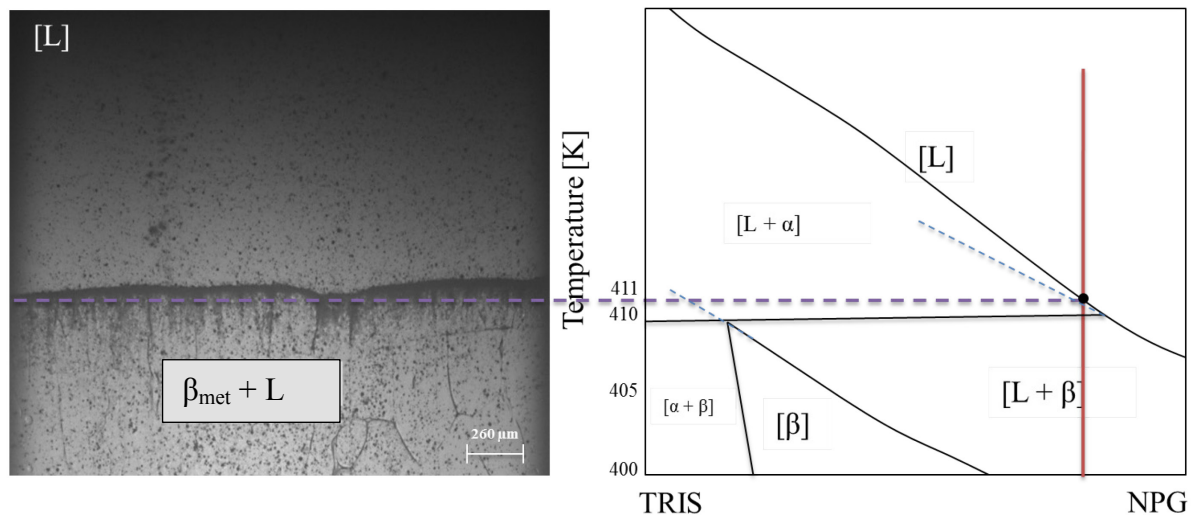
Fig. 47: Observation of the s/l interface with assignment to the phase diagram.

The sinking velocity of the followed particles was estimated. Since the sample was in rest an idealized sinking movement straight downwards was assumed. Any other movements in lateral direction are neglected because they are infinitesimally small. The sinking velocity was calculated according to equation 8. For the calculation, the determined densities of fluid and particle were used. The viscosity as published in [17] was used.

Considering the size distribution of the particles (2–20 µm), the theoretical sinking velocity v_{sink} lies between $v_{sink,min} = 0,01$ µm/s and $v_{sink,max} = 1,28$ µm/s. Table 6 shows the results of the sinking velocity of the particles within the sample in rest. Here, for a certain time frame of each individual particle the distance (s) was measured.

Table 6: Estimation of the sinking velocity of the particles within the steady-sample.

Particle [color]	*s* measured [µm]	*Δt* [s]	*v* [µm/s]
green	275,48	630	0,437
red	257,12	600	0,429
white	449,95	630	0,714
pink	367,31	660	0,557
light green	367,31	810	0,453
violet	367,31	630	0,583
blue	312,21	660	0,473
orange	426,08	660	0,646
average	352,85 ± 67,84	660	0,535 ± 0,11

The average sinking velocity was measured with $v_{sink,average} = 0,535 \pm 0,11$ µm/s. This corresponds to a particle diameter of 12 µm.

Table 6 shows that most of the particles have a slightly different velocity. But due to the fact, that $v_{sink,min} < v_{sink,average} < v_{sink,max}$, show, that the calculated and the estimated sinking velocity are well matching. The different values therefore results from different diameters of the followed particles.

5.2 Liquid Channels

Within the mushy zone the solid phase and the liquid are in equilibrium. Whereby, the mushy zone in these experiments is a consequence of rapid solidification or rather homogenization. This means that even if the planar s/l interface is reached after 1 hour keeping the sample in rest, fine distributed inter-dendritic liquid still exists within the mushy zone. This liquid is enclosed in form of droplets and elongated channels which are constantly moving upwards by the effect of temperature gradient zone melting (TGZM) towards the s/l interface. According to the phase diagram and considering the preliminary Sudan-red tests, mentioned in chapter 2.3, the enclosed liquid is enriched with NPG.

Some liquid channels were detected with free moving particles in contrast to the surrounding solidified area where particles are frozen in. The movement of these tracers is very fast, so it was not possible to evaluate the movement or velocity in detail since the time interval between each pictures is too large. The density of the enclosed liquid is smaller than the density of the melt ($\rho_1 > \rho_2$), therefore, such liquid channels leads to micro-plumes in the melt as soon as they are in contact with the s/l interface. Whereby, during the formation of micro-plumes the liquid channels have to be fed by liquid or squeezed by thermal contraction. The visualized explanation of the two possibilities is presented in Fig. 48. The first possibility is by feeding, see Fig. 48 (a) The NPG-enriched liquid within these channels flows into the melt due to the difference in density. Due to the lighter density of NPG, those particles have a different velocity than particles which are within the liquid material, moving downwards. (b) Due to the assumption that the material acts in all three dimensions, there could also be feeding via other channels and droplets which may be present closed by and be interconnected.

Another possibility is that the liquid channels are squeezed together due to thermal contraction. This means that due to the cooling on the cold plate, the mushy material contracts in lower regions of the sample and this causes squeezing in upper regions of the material, see Fig. 48c.
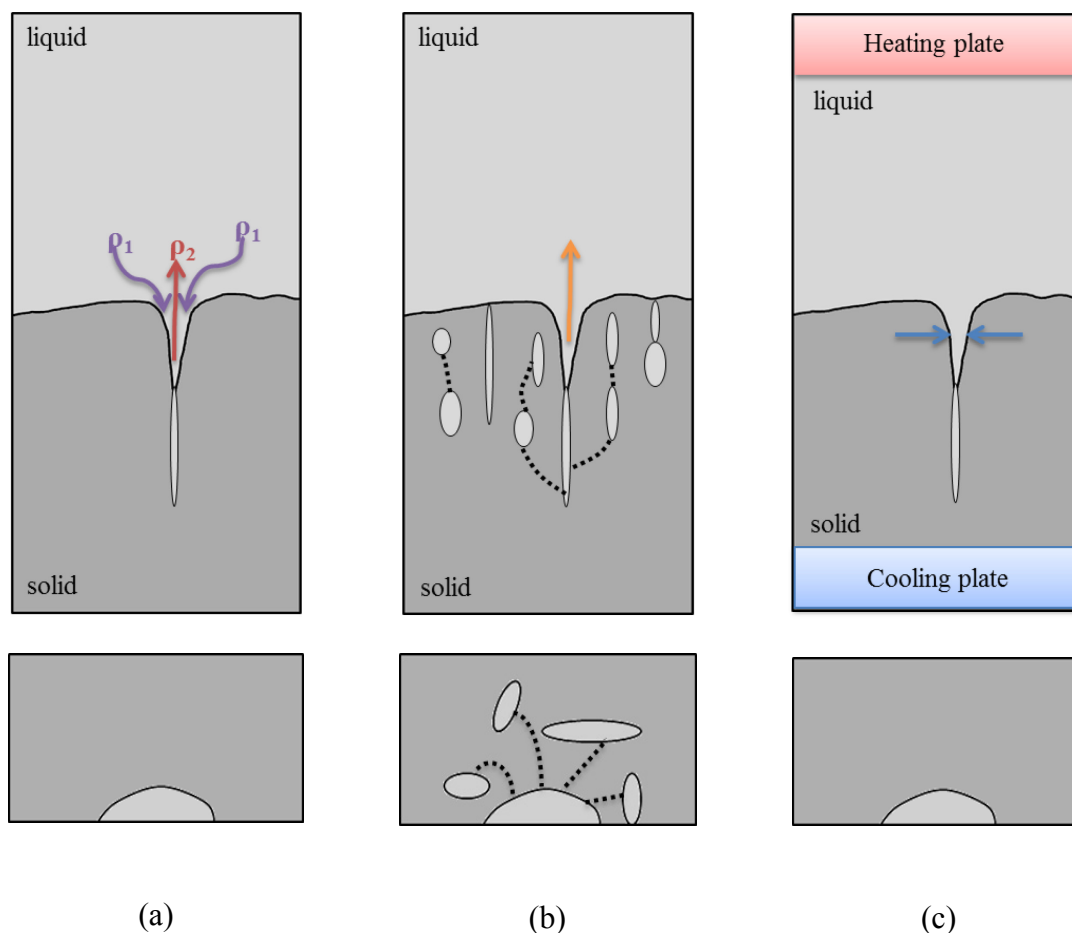

Fig. 48: Assumptions of the evolution of liquid channels (a) $\rho_1 > \rho_2$, (b) connected channels and droplets which can feed other channels (3D effect) and (c) channel is squeezed together due to thermal contraction.

Considering the origin of the liquid channels as former inter-dendritic liquid it is assumed that these micro-plumes are fed by connected channels in the surrounding area. These channels interact with each other. This is caused by the fact that there exists a lot of inter-dendritic liquid material. This behavior may also be the reason for the observed oscillation of the liquid channel in experiment x = 0.52, v = 0.174 µm/s as described in Fig. 41b. Nonetheless, it has to be assumed that all three effects have an impact on the development of micro-plumes.

5.3 Planar structures

Layered structures in form of island bands occur on the assumption that both phases solidify planar. In order to study convection during the formation of layered structures, it was also useful to determine the convection pattern in front of a planar s/l interface for a pure single-phase.

This was done for a concentration $x = 0.5$ mol fraction NPG and $v = 0.140$ µm/s. The movement of the interface is shown in Fig. 49. The values of the temperature were determined by measuring the interface at the center of the sample (blue line) and for the curved interface at the right side of the glass wall (red line).

It can be seen that the initial temperature was $T = 413.5 \pm 1$ K. This corresponds to a planar interface with no curvature. Due to the error indicator this is almost acceptable. With increasing time the temperature of the curved interface at the right side of the sample shows a lower temperature compared to the s/l interface, which is after $t = 200$ s approx. 0.4 K ± 0.5 K and after $t = 1200$ s the difference in temperature is 1.6 ± 0.5 K. Both lines are above the peritectic temperature T_P. This indicates the enrichment of NPG.
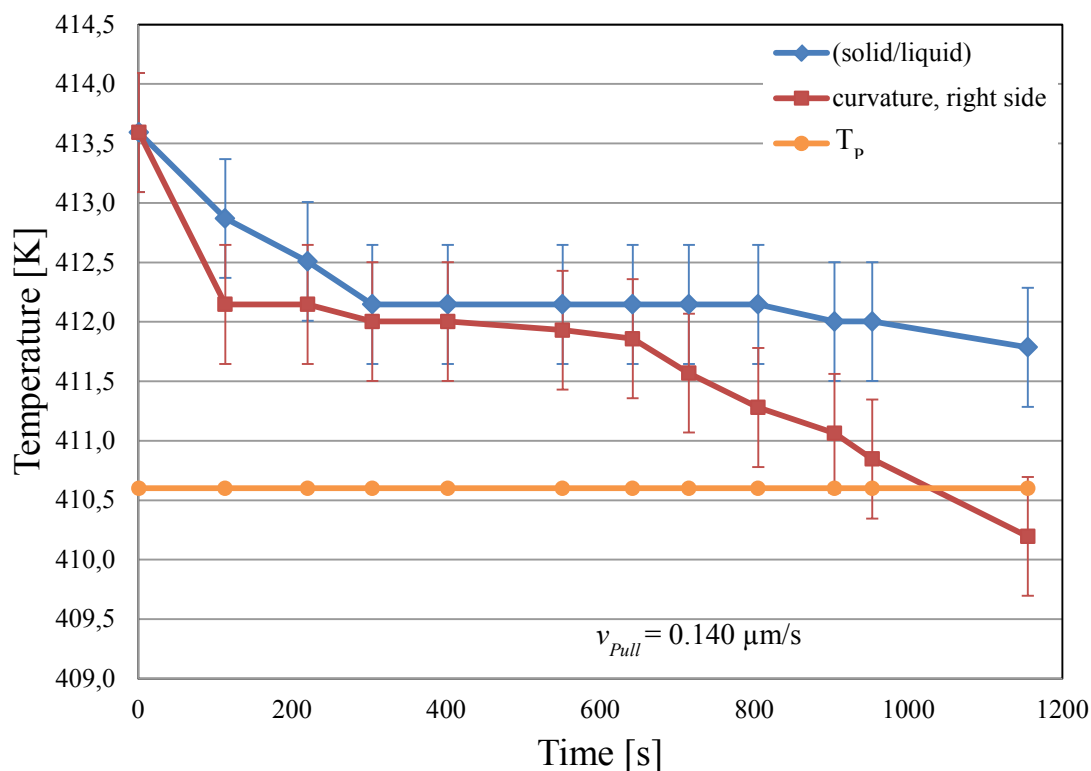
Fig. 49: Time depending interface temperatures for the s/l interface and the curvature at the right side of the sample.

Fig. 50 shows the idealized flow pattern ahead of the s/l interface for a planar interface of just one present solid phase (α-phase). The convection was made visible connecting the position of particles for given time intervals. Each arrow corresponds to a time step of 30 seconds. It was observed that particles at the center of the sample flows straight downwards perpendicular to the s/l interface.
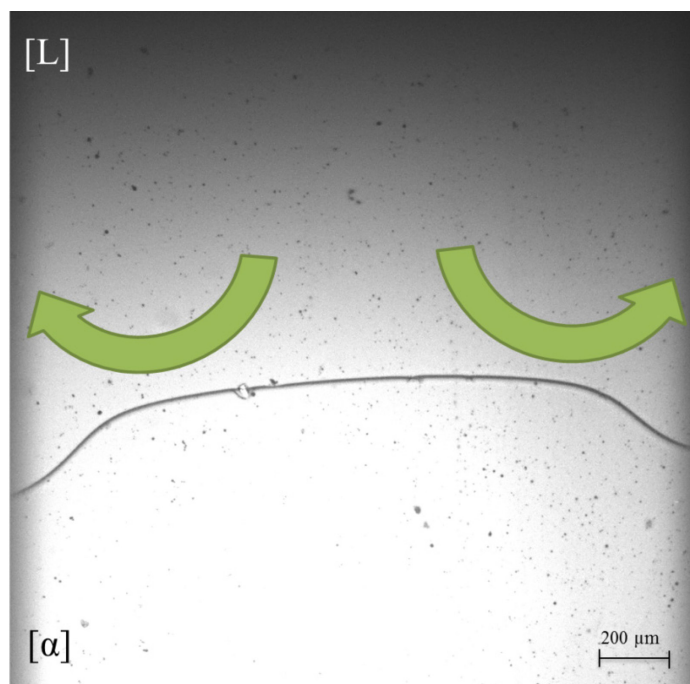
Fig. 50: Idealized representation of the flow within the melt.

The initial fluid concentration corresponds to c_0. On the edge region close to the side glass wall the particles move lateral to the s/l interface.

Initial, the s/l interface was planar but becomes curved during the solidification experiment with increasing time. The s/l interface is indicated by a clear sharp line which suggests that the solidification boundary is not curved against the front and backward glass wall. Additionally, thermo-sensor monitoring exhibited an isothermal temperature distribution rectangular to the glass wall. Therefore, the curved interface must be seen as a consequence of dissimilar concentration distribution ahead of the solidification front.

An explanation for this phenomenon is given by the flow which takes place when the initial concentration c_0 enriched on NPG in front of the interface. Since the partial heavier fluid is moved downward an equal volume of lighter fluid has to be flown upwards.

The expected shape of the flow pattern is described by the Atwood number. It is the difference in the fluid densities divided by their sum. For Atwood number close to 0, the flow pattern take the form of symmetric "fingers" plumes; otherwise, for Atwood number close to 1, the much lighter fluid "below" the heavier fluid takes the form of larger bubble-like

plumes, like in our case, close to the glass walls. As a consequence the region enriches on NPG close to the side wall and the concentration in the center enriches on TRIS. This effect leads to a curved s/l interface.

5.4 Layered structures

In this study, layered structures and the corresponding flow fields for samples with $x = 0.52$ mol fraction NPG are described. Principally it is not possible to optically distinguish between the primary α-phase and the β-phase. The following requirements according to the phase diagram help to indirectly identify the growing phase:

Banded growth leads to an oscillating planar s/l interface due to the difference in the liquidus temperatures of the α- and β-phase. The s/l interface of the primary α-phase prefers to grow at the β-solidus temperature which is at a lower temperature compared to the one of α. The movement is in pulling direction, therefore, the lateral solidification velocity of the solid/liquid interface increases. The opposite applies for the peritectic β-phase which is undercooled in respect to the primary phase α. As soon as the peritectic phase starts to solidify it prefers to grow at the solidus temperature of the α-phase which is at higher temperature. Thus, the solid/liquid interface grows against the pulling direction and the solidification velocity decreases. Therefore, during banded solidification the growth velocity of the planar solid/liquid interface with respect to the pulling velocity helps to indicate the correct phases. [17]

Layered structure: $x = 0.52$, $v = 0.174$ μm/s

After 1 hour keeping the sample unmoved within the temperature gradient of the Bridgman-furnace, steady-state condition was reached. The s/l interface exhibits planar morphology with a backwards curving close to the glass wall. Hence, the initial concentration within the sample is not uniformly distributed. Additionally, another interface can be detected approx. 200 μm below the s/l interface (violet broken lines), see Fig. 51. It represents the liquidus line of the α-phase and the s/s interface with metastable β. The lines separate the phase region [L + α] and [L + α + β$_{met.}$].
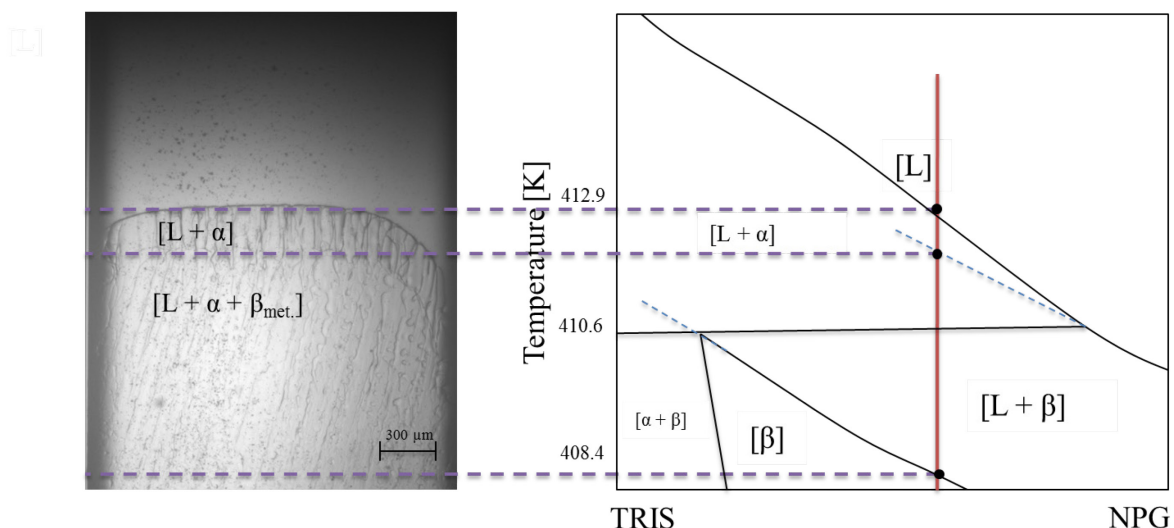
Fig. 51: Observation of the solid and liquid interfaces with assignment to the phase diagram.

The solidification experiment was started by moving the sample from the hot zone of the furnace to the cold zone with a pulling velocity of $v_p = 0.174$ μm/s.

Since the selected pulling rate is close to the constitutional undercooling limit, the s/l interface wants to reach the temperature level of the corresponding solidus line. Therefore, the s/l interface and the solid/solid one shift constantly to lower temperatures, see Fig. 52. As soon as the temperature level of α/l interface is below the temperature of the β-phase, the peritectic phase, becomes the preferred phase. Therefore, the peritectic phase overgrows the primary α-phase in form of two island bands which grow laterally along the initial s/l interface from the side glass walls toward the center.

Fig. 52 shows a sketch of the solidification path for the concentration $x = 0.52$. During the solidification experiments the initial temperature level of the interface changed from the liquidus towards to the solidus temperature. Here, solidification starts at a temperature of $T = 412.9$ K. The initial α-phase follows the liquidus line from point A to C (orange arrow), whereas, the solid concentration following the solidus line from point B to D (orange arrow). Simultaneously, the existing β-phase follows the liquidus line of the β-phase (green arrow). Due to the pile-up of the boundary layer the liquid ahead of the interface was constantly enriched with NPG. Additionally, the density difference between the two substances, where $\rho_{TRIS} > \rho_{NPG}$, leads to solutal convection in front of the interface.

The α-phase tries to reach steady-state conditions at a temperature of $T = 408.4$ K, point C. For this, an undercooling $\Delta T_\alpha = 4.5 \pm 0.5$K is necessary. The s/l interface reaches the temperature where initial β-phase was observed, which is at $T = 409.8$ K. This corresponds to an undercooling of $\Delta T_\beta = 2.2 \pm 05$ K. Note, that within the α-phase matrix the still existing β-

phase grows partial through existing liquid channels. Additionally, close to the side walls the concentration ahead of the β-phase was enriched with NPG. Afterwards the β-phase tries to overgrow the α-phase at the s/l interface. According to the phase diagram, the growth of the β-phase leads to a reduction of the NPG concentration ahead of the s/l interface.
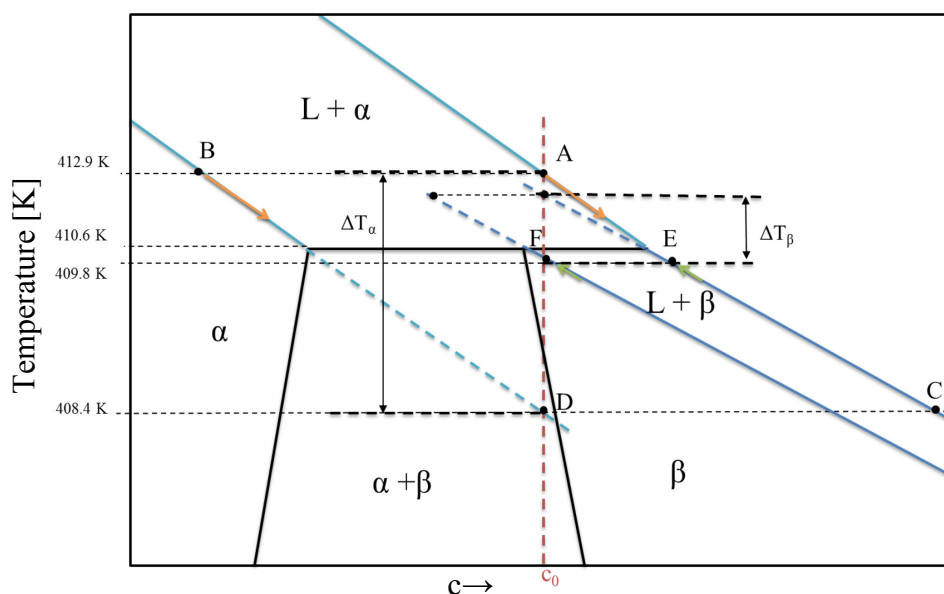

Fig. 52: Solidification path for a concentration c_0.

Fig. 53 shows the movement of the interfaces with time. The values for the position of the interface were measured at the center of the sample, whereas the values for the bands were measured directly from beginning of nucleation. The red line corresponds to the primary solid/solid interface. The temperature where β nucleates or occurs due to growth along a channel is $T = 409.4 \pm 1$ K. The s/l interface starts with a liquidus temperature of $T = 412.9 \pm 1$K and decreases to $T = 410 \pm 1$ K.
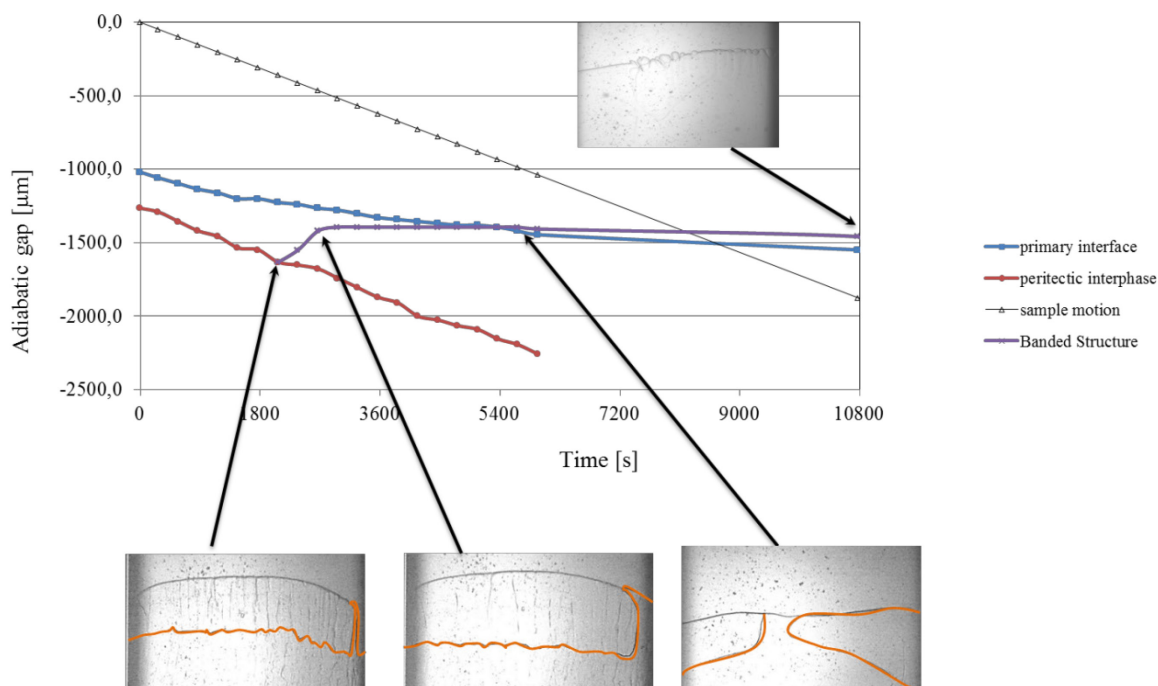
Fig. 53: Movement of the interfaces with time: the red line corresponds to the initial β-interface and the blue line corresponds to the α-interface.

Fig. 54 shows the change of both interface temperatures within the first 10800 s. They were measured from the position within the adiabatic gap from Fig. 53 with the associated temperature gradient.

The results match with the liquidus temperature of this concentration. The growth of the β-band starts from out of the peritectic interface at $T = 409.4 \pm 1$ K increases up to 410.8 ± 1K and remains fairly constant. Taking the measurement accuracy into account, the transition temperatures confirm to the published phase diagram. After $t = 10800$ s PCG started with $T = 410.4 \pm 1$ K. The temperature of the solid/liquid interface is 0.5 ± 0.5 K lower compared to the temperature of the band and 0.7 ± 0.5 K lower than the peritectic temperature.
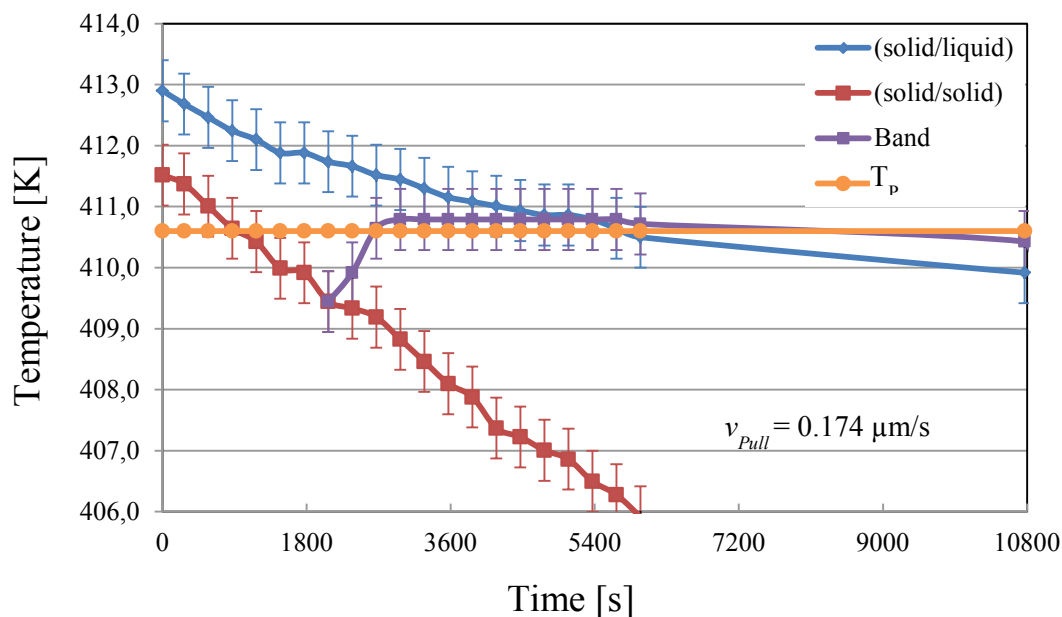
Fig. 54: Time depending interface temperatures for experiment $x = 0.52$ mol fraction NPG.

The evolution of such layered microstructure pattern was published in several papers [6-11]. New in this project is the ability to make convection in front of the layered structures visible. As in the previous experiment, certain particles were selected and their time-depending positions were marked by using arrows with different colors.

By observing the particles during the formation of banded structure experiments, it could be shown, that at the beginning of the solidification experiment the flow established like for experiment with planar front, see Fig. 55a. The flow starts in the middle of the sample and moves gradually towards the left and right sample wall, where the particles drifted upwards again. After approx. $t = 2760$ s a second flow starts from the right side of the sample to the left side in direction with the right band, see Fig. 55b. Particles at the right side near the interface followed the growth of the band. Whereas, particles at the upper liquid material stayed unaffected from the growth of the band and moved undisturbed on streamlines like at the beginning from the middle to the right side and curved upwards at the sample wall, see Fig. 55b.

Diffusion processes along the s/l interface have therefore a great influence on the formation of the flow pattern or rather on the formation of the banded structure. The growth of the peritectic phase needs more solute than primary phase. The dissolution of β during peritectic

reaction absorbs solute atoms from the liquid, which can induce the local diffusion current. This is also assumed for the development of the left band. This would mean that there is also a flow from the left side of the sample wall towards the center. But, this cannot be confirmed since no particles were found which show that there is any flow following the left band, see Fig. 55b.

This absence of flow from left to right can be stated due to the strong flow coming out of the existing micro-plume, which forms a kind of flow barrier that all particles in the surrounding are distracted by this upwards movement, see chapter 4.1.

(a) (b)
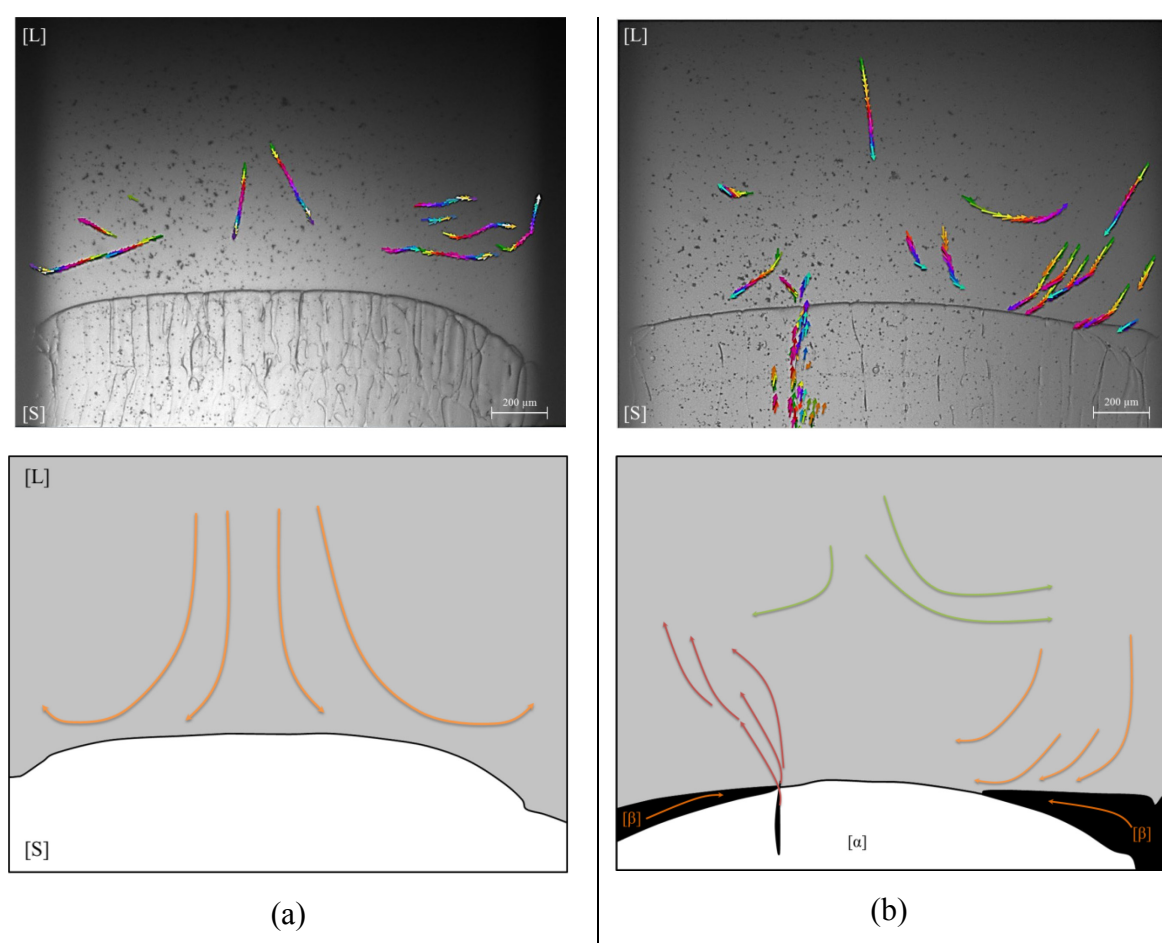
Fig. 55: Real and idealized pictures of the flow behaviour while formation of banded structure: (a) the flow pattern initially behaves exactly as in the experiment with planar solidification front due to the almost planar interface here. (b) The reverse flow on the right side of the forming β-band (orange arrows) could be well presented whereas the flow above the left β-band is hardly visible due to the influence of the existing flow out of the micro-plume (red arrows).

Layered structures, $x = 0.52$ mol fraction NPG, $v = 0.157$ µm/s

Again, after 1 hour keeping the sample unmoved within the temperature gradient of the Bridgman-furnace, steady-state condition was reached. The s/l interface was, planar but slightly curved only on the left side of the sample.

Fig. 56 shows the change of the interface temperatures and Fig 57 shows the change of the interface within the adiabatic gap. The values for the s/l interface were measured at the center of the sample, whereas the values for the band were measured directly from beginning of nucleation which was after $t = 2070$ s at a temperature of 411.6 ± 1 K and reached steady-state at 411.3 ± 1 K. After $t = 7350$ s PCG started also with $T = 411.3 \pm 1$ K. The s/l interface grew approx. 1.4 ± 0.5 K above the peritectic temperature and the band grew approx. 0.7 ± 0.5 K above T_P.
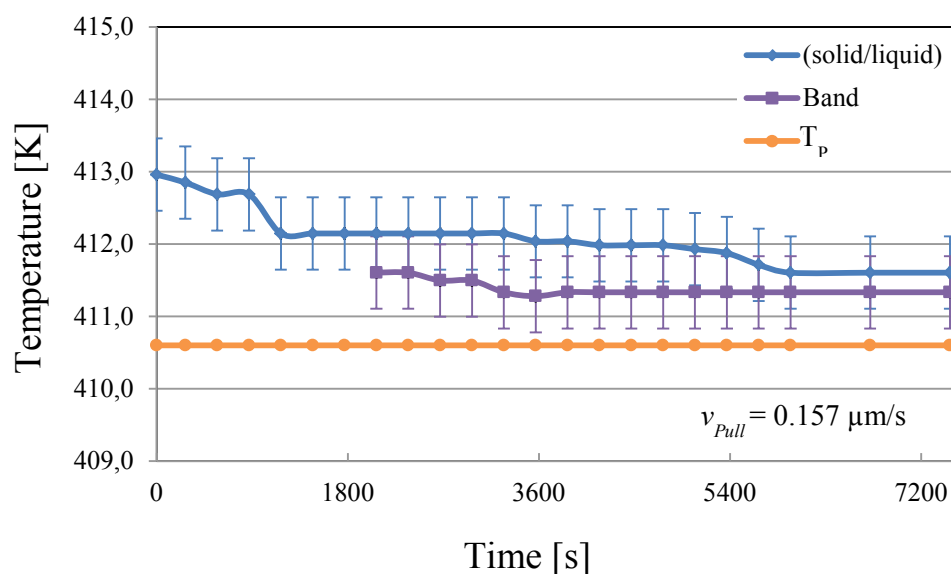
Fig 56: Time depending interface temperatures for experiment $x = 0.52$ mol fraction NPG

It has to be noted, that the temperature of the PCG for experiment $x = 0.52$, $v = 0.174$ µm/s grows below the peritectic temperature, see Fig. 54, whereas, for experiment $x = 0.52$, $v = 0.157$ µm/s PCG grew above T_P.

Fig 57 shows the evolution with increasing time for the adiabatic gap. At first nucleation of β starts and finally transform into PCG.
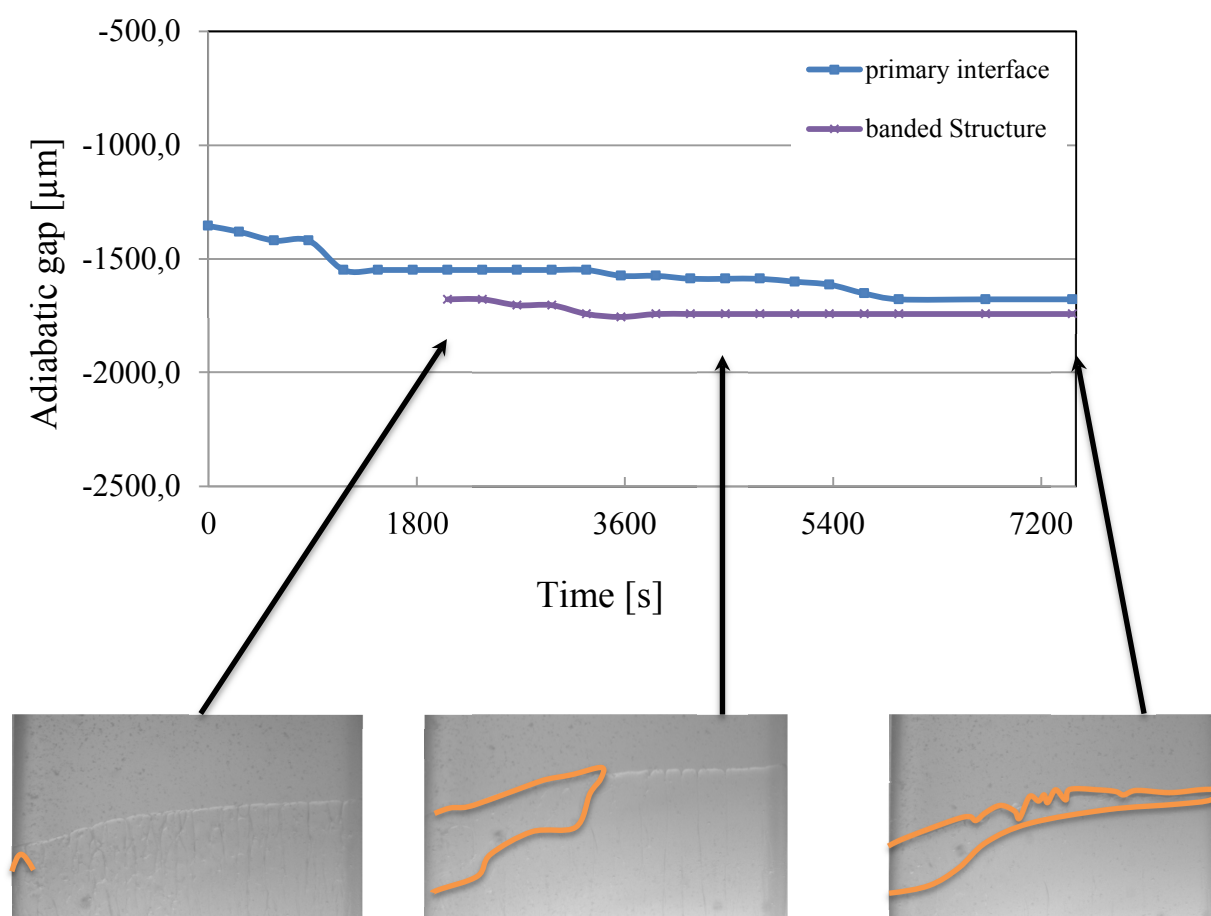
Fig 57: Movement of the interfaces with time within the adiabatic gap: the blue line corresponds to the s/l interface and the violet line corresponds to the band.

Comparison of the flow patterns

The change of the convection flow pattern during the formation of layered structures leads to the question whether there is a coherency. To answer this, we consider the influence of growth near the glass wall.

Before the β-phase grew the s/l interface was curved against the side walls. It is explained in the chapter 6.3, that this is a consequence of the density of the solute in combination with the direction of the earth's gravity gradient. To keep the mass constant, liquid moves at the centre downwards and at the side walls upwards. As soon as solidification close to the side wall starts the lighter density liquid change into the denser solid by solute rejection at the interface. To keep the mass constant, more liquid has to flow close to the side wall. In contrast, at the

centre of the sample the existing α-phase is inhibited by the evolution of the β-phase. As a consequence, the flow pattern changes.

Comparing the solidification experiments, it can be seen, that all experiments showed curved s/l interfaces. Obviously, all experiments showed fairly the same initial flow pattern, see Fig. 58a and b. For experiment with $v = 0.157 \mu m/s$ there is a slight curvature on the left side of the sample (c). It is assumed, that the shape of the boundary layer in front of the s/l interface or rather the enrichment of NPG and the local temperature difference between s/l interface and the resulting curvature has a great impact on the evolution of the flow within the sample.

(a)   (b)   (c)
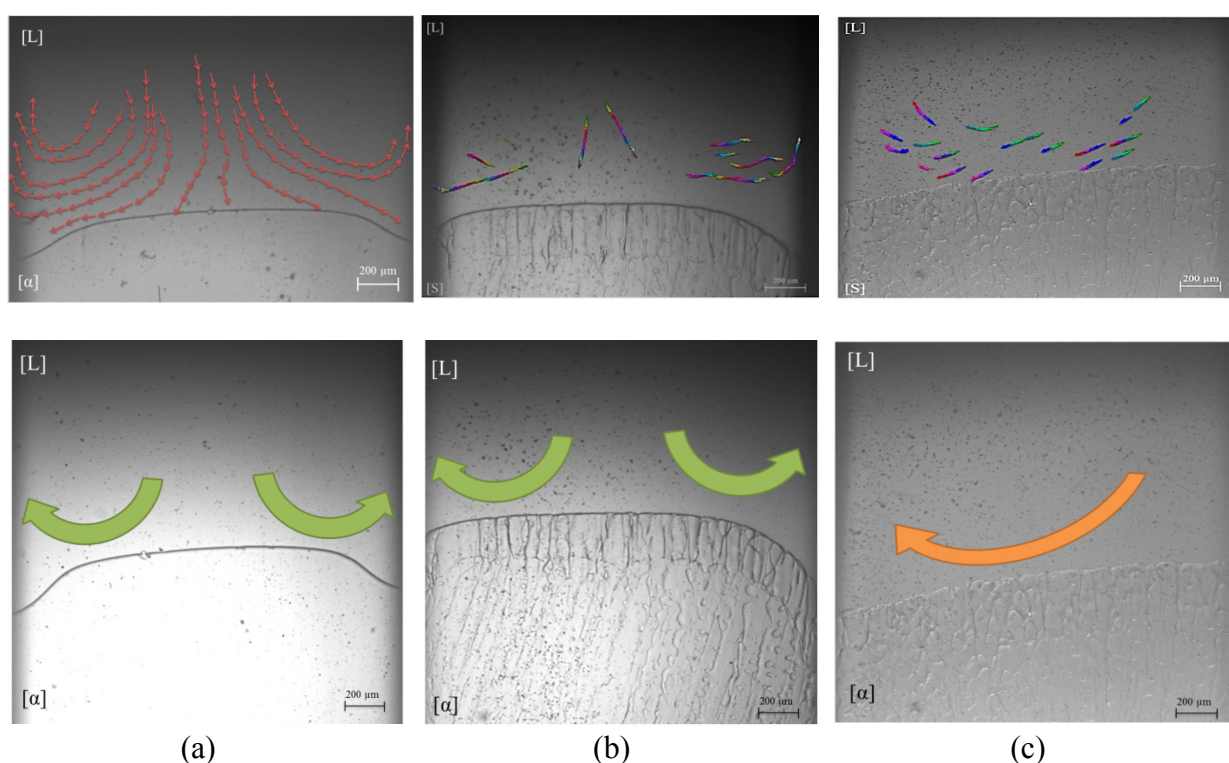
Fig. 58: Comparison of the initial flow pattern of all three experiments (a) planar (b) HGS, $x = 52$ mol fraction NPG, $v = 0.174$ µm/s and (c) HGS, $x = 52$ mol fraction NPG $v = 0.159$ µm/s.

If we compare the flow pattern within the time interval, where layered structures occur, it can be seen, that for experiment $x = 0.52$ mol fraction NPG and $v = 0.174$ µm/s the main flow in the middle of the liquid material stays unaffected of the formation of bands. But near the growing band at the right side of the sample, the particles follows the growth direction of the forming β-phase, since the β-phase absorbs enriched liquid material and rejects less segregated solute so that the high solute concentration is now in front of the α-phase at the sample center , see Fig. 59a.

Due to the strong flow out of the liquid channel, which is situated near the growing β-band at the left hand side in Fig. 59a we observed an influence of the micro-plume on the flow pattern in this area.

For the investigation of thermo-solutal convection, the comparison with the experiment $x = 0.52$ mol fraction NPG and $v = 0.159\mu m/s$ is useful, where just one β-band at the left hand side occurred, see Fig. 59b. In addition, there is small curvature at the left side of the sample. There were no significant liquid channels observed near the band, which could affect the flow in front of the interface. At the beginning, the flow pattern shows the same vortex as in all other experiments. Due to the fact that there was just one side curved, this vortex is just in one direction. In fact, the pattern of flow showed no reversal caused by the formation of the β-band. It can be stated that such reversed flow cannot be observed, since this band grows most likely in another plane of the sample. This is explained in chapter 4.2. So, no particles are traceable in this direction because particles simply cannot be detected in areas located further in the back of the sample.

(a)   (b)
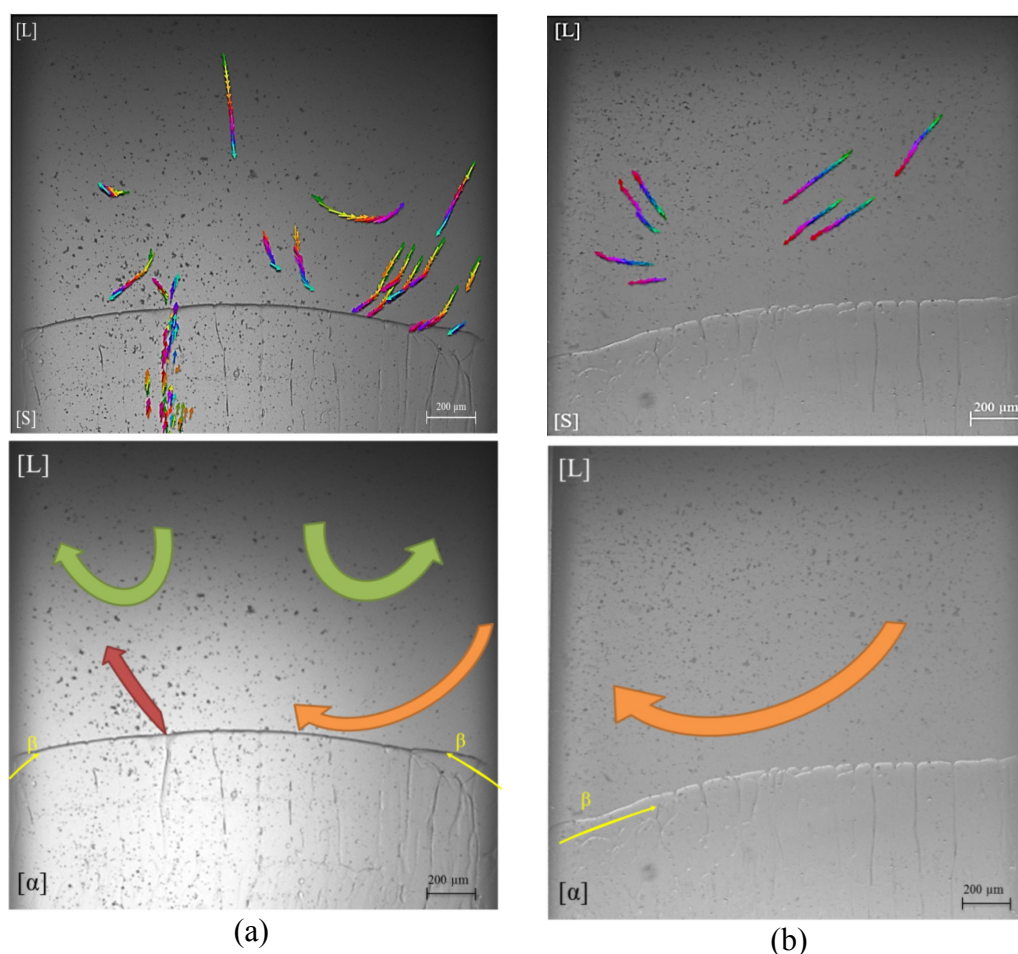
Fig. 59: Comparison of the evolution of flow pattern of layered structures experiments. Note that the band in (b) grows in another plane of the sample.

In summary, it can be concluded, that for all experiments, where curved interfaces were present, the flow pattern looks like in Fig. 58a. With the formation of bands, this flow pattern reverses to a pattern like in Fig. 59a. Due to the fact that experiments with curved interfaces showed quite similar flow patterns it is assumed that this is a result of density changes in front of the interface near the curvature. This density changes are caused by changes in concentration and, thus, also local temperature changes occured which influence the flow pattern due to this thermo-solutal convection. In fact, in all experiments, β-bands grew below the temperature of the s/l interface and above the peritectic temperature.

6. Summary

The assumption that flow in the melt, caused by the thermo-solutal convection, influence the formation of layered structures in peritectic systems was investigated. This was done by using the transparent organic model system TRIS-NPG. The solidification experiments were carried out with the Bridgman method. The investigation range was from $x = 0.48$ to $x = 0.54$ mol fraction NPG. This covered the entire hypo- and hyper-peritectic region. Here, all kind of morphologies were observed. Special attention was paid on layered structure experiments, which were found for $x = 0.50$ and $x = 0.52$ mol fraction NPG.

In order to monitor any flow in front of the s/l interface, indicators were added within the melt. Since the commercially available tracers, HGS particles are uniformly distributed within the liquid and its density is close to that of the melt, the flow could be observed quite well by the movement of these tracers. Additionally, the formation of layered, peritectic solidification in form of laterally growing bands was investigated more closely. The fact that the particles did not influence the material as well as the formation of layered structures was an important finding in this project. A challenge hereby was the evaluation of the movement of the indicators with particle velocimetry software. However, it was not possible to evaluate the particle motion by using this software. Hence, the estimation of the flow pattern had to be carried out manually. The best solution for this was to mark well-visible particles with an arrow and to visualize the total movement by overlapping all the arrows after a certain time. In order to further support the results which are obtained here, investigations with fluorescent particles in conjunction with a laser would be advantageous. With this method, the PIV software could be used.

For the first time, the evolution of the flow within the liquid during a solidification experiments could be observed. The existence of liquid channels within the mushy zone and its behaviour through the liquid as micro-plumes was observed. These plumes influenced the particles in the surrounding liquid. Furthermore, the reversal of the flow near the interface due to local temperature and density differences, caused by thermo-solutal convection was a major finding of this work.

Of course, it would be very interesting to simulate convection at the s/l interface with respect to these experiments with suitable software, for example phase field simulations with MICRESS.

Following up on this work, there will be additional experiments in space in near future. The same experiments which are carried out in this thesis will be tested on board of the ISS. A comparison of the ground experiments with those experiments without any convection will be very enlightening.

7. List of figures

8. List of Tables

9. Literature

[1]   S.T. Misture, D.P. Matheis, R.L. Snyder, T.N. Blanton, G. M. Zorn, B. Seebacher, Physica C: Superconductivity, 250 (1995) 175-183.

[2]   Matsumiya T, Yamada W, Ohashi T and Nittono O, Metall. Mater. Trans. A 18 (1987) 723.

[3]   R.Rudman, Solid State Commun, 29 (1979) 785-787.

[4]   J.Timmermans, J.Phys.Chem.Solids, 18 (1961) 1-8.

[5]   L.A.K.Staveley, Annu. Rev. Phys. Chem. 13 (1962) 351-368.

[6]   P.R.Sahm, I.Egry, T. Volkmann, "Schmelze, Erstarrung, Grenzflächen", Vieweg Verlag [ISBN 3-528-06979-1].

[7]   W.J. Boettinger, Metall. Trans. 5 (1974) 2023.

[8]   J.H. Lee, J.D. Verhoeven, J. Cryst. Growth 144 (1994) 353.

[9]   M. Vandyoussefi, H.W. Kerr, W. Kurz, Acta Mater. 48 (2000) 2297.

[10]   P. Mazumder, R. Trivedi, A. Karma, Metall. Trans. 31A (2000) 1233.

[11]   R. Trivedi, J.S. Park, J. Cryst. Growth 235 (2002) 572.

[12]   P. Mazumder, R. Trivedi, Phys. Rev. Lett. 88 (2002) 235507.

[13]   M. Sumida, J. Alloys Compd. 349 (2003) 302.

[14]   T.S. Lo, S. Dobler, M. Plapp, A. Karma, W. Kurz, Acta Mater. 51 (2003) 599.

[15]   S. Dobler, T.S. Lo, M. Plapp, A. Karma, W. Kurz, Acta Mater. 52 (2004) 2795.

[16]   R. Trivedi, J.H. Shin, Mater. Sci. Eng. A 413–414 (2005) 288.

[17]   J. Mogeritsch, Investigation on Peritectic Solidification using a Transparent organic system, Montanuniversität Leoben, June 2012.

[18]   D.R. Uhlmann and G.A. Chadwick, Acta Metall. 9 (1961) 835–840.

[19]   W.J.Boettinger, Metall.Trans. 5 (1974) 2023 - 2031.

[20]   H.Yasuda, N.Notake, K.Tokieda and I.Ohnaka, J. Cryst. Growth 210 (2000) 637–645.

[21]   J.H.Lee and J.D.Verhoeven, J. Cryst. Growth 144 (1994) 353–366.

[22]   H.Zhong, S.M.Li, H.Y.Lü, L.Liu, G.R.Zou and H.Z.Fu, J. Cryst. Growth 310 (2008) 3366–3371.

[23]   H.W. Kerr, W. Kurz, Int. Mater. Rev. 41 (1996) 129.

[24]   W.Kurz, D.J.Fischer, "Fundamentals of solidification", Trans tech Publications Ltd 1998 [ISBN 0-87849-804-4].

[25]   R.F. Sekerka W.W. Mullins. J. Appl. Phys., (1964) 35, 444.

[26]   J.W. Rutter B. Chalmers W. Tiller, K.A. Jackson. Acta Metall., (1953) 1, 428.

[27]   O.Hunziker, M. Vandyoussefi, W. Kurz. Act Metal., Vol. 46, No. 18 (1998) 6325-6336.

[28]   M. C. Flemings T. F. Bower, H. D. Brody. Trans. Met. Soc. AIME, 236, (1981) 624.

[29]   Yasuda H, Ohnaka I, Tokieda K. In: Beech J, Jones H, editors. Solidification processing. University of Sheffield; 1997. p. 44-8.

[30]   J.A. Dantzig, M. Rappaz, Solidification, EPFL press, 2009.

[31]   Sumida M, J. Alloys Comp. (2003) 349 302.

[32]   T.S. Lo, S. Dobler, M. Plapp, A. Karma, W. Kurz, Acta Mat. 51, (2003) 599-611.

[33]   Mazumder P, Trivedi R, Karma A. In "Phase Transformations and Systems Driven far from Equilibrium", eds MaE, Bellon P, Atzmon M, Trivedi R, Materials Research Society (MRS) Proceedings, Vol. 481, 1998, p. 39-44.

[34]   Mazumder P. PhD thesis. Iowa State University; 1999.

[35]   M.Barrio, D.O.Lopez, J.L. Tamarit, P.Negrier and Y.Haget, J.Mater.Chem.5 (1995) 431-439.

[36]   L.Sturz, V.T.Witusiewicz, U.Hecht and S.Rex, J.Crystal Growth 270 (2004) 273-282.

[37]   https://www.merck.de, visit on 12.12.2017.

[38]   Datasheet TRIS(hydroxymethyl)aminomethane at Sigma-Aldrich, (last download: 14.01.2018).

[39]   O.Hunziker, M.Vandyoussefi and W.Kurz, ActaMater Vol. 46 (1998) 6325-6336.

[40]   Ludwig A., Mogeritsch J., Kolbe M., Gerhard Z., Sturz L., Bergeon N., Faivre G., Billia B., Akamatsu S., Bottin-Rousseau S., Voss D.: JOM 64 (2012) 1097-101.

[41]   J. Mogeritsch, A. Ludwig, Iop Conference Series Materials science and engineering (2012).

[42]   M.E. Glicksman, S.R. Coriell, G.B. McFadden, Ann. Rev.Fluid Mech. 18 (1986) 307.

[43]   S.H. Davis, J. Fluid Mech. 212 (1990) 241.

[44]   G. Muller, A. Ostrogorsky, in: D.T.J. Hurle (Ed.), Handbook of Crystal Growth, Vol. 2B, North-Holland, Amsterdam, (1994) 709.

[45]   S.H. Davis, T.P. Schulze Metallurgical and Materials Transactions A: Physical Metallurgy and Materials Science, (1996) 583-593.

[46]   Sahm P.R., Egry I., Volkmann T. (eds) Schmelze, Erstarrung, Grenzflächen. Springer, Berlin, Heidelberg.

[47]   R. Trivedi, J.S. Park, Journal of Crystal Growth 235 (2002) 573-588.

[48]   W.Boettinger, S.Coriell, M. Rappaz and R. Trivedi, Acta mater. 48 (2000) 43-70.

[49]   A. Saad, C. Gandin, M. Bellet, N. Shevchnko, S. Eckert, Metallurgical and Materials Transactions A, Springer Verlag/ASM International, 2015, Symposium ICASP-4 International Conference on Advanced Solidification Processing, 46 (11), (2015) 4886-4897.

[50]   D. Tourret, Y. Song, A. Clarke, A. Karma, Acta   Mater. Vol. 122 (2017) 220-235.

[51]   T. Takaki, S. Sakane, M. Ohno, Y. Shibuta, T. Shimokawabe, T. Aoki, ISIJ Int. 56 (8) (2016) 1427-1435.

[52]   L. Wang, N. Wang, N. Provatas, Acta Mater. 126 (2017) 302-312.

[53]   A Melling, Measurement Science and Technology, Vol. 8, Nr. 12.

[54]   Klaus Luckert: Handbuch der mechanischen Fest-Flüssig-Trennung. Vulkan-Verlag GmbH, 2004, ISBN 3-8027-2196-9.

[55]   Mogeritsch J., Ludwig A., Eck S., Grasser M., McKay B.: Scripta Mater., 60 (2009) 882-5.

[56]   Dantec Dynamics: https://www.dantecdynamics.com/ (download: 03.12.2017).

[57]   Sigma Aldrich: https://www.sigmaaldrich.com/austria.html.

10. Symbols

Symbol	Meaning	Definitions	Units
c	concentration	$C = x \cdot 100\ \%$	mol.%
c_0	initial concentration		mol.%
c_L	liquidus concentration		mol.%
c_S	solidus concentration		mol.%
c_p	peritectic concentration		mol.%
D	diffusion coefficient		m^2/s
G_T	temperature gradient		K/m
i	index		-
k	distribution coefficient	$k = C_S/C_L$	-
M	molar mass		g/mol
m_L	liquidus slope	$m = \Delta T_L/\Delta C$	K/mol
m_s	solidus slope		
p	pressure		Pa
T_{cold}	temperature in the cold zone of the Bridgman-furnace		K
T_{hot}	temperature in the hot zone of the Bridgman-furnace		K
T_L	liquidus temperature		K
T_m	melting temperature		K
T_p	peritectic temperature		K
T_S	solidus temperature		K
T^{α}_S	solidus temperature of the α-phase		K
T^{β}_S	solidus temperature of the β-phase		K
t	time		s
v	growth or solidification velocity		m/s
v_c	critical solidification velocity		m/s
v_L	lateral solidification velocity		m/s
v_{pull}	pulling velocity		m^2/s
v_{α}	solidification velocity of the α-phase		m/s
v_{β}	solidification velocity of the β-phase		m/s
$v_{\alpha, \beta}$	solidification velocity of α- and β-phase		
ΔT_0	temperature difference between T_L and T_S		K
ΔT_N	Nucleation undercooling		K
Δt	time difference		s
β_{met}	metastable β-phase		
δ	boundary layer thickness		m
η	dynamic viscosity		Pa·s
κ	heat conductivity		W/K m
x	mol fraction	$x = C/100\ \%$	-